8-2019

Real-Time Prediction and Decision Making in Connected and Automated Vehicles Under Cyber-Security and Safety Uncertainties

Franco van Wyk
University of Tennessee, fvanwyk@vols.utk.edu

To the Graduate Council:

I am submitting herewith a dissertation written by Franco van Wyk entitled "Real-Time Prediction and Decision Making in Connected and Automated Vehicles Under Cyber-Security and Safety Uncertainties." I have examined the final electronic copy of this dissertation for form and content and recommend that it be accepted in partial fulfillment of the requirements for the degree of Doctor of Philosophy, with a major in Industrial Engineering.

Anahita Khojandi, Major Professor

We have read this dissertation and recommend its acceptance:

Mingzhou Jin, P.J. Vlok, Neda Masoud, David B. Clarke

Accepted for the Council:

Dixie L. Thompson

Vice Provost and Dean of the Graduate School

(Original signatures are on file with official student records.)

Real-Time Prediction and Decision Making in Connected and Automated Vehicles Under Cyber-Security and Safety Uncertainties

A Dissertation Presented for the

Doctor of Philosophy

Degree

The University of Tennessee, Knoxville

Franco van Wyk

August 2019

This dissertation is dedicated to my mother, father, and sister. Thank you for your endless support and encouragement.

Acknowledgments

I would like to thank my academic adviser, Dr. Anahita Khojandi, who guided me through this process. Thank you for the advice and willingness to always share new insights. I would also like to thank my committee members for their advice and guidance.

Abstract

Connected and automated vehicles (CAVs) are expected to transform current transportation systems into highly efficient, automated, and intelligent systems. CAVs, with various levels of automation and connectivity, are expected to reduce travel time, improve travel comfort, improve fuel efficiency, and decrease fatal accidents in the near future. CAVs use a combination of cameras, ultrasonic sensors, and radar to build a digital map of their surroundings and operate the vehicle accordingly. As a result, there are numerous sources of information that can be manipulated, with malicious or non-malicious intent, which may result in dangerous situations. Although the ever-increasing use of CAV technologies in vehicles are expected to have numerous advantages, they can give rise to new challenges in terms of safety, security, and privacy. As evident by recent crash records and experiments successfully conducting cyber attacks on vehicles, the currently available autonomous systems lack the ability to fully handle novel, complex situations. Hence, the potential drawbacks of CAVs are not negligible and should not be ignored. In this research, we investigate the real-time prediction and decision making in CAVs under cyber-security and safety uncertainties.

Table of Contents

List of Tables

List of Figures

Introduction

In *Chapter 1*, we investigate real-time sensor anomaly detection and identification in CAVs. To navigate roadways, CAVs need to heavily rely on their sensor readings and the information received from other vehicles, i.e., vehicle-to-vehicle (V2V) communication, and roadside units, known as vehicle-to-infrastructure (V2I) communication. Hence, anomalous sensor behavior/data points caused by either malicious cyber attacks or faulty vehicle sensors can result in disruptive consequences, and possibly lead to fatal crashes. As a result, before the mass implementation of CAVs, it is important to develop methodologies that can detect anomalies and identify their sources seamlessly and in real-time.

Next in *Chapter 2*, we focus on the limitations of semi-autonomous vehicles under certain circumstances where it is safer for the human driver to be in control compared to the automated driving system. Such circumstances may be caused due to technological failures, complex road and environmental conditions, or infrastructure deficiencies (e.g., lack of roadside units or high-definition maps in certain areas), to name a few. Hence, for the foreseeable future, the need for the transition of authority between the human driver and the autonomous entity would continue to complicate traveling through the road network. Switching control back and forth between the human driver and the autonomous driving entity to maximize safety may not be straightforward as every such switch can itself pose a short-term, elevated risk, especially under highly dynamic and stochastic traffic conditions. As a result, we investigate the transfer of control authority in semi-autonomous vehicles to improve overall road safety.

Lastly, in *Chapter 3* we investigate real-time dynamic thresholding in classification algorithms to adapt to complex road and environmental conditions. The successful operation of CAVs are dependent on a large number of information sources such as on-board sensors, roadside units, cloud data, and other vehicles. As a result, these vehicles are susceptible to false/incorrect information, originating from various sources. A classification algorithm is therefore required to detect the false/incorrect information. Traditional classification algorithms use fixed and *a priori* determined thresholds which determine if information is anomalous or not. However, this approach does not allow for incorporating feedback obtained during a trip on the performance of the classification algorithm which may result in excessive false positive/negatives. It is therefore critical to dynamically alter this threshold of the classification algorithm in real-time to respond to past performance and exogenous factors to assure reliable and robust system operation.

Below are summaries of the *methods* developed in the three chapters to improve real-time prediction and decision making in CAVs under cyber-security and safety uncertainties.

- *Chapter 1.* We develop a robust anomaly detection approach through combining a deep learning method, namely convolutional neural network (CNN), with a well-established anomaly detection method, Kalman filtering, to detect and identify anomalous behavior in CAVs in real-time. Our numerical experiments demonstrate that the developed approach can detect anomalies and identify their sources with high accuracy, sensitivity, and F1 score. In addition, this developed approach outperforms the anomaly detection and identification capabilities of both CNNs and Kalman filtering methods alone.

- *Chapter 2.* We develop a generalizable framework that allows for adaptive balancing of risks and benefits of having an autonomous entity navigate a complex environment. Specifically, we develop a Markov decision process (MDP) model to prescribe the entity in charge to minimize the expected safety risk of a trip, considering the dynamic changes of the road/environment during the trip. We provide numerical experiments in which we compare the expected cost/safety of trips under the optimal policy with a few benchmark policies illustrating the benefits under the optimal policy. In addition, we perform sensitivity analyses to investigate the calibrated parameters and the robustness of the MDP model. As a result, we gain insights into the associated risks and advantages of authority control transitions for semi-autonomous vehicles in certain conditions. We also develop a partially observable Markov decision process (POMDP) model to account for cases when only partial information of the environmental risk is available. We solve the POMDP using a state of the art deep reinforcement learning technique, namely the asynchronous advantage actor critic (A3C) algorithm.

- *Chapter 3.* We develop a mathematical framework in which we pair an anomaly classification algorithm, based on CNN, with a partially observable Markov decision process (POMDP) model to determine the optimal dynamic threshold of an anomaly classification algorithm to maximize the safety of a trip. We solve the resulting POMDP model using the asynchronous advantage actor critic (A3C) deep reinforcement learning algorithm. We provide numerical experiments in which we compare the performance of the benchmark model, i.e., the CNN model with a fixed threshold, to the developed POMDP model utilizing a dynamic threshold. The numerical experiments suggest that the addition of the POMDP model improves the anomaly detection performance of the CNN model, resulting in high accuracy, sensitivity, and positive predictive value. As a result, we gain insights into the associated benefits and disadvantages of implementing a dynamic classification threshold in response to complex exogenous factors.

Chapter 1

Real-Time Sensor Anomaly Detection and Identification in Automated Vehicles

Disclosure: This chapter is based on a paper published by van Wyk et al. (2019) in IEEE Transactions on Intelligent Transportation Systems.

van Wyk, F., Wang, Y., Khojandi, A. and Masoud, N., 2019. Real-Time Sensor Anomaly Detection and Identification in Automated Vehicles. IEEE Transactions on Intelligent Transportation Systems.

My contributions to this paper include: (i) the development of the problem and methodology to investigate the problem, (ii) reviewing the appropriate literature, (iii) the identification of study objectives, (iv) collection of data, (v) design and conducting of the numerical experiments, (vi) majority of the writing responsibilities of the manuscript.

Abstract

Connected and automated vehicles (CAVs) are expected to revolutionize the transportation industry, mainly through allowing for a real-time and seamless exchange of information between vehicles and roadside infrastructure. Although connectivity and automation are projected to bring about a vast number of benefits, they can give rise to new challenges in terms of safety, security, and privacy. To navigate roadways, CAVs need to heavily rely on their sensor readings and the information received from other vehicles and roadside units. Hence, anomalous sensor readings caused by either malicious cyber attacks or faulty vehicle sensors can result in disruptive consequences, and possibly lead to fatal crashes. As a result, before the mass implementation of CAVs, it is important to develop methodologies that can detect anomalies and identify their sources seamlessly and in real-time. In this work, we develop an anomaly detection approach through combining a deep learning method, namely convolutional neural network (CNN), with a well-established anomaly detection method, Kalman filtering with a χ^2-detector, to detect and identify anomalous behavior in CAVs. Our numerical experiments demonstrate that the developed approach can detect anomalies and identify their sources with high accuracy, sensitivity, and F1 score. In addition, this developed approach outperforms the anomaly detection and identification capabilities of both CNNs and Kalman filtering with a χ^2-detector methods alone. It is envisioned that

this research will contribute to the development of safer and more resilient CAV systems that implement a holistic view towards intelligent transportation system (ITS) concepts.

1.1 Introduction

Our current transportation system is on the brink of transforming into a highly connected, automated, and intelligent system as a result of the rapid emergence of connected and automated vehicles (CAVs) (Ran and Boyce, 2012). CAVs, with various degrees of connectivity and automation, are expected to play an integral role in the next phase of the transportation revolution, leading to more accessible, more efficient, safer, more environmentally friendly, and hence sustainable, transportation options (Meyer and Beiker, 2014; Litman, 2017). CAVs use wireless technology to facilitate communication between vehicles, with roadside units (RSUs), and with personal mobile devices. This will allow them to continuously transmit and share information such as speed, position, acceleration, and braking, enabling CAVs to warn their surrounding vehicles of potentially unsafe circumstances. These vehicle-to-vehicle (V2V) and vehicle-to-infrastructure (V2I) communication technologies will provide unprecedented efficiency, safety, and mobility advancements. For instance, CAV technologies are expected to decrease fatal traffic accidents by as much as 80%, reducing their corresponding $870 billion cost, while also improving traffic flow, cutting into the approximate 7 billion hours American motorists spend in traffic annually (USDOT, 2016).

Although the ever-increasing use of CAV technologies in vehicles are expected to have numerous advantages, the potential drawbacks are not negligible. CAVs use a variety of sensors to build a virtual map of their surroundings in order to drive in the correct lane within the speed limit, avoid collisions, and detect obstacles in their immediate physical environment. Hence, anomalous sensor values caused by either malicious cyber attacks or faulty vehicle sensors can result in disruptive consequences, and possibly lead to fatal crashes. The increase in connectivity and automation has led to the scrutiny of in-vehicle network architectures used by automotive manufacturers and evaluation of vulnerabilities in their resiliency against such anomalous behavior (Koscher et al., 2010; Greenberg, 2015; Weimerskirch and Gaynier, 2015). For instance, the dedicated short-range communication (DSRC) technology is currently used to facilitate communication within connected networks.

DSRC has a range of approximately 300 meters, hence it can protect vehicles from long-range cyber attacks, e.g., a stationary attacker would only have a short time-window to attack moving vehicles when they are in close proximity (Bai et al., 2010). Although such a technology can prove useful, it is not comprehensive enough and leaves CAVs vulnerable to non-stationary attackers, among others. Hence, it is necessary to better understand CAVs' vulnerabilities and develop holistic, real-time methodologies that can mitigate them.

Various internal and external cyber attack surfaces exist in CAV systems, i.e., the entry point of the attack, which may enable hackers to access and compromise the safety and integrity of CAVs (Koscher et al., 2010; Checkoway et al., 2011; Greenberg, 2015; Weimerskirch and Gaynier, 2015; Petit and Shladover, 2015; Yan et al., 2016; Field, 2017). Typical *internal* attack surfaces include in-vehicle devices, GPS system, on-board diagnostics (OBD) system, vehicle sensors including the controller area network (CAN) bus, and other sensors required for CAV operation. For instance, Checkoway et al. (2011) demonstrated through an OBD port attack, it is possible to disable the brakes, turn-off head-lights, and take over steering for cars equipped with a low level of autonomy. Typical *external* attack surfaces include information from RSUs, machine vision, data from other vehicles, security system breaches of the vehicle, and navigation interference (Field, 2017; Jo et al., 2016; Truong et al., 2005). For instance, Field (2017) demonstrated how an attacker could gain access to the visual recognition software used in autonomous vehicles and manipulate it by creating a simple alteration to RSUs that would cause the car to misinterpret them, possibly putting vehicle occupants at risk. Similarly, several teams have hacked traffic light controller systems, highway signs, and traffic surveillance cameras (Huq et al., 2017). For instance, in 2017, approximately 70% of the storage devices that record data from Washington D.C. police surveillance cameras were infected with ransomware by hackers (Williams, 2017). Injection of fake information and map database poisoning is considered to be one of the most dangerous cyber attacks on CAVs (Petit and Shladover, 2015). Future CAVs are expected to have even more attack surfaces than what has currently been investigated. Possible reasons for cyber attacks on CAVs include financial gain, collecting private information, and gaining priority access to infrastructure.

Not all anomalous sensor behavior are due to malicious attacks. Sensor readings may be influenced for a variety of reasons prompting the transmission of faulty information (Checkoway et al., 2011; Realpe et al., 2015; Pous et al., 2017). For instance, sensors in CAVs may be blinded by magnetic interference, signal outage, poor weather conditions, and other environmental circumstances. Furthermore, as sensors age, inherent errors are introduced which may result in sensor failure, therefore, affecting data availability. Faulty sensors, therefore, pose significant risks to the operation of CAVs since their safe operation depends on information obtained from sensors.

Sensor redundancy is a measure that can be implemented to protect CAVs against anomalous sensor behavior. The majority of CAV manufacturers are expected to incorporate multiple sensors that measure the same parameter (Darms et al., 2008). For instance, CAVs may utilize various sensor systems such as cameras, radio detection and ranging (RADAR), light detection and ranging (LIDAR), and ultrasonic sensors for lane keeping purposes as well as GPS to assist navigation. To illustrate the importance of sensor redundancy, consider a short-term loss of a GPS signal in a CAV as it passes through a tunnel. In such a scenario, information from redundant sensors such as the inertial measurement unit (IMU), RADAR, and LIDAR can be used to approximate vehicle location until all systems are online again. In this example, sensor redundancy proves useful since sensors collecting the same data are not affected similarly by environmental factors; e.g., the factors that lead to a lack of access to GPS signal do not affect RADAR. Additionally, different types of sensors collecting the same data may have various degrees of precision as well as various levels of vulnerability to different cyber attack types. For instance, if a vehicle's machine vision, used for obstacle detection through video image processing, is attacked by using a high-brightness infrared LED, the redundant obstacle detection sensors including RADAR and LIDAR would be unaffected. Hence, sensor redundancy can lead to improved, dynamic sensor fusion in which anomalous sensor readings, due to either faults or attacks, can be discarded while the normal data is being fused to increase the reliability of the fused data.

A large body of work exists that examines various methods to detect anomalies, if they occur, and/or identify their source; however, only a limited number of these studies are focused on CAVs and ITS. Table A.1 in Appendix A summarizes some of the important works related to anomaly detection and identification in CAVs. Several studies employ distance-related metrics such as the Mahalanobis distance, affinity propagation clustering, and graph theory to detect in-vehicular network intrusions and faulty sensors (Yang et al., 2016; Lin et al., 2010; Khalastchi et al., 2011; Park et al., 2015). Also, Kalman filtering Kalman (1960) has been used in numerous applications for fault detection (Foo et al., 2013; Wei et al., 2010). In addition, some recent studies have employed deep learning techniques such as convolutional neural network (CNN) (Schmidhuber, 2015), recurrent neural network (RNN) (Taylor et al., 2016), and multilayer perceptron (MLP) models to detect anomalies in autonomous agriculture equipment vision and malicious CAN packets in modern vehicles (Christiansen et al., 2016; Kang and Kang, 2016). Deep learning techniques can be implemented on raw data and therefore do not require data abstraction. Lastly, Bezemskij et al. (2017) and Müter and Asaj (2011) employed Bayesian networks and signal entropy to detect anomalies in in-vehicular networks and autonomous robotic vehicles. However, these methods require synchronized data sources and high-volume attacks to perform well.

Several gaps are apparent in the literature. First, to the best of our knowledge, there is a lack of deep learning implementations in anomaly detection and identification for CAVs. Data are becoming more readily available and deep learning models are renowned for their performance using large datasets, therefore such models may be able to outperform traditional anomaly detection techniques such as Kalman filtering with failure detectors. In addition, there is a lack of comprehensive frameworks combining different anomaly detection and identification methods that incorporate the strengths and negate the weaknesses of the individual anomaly detection methods in CAVs. Lastly, applications focusing on real-time detection and identification of anomalous information (such as cyber attacks and/or faulty sensors) are limited.

Before mass implementation of CAVs into the transportation system, we need to ensure that the design of CAVs is resilient to cyber attacks and faulty equipment. This study assumes that the participating vehicles are of levels 4 and 5 automation, as defined by the National Highway Traffic Safety Administration (NHTSA) (NHTSA, 2013). Our main objective in this study is to detect anomalous sensor behavior and identify the source anomalous sensor in real-time for CAVs to assure the high reliability of fused data. Our framework is generic in that a 'sensor' may refer to any of the on-board sensors in a CAV, or another connected vehicle or roadside unit (RSU) that is communicating with the CAV. Specifically, we develop a holistic and generic framework by combining a deep learning technique, i.e., CNN, and Kalman filtering with a χ^2-detector, and investigate their ability to detect and identify various types of anomalous behavior in real-time. In addition, we perform various experiments to investigate the effects of anomaly type, magnitude, and duration.

Anomalous sensor readings, caused by attacks or failures, can present themselves in different ways. Several network attack taxonomies are available in the literature. Bhuyan et al. (2014) summarize the taxonomy of intrusions or attacks in computer network systems, which encompass CAVs. Also, several faulty sensor behaviors are discussed in (Sharma et al., 2010). We consider the anomalous sensor behavior resulting from both false injection attacks and sensor failures. According to the literature, anomalous sensor behavior can be represented by the five main following types:

1. Instant: A sharp, unexplained change in the observed data between two successive sensor readings.

2. Constant: A temporarily constant observation that is different from the "normal" sensor readings and is uncorrelated to the underlying physical phenomena.

3. Gradual drift: A small and gradual drift in observed data during a time period. It can result in a large discrepancy between the observed data and the true state of the system in time.

4. Bias: A temporarily constant offset from the sensor readings.

5. Miss: Lack of available data during a time period.

In this work, consistent with literature (Bhuyan et al., 2014; Sharma et al., 2010), we focus on detection and identification of anomalous behavior, caused by either cyber attacks or faulty sensors, resulting in 'instant,' 'constant,' 'gradual drift,' and 'bias.' These types of anomalies are some of the most dangerous for CAVs (Petit and Shladover, 2015; Mo et al., 2010). In this work, we do not explicitly account for 'miss,' which can result from DoS attacks preventing the exchange of information. However, note that 'miss,' depending on its duration, can be viewed as 'instant' or 'constant' behaviors, where the sensor reading is non-existent instead of showing a wrong value. Hence, it can partially be addressed using the same methods for detecting 'instant' or 'constant' behaviors. Regardless, we acknowledge that the considered anomaly types may not encapsulate *all* possible types of anomalies expected to occur in CAVs.

In this work, we develop an anomaly detection approach through combining a deep learning method, namely convolutional neural network (CNN), with a well-established anomaly detection method, Kalman filtering with a χ^2-detector, to detect and identify anomalous behavior in CAVs. Our main contributions are as follows: (1) We develop an anomaly detection and identification approach based on convolutional neural networks (CNN), applied to time-series data obtained from multiple sensors. Our use of the CNN for anomaly detection in time-series data is novel, where we generate 'images' from a continuous feed of real-time raw sensor data from a fixed-width sliding window and classify these images as anomalous or normal; (2) We develop a new generic anomaly detection and identification approach through combining CNN with a well-established anomaly detection method, i.e., Kalman filtering with a χ^2-detector. The resulting CNN-empowered KF (CNN-KF) framework can effectively detect and identify sensor anomalies.

1.2 Methods

In this section, we first discuss the two models that form the building blocks of our framework, namely the CNN model and the Kalman filter with a χ^2-detector model (referred to as the KF model throughout), developed independently to detect anomalies caused by cyber attacks and/or faulty equipment, in a CAV trip. Next, we develop a framework that combines the two methods in order to improve detection and identification capabilities by relying on their respective individual strengths. CNN was mainly selected due to its ability to capture temporal patterns, relationship between various sensors, and its capability to automatically extract features while weight sharing. All these make CNN particularly suitable as large amounts of data are becoming available. However, there is always a risk of unknown/unseen patterns going undetected when relying only on CNNs. Hence, using an architecture that combines CNN and KF can provide an additional level of reliability for the task at hand, as CNN and KF are complementary in their ability to detect anomalies. It is worth noting that we also explored recurrent neural networks (RNNs) with long short-term memory (LSTM) units; however, CNN consistently outperformed RNN in all preliminary experiments. This is partly because in this particular application, there are many normal values between consecutive anomalous values, which generally makes it hard for RNN to distinguish between anomalous and normal values in an extended sequence of data (Malhotra et al., 2015).

In general, the inputs to the model are the data collected from sensors, reading the same or highly correlated physical quantities. Based on the input data, at every time step, e.g., a few milliseconds (ms), outputs are generated as to whether anomalies are present (detection) and if so, which sensor reading(s) are erroneous (identification). Consequently, erroneous data can be excluded and normal data can be seamlessly fused to support CAV operation. Please note that all notation used are summarized in Table A.2 in Appendix A.

1.2.1 Kalman Filter

As discussed, Kalman filter combined with a failure detector is a well-established, widely used method for fault detection and identification in time-series data. In order to detect and identify anomalous sensor readings, we use an adaptive Kalman filter with a χ^2-detector to filter out process and measurement noise. Specifically, we assume our physical system is a discrete-time linear time-invariant system in the following form:

$$x(k) = Ax(k-1) + w(k-1) \tag{1.1}$$

where $x(k) \in \mathbb{R}^m$ is the vector of state variables at time k, $w(k) \in \mathbb{R}^m$ is the process noise at time k, and $A \in \mathbb{R}^{m\times m}$ is the state-transition matrix.

As discussed, we consider redundant sensor in this study. Let n denote the number of these sensors. That is, we consider n local subsystems, corresponding to the redundant sensors, with measurement matrices $H(k) \in \mathbb{R}^{p\times m}$ and sensing model:

$$z_i(k) = H(k)x(k) + v_i(k),\ i = 1, 2, ..., n \tag{1.2}$$

where $v_i(k) \in \mathbb{R}^p$ is zero mean Gaussian white noise sequences associated with the process and the measurement. The covariance matrices of $v_i(k) \in \mathbb{R}^p$ and $w(k)$ are $R_i(k)$ and $Q(k)$, respectively. We assume $v_i(k)$ and $w(k)$ are independent. In equation (1.2), $z_i(k) = [z_{i,1}(k), z_{i,2}(k), ..., z_{i,p}(k)]^T \in \mathbb{R}^p$ is a vector of sensor measurements for subsystem $i \in \{1, ..., n\}$. We assume all n subsystems have the same measurement matrix $H(k)$ and the readings across all subsystems are synchronized.

For each subsystem, a Kalman filter is used to estimate the state vector $x(k)$ from sensor reading $z_i(k)$. Kalman filter consists of two phases, i.e. prediction and update. The prediction phase advances the state estimate before the next measurement, and the update phase corrects the state estimate based on the measurement.

Let $\hat{z}(k|k-1)$ denote the predicted value of measurement at time k, $P(k|k-1)$ denotes the error covariance matrix of predicted state, and $\nu(k)$ denote the innovation, i.e., the difference between the measurement $z(k)$ and the predicted value of measurement at time k,

$$\nu(k) = z(k) - \hat{z}(k|k-1). \tag{1.3}$$

Also let $S(k)$ denote covariance matrix of innovation. In practice, covariance matrices R and Q are generally unknown a priori. Thus, we apply an adaptive Kalman filter to approximate these matrices (Mohamed and Schwarz, 1999). Specifically, we use a moving estimation window of size M to adaptively estimate R and Q matrices according to the innovation sequence within the time window, i.e.,

$$\begin{aligned} \hat{R}(k) &= \hat{C}_\nu(k) - H(k)P(k|k-1)H(k)^T, \\ \hat{Q}(k) &= K(k)\hat{C}_\nu(k)K(k)^T, \end{aligned} \tag{1.4}$$

where

$$\hat{C}_\nu(k) = \frac{1}{M}\sum_{j=k-M}^{k-1} \nu(j)\nu(j)^T. \tag{1.5}$$

We use a χ^2-detector to construct χ^2 test statistics, to determine whether the new measurement falls into the gate region with the probability determined by the gate threshold γ, defined as

$$V_\gamma(k) = \{z :(z - \hat{z}(k|k-1))^T S(k)^{-1}(z - \hat{z}(k|k-1)) \leq \gamma\}. \tag{1.6}$$

The χ^2 test statistics for each local subsystem is defined as

$$t(k) = \nu(k)^T S(k)^{-1}\nu(k) \tag{1.7}$$

It is easy to show that under Gaussian assumption the test statistic has a χ^2 distribution with p degrees of freedom, where p is the number of components of the measurement vector. However, in practice, usually w and v_i do not follow Gaussian distributions, and parameter γ has to be selected empirically. Hence, the threshold γ for $t(k)$ and the time window size M can be tuned.

Selection of the threshold γ is a trade-off between sensitivity of the trained model (i.e., the proportion of correctly identified anomalies), and the false-alarm rate. For each experiment in our experiment section, we select γ using a grid search within the range $\{1, 2, ..., 50\}$, and select the value of γ resulting in the highest F1 score.

The window size M is a parameter that allows for the control of smoothing short-term fluctuations in the detector. To select the best value for M, we performed a grid search. Specifically, for various values of M in our grid search, we computed the Area Under the ROC Curve (AUC) on a validation dataset. The results suggested that $M \in \{10, 15, 20\}$ provides robust results and high AUC (≈ 0.96). The AUC values within this range are similar. Hence, consistent with previously published work (e.g., Loebis et al. (2004)), we selected the window size $M = 15$ epochs for our experiments.

Once a faulty measurement stream has been identified, in order to ensure the future estimate is reliable, the measurement stream should be rejected at once and not fused with other measurements to ensure that the information generated through data fusion is not contaminated.

1.2.2 CNN

To apply CNN for real-time detection and identification of anomalous sensor behavior, we use a fixed-width sliding window on input data from all sensors measuring the same quantity, either directly or indirectly, where conversions or combining with other sensors may be required to infer the value of the quantity. At every epoch, as new observations are collected from sensors, the sliding window shifts to include these latest observations. Hence, the input to CNN is a series of 'images' from the continuous feed of raw sensor data during a CAV trip. For instance, consider three sensors (e.g., GPS, accelerometer, and transmission vehicle speed sensor) measuring vehicle speed at the sampling interval of 0.1 seconds. Hence, an image of size 3×10 would include the data collected from the three sensors during the last one second of the trip. The CNN therefore utilizes the data from multiple sensors simultaneously for detection and identification of anomalous values.

CNN models are trained to evaluate these images to detect and identify anomalies in real-time. Specifically, a sliding window is used on retrospectively collected data from sensors to produce images for training and testing. Because the goal is both to detect and to identify anomalies, for each sensor we train a separate model using labeled images, i.e., supervised learning. That is, if an anomaly is present in an image constructed with the data from the sensor of interest, the response variable is set to 1; otherwise, it is set equal to 0. Once separate models are trained to identify anomalies for each sensor, a logical OR operator on the outcomes of the all such models determines whether anomalous readings are detected across all sensors.

In our experiments, for each CNN model, a popular image recognition architecture from the literature is adopted (Krizhevsky et al., 2012). The parameter values for this architecture are then selected based on a number of experiments performed to maximize anomaly detection and identification performance on a validation set. In short, we used three convolution layers with max-pooling, followed by two fully connected layers with random dropout between the layers. A 1×2 pool size is used and 40, 60, and 60 filters are used for convolutional layers one to three, respectively. Also, a random dropout rate of 0.1 and batch size of 128 is used to train the CNN models. Furthermore, rectified linear unit (ReLU) activation functions are used and the Adam optimizer for Tensorflow in Python is implemented to minimize binary cross-entropy (Kingma and Ba, 2014). The following parameters were used for the Adam optimization algorithm: learning rate, $\alpha = 0.001$, exponential decay rates, $\beta_1 = 0.9$, $\beta_2 = 0.999$, and a fuzz factor, $\epsilon = 10^{-8}$.

It is widely acknowledged that deep learning models such as CNNs are often subject to 'overfitting' during the training process (Krizhevsky et al., 2012; Srivastava and Salakhutdinov, 2014). To reduce the risk of overfitting, in addition to random dropouts, we use early stopping to monitor the accuracy of the validation set with a patience of 200 epochs. Therefore, when training a CNN model, starting from any training epoch, if the validation accuracy during the following 200 epochs does not increase, training is terminated and the model corresponding to 200 training epochs ago, which resulted in the highest validation accuracy, is selected.

1.2.3 CNN-Empowered Kalman Filter (CNN-KF)

In order to further improve upon the detection and identification performances of the individual KF and CNN models, we develop a new framework that relies on both CNN and Kalman filter as shown in Figure 1.1. In this framework, first CNN models process the images of raw data from all sensors, which are obtained by using a sliding window over all sensor readings, to identify whether the readings from each sensor are normal or anomalous. Consequently, the sensors with anomalous behavior are excluded and the readings from normal sensors are separately fed into adaptive Kalman filters with failure detectors for further examination and anomaly detection. If Kalman filter detects anomalies that are missed by CNN, the readings from the corresponding sensors are excluded and the remaining normal data are fused in order to achieve a higher degree of reliability. As time passes and the vehicle continues its trip, if the sensors that presented anomalies go back to normal behavior, as verified by both CNN models and Kalman filters, the exclusion is no longer necessary and hence, the readings of the previously excluded sensors would be used in fusion again. In this study, we use a CNN-empowered Kalman Filter (CNN-KF), as opposed to a Kalman Filter empowered CNN (KF-CNN), mainly because having the Kalman filter in the last layer of learning allows for the reliable fusion of the non-anomalous sensor values (Schmidhuber,

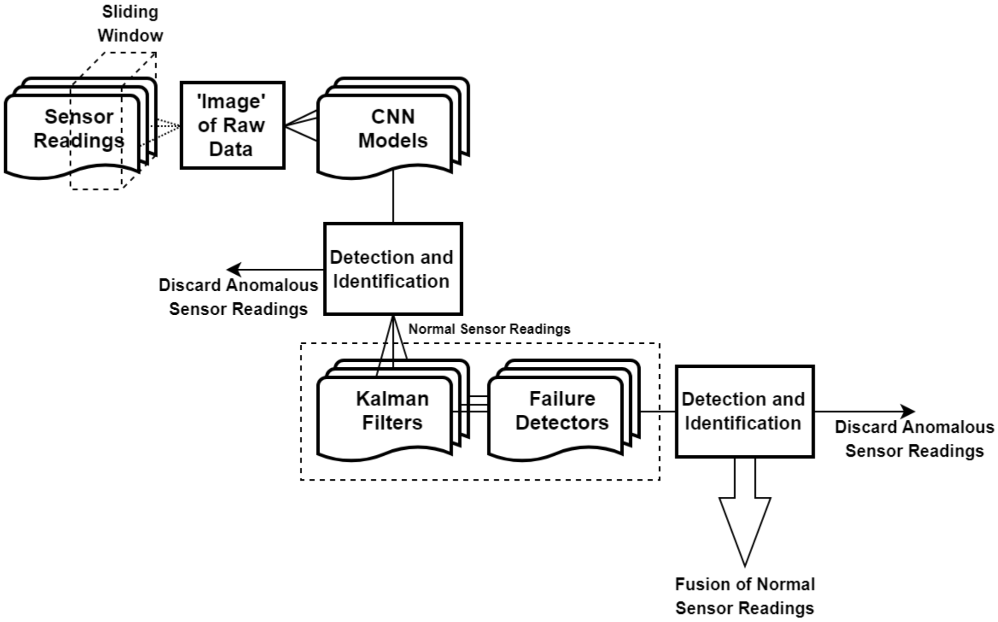
Sliding Window
Sensor Readings
'Image' of Raw Data
CNN Models
Detection and Identification
Discard Anomalous Sensor Readings
Normal Sensor Readings
Kalman Filters
Failure Detectors
Detection and Identification
Discard Anomalous Sensor Readings
Fusion of Normal Sensor Readings

Figure 1.1: Overview of the CNN-KF Framework. At each time epoch, the sensor readings collected within the past several time epochs are used as an input ‘image’ to the CNN-KF Framework. The data are first processed with a CNN to detect and identify sensors with anomalous readings. Next, the CNN-verified non-anomalous data are fed to the KF model to further detect and identify anomalies to increase reliability.

2015), which is important from a practical perspective for the application considered. In addition, based on our preliminary experiments, CNN-KF generally outperforms KF-CNN. Hence, we opted to present the results for CNN-KF only.

1.3 Data

The data for this study is obtained from the research data exchange (RDE) database for the Safety Pilot Model Deployment (SPMD) program (Bezzina and Sayer, 2014). This program was conducted with the primary objective of demonstrating CAVs, with the emphasis on connectivity technologies such as V2V and V2I communications in real-world conditions. The program recorded detailed and high-frequency (collected every 100ms) data for more than 2,500 vehicles over a period of two years. The data features extracted from the SPMD dataset used in this study include the in-vehicle speed (denoted as sensor 1), GPS speed (sensor 2), and in-vehicle acceleration (sensor 3) for one of the test vehicles with a trip length of 2,980 seconds. Note that the in-vehicle speed and GPS speed sensors observe the same quantity, namely, speed, whereas the acceleration sensor observes the vehicle's acceleration which can be used to infer speed.

Since there are no publicly available datasets for CAVs that include anomalies in sensor measurements, due to either attacks or faults, and the ground truths, we used simulation to generate datasets for our experiments. Specifically, we accounted for the four major anomaly types including instant, constant, gradual drift, and bias. We inject all four types of anomaly into each of the three speed-related (redundant) sensors. We assume the *onset* of anomalous values in sensors, due to either attacks or faults, occur independently. That is, we do not explicitly train models on datasets containing interdependent sensor failures or systemic cyber attacks on vehicle sensors. Additionally, we assume that no more than one anomaly can *start* in every time epoch, which is indeed very unlikely considering that sensors are generally reliable, and attacks/faults to sensors occur independently. However, dependent on the types, onset times, and durations of anomalies, multiple sensors may be anomalous at the same time.

There is existing work that illustrates the sensors considered in our numerical study, i.e., speed and acceleration sensors, are vulnerable to cyber attacks or faults (e.g., see Petit and Shladover (2015), Trippel et al. (2017), Currie (2015)). For in-vehicle speed and acceleration sensors, an injection attack through the CAN bus or the on-board diagnostics (OBD) system, could give rise to the four types of anomalies considered in this work. Also, for the in-vehicle acceleration sensor, an acoustic injection attack could result in anomalous sensor values. Lastly, for the speed measurement from the GPS, both the operating environment of the vehicle and GPS spoofing/jamming attacks may result in anomalous sensor values.

We generate various datasets for our experiments at 1% or 5% rates of anomalies, denoted by α. We simulate the anomalies to occur at randomly selected onset times (discretized into 100ms) to randomly selected sensors. To simulate the corresponding attacks/faults, these anomalies are then added to each affected sensor's 'base value,' i.e., the normal sensor readings in the original dataset indicating the traveling speed of the CAV at the time that the anomaly was introduced. Algorithm 1 presents the pseudo code used for simulating the anomalies. Note that vectors V_i and V_i', $i \in \{1, 2, \ldots, n\}$, denote non-anomalous and anomalous readings for sensor i, respectively. To facilitate thorough experiments, we vary the simulated anomalies in type, magnitude and/or duration when generating the datasets.

In addition, dependent on the experiment, we generate datasets where we randomly sample from a set of one or all anomaly types. The exact types of anomalies considered as well as their magnitude (and duration) will be discussed in detail for each experiment in Section 1.4.

Algorithm 1 Anomaly generation process

```
$\alpha \leftarrow$ anomaly rate; $n \leftarrow$ number of sensors
for time epoch $t \in T$ do
    if $\mathcal{U}(0,1) \leq \alpha$ then
        $\zeta \leftarrow \mathcal{U}(0,1)$
        for $i \in \{1, 2, \dots, n\}$ do
            if $\zeta \geq \frac{i-1}{n}$ and $\zeta < \frac{i}{n}$ then
                Generate anomaly; $V_i' \leftarrow V_i +$ anomaly
            end if
        end for
    else
        $V_i' \leftarrow V_i, \;\; i \in \{1, 2, \dots, n\}$
    end if
end for
```

1.4 Results

In this section, we perform various analyses to investigate the anomaly detection and identification performance of the three models discussed in Section 1.2. Specifically, we present the results obtained when using Kalman filter (KF) and CNN alone, and compare their performance to highlight their respective capabilities. In addition, we present the results obtained using CNN-KF framework and compare and contrast its performance with those of KF and CNN alone. We first investigate the detection performance of all three models when trained and tested for a single anomaly type in Section 1.4.1. We then investigate the detection and identification performance of the three models when trained and tested in the presence of all anomaly types in Section 1.4.2.

In our analyses, we use various datasets in which we simulate various types of anomalies of different durations and magnitudes to draw insights from the use of CNN, KF, and the CNN-KF models to detect/identify anomalies in real-time. Note that we need to select the parameter γ for KF models and also extensively train CNN models and tune their many parameters. Hence, for any given dataset, we use a training/validation/testing split of 60%/20%/20%. We use the training and validation sets to tune the model parameters. Next, to objectively evaluate their performance levels, we use the separate test sets for testing.

We evaluate the performance of the models in terms of accuracy, sensitivity, precision, and F1 score. Accuracy measures the overall proportion of correct predictions for normal and anomalous sensor values. Sensitivity assesses the proportion of correctly identified anomalous sensor values from the total number of anomalous sensor values. Precision measures the proportion of anomalous sensor values among those predicted as anomalous. Lastly, F1 score is the harmonic mean of sensitivity and precision. These metrics are particularly chosen as they measure the ability of the models to correctly differentiate between normal and anomalous sensor behavior. Note that these metrics are commonly used to evaluate the performance of classification models. Here, for consistency and to enable comparison of all models, we use the same metrics to evaluate the performance of CNN, KF, and CNN-KF models.

1.4.1 Models Under a Single Anomaly Type

In this section we compare the *detection* performance of the three models for the specific types of anomalies, as discussed in Section 1.1, namely, instant, constant, gradual drift, and bias. We generate various datasets, each with a specific type of anomaly, with anomaly rate $\alpha = 5\%$. For each dataset, we train and test CNN models to measure their performance in detecting the specific anomaly type. Because each sensor reading in our experiment is one dimensional, the state transition matrix A and measurement matrix H for KF are simply single values.

Instant

The instant anomaly type is simulated as a random Gaussian variable with mean and variance of zero and 0.01, respectively, that is scaled by a scalar $c \in \{25, 100, 500, 1{,}000, 10{,}000\}$, i.e., $c \times \mathcal{N}(0, 0.01)$, to capture various magnitudes. The resulting simulated value is added to the base value of sensor measurement for one epoch, i.e., 100 ms.

Table 1.1 illustrates the anomaly detection performance of the KF, CNN, and CNN-KF models. Considering the detection performance of KF and CNN models, the following is noted. In general the detection performance of the KF and CNN models increases across all metrics in the magnitude of the instant anomaly type, which is consistent with the intuition. For small magnitudes of anomalous sensor values, i.e., the first two rows in Table 1.1, the detection performance of the models are poor. However, in these cases the difference between the anomalous sensor values and non-anomalous sensor values are generally too small to pose any substantial risks to the operation of the vehicle. For magnitudes that may pose significant risk to the operation of the vehicle, i.e., rows 3–5, the models are able to detect anomalous behavior with high performance. As seen in the table, KF and CNN models have similar performance for instant anomalies with large magnitudes. The CNN models generally outperform KF models in terms of sensitivity, precision, and F1 score. Particularly, sensitivity is higher in CNN models, which can directly impact the reliability and safety of fused data in CAVs. A reason for this higher performance of CNN models compared to KF models is that when the anomalies are small enough, the attack will fall into the region of gating for the KF model, therefore it cannot be detected by the chi-square test, which results in a low sensitivity measure. Additionally, unlike the KF models that use the readings by a single sensor over time to detect any potential anomalies on that sensor, the CNN models use the readings from *all* sensors within a time window to detect anomalous behavior by each individual sensor. This redundancy in information improves the CNN performance when the anomaly magnitudes are small and therefore harder to detect.

Considering the anomaly detection performance of the CNN-KF model for the instant anomaly type, the following is noted. Similar to the results for KF and CNN models, the detection performance across all metrics increases in anomaly magnitude. Furthermore, it is seen that, in general, the CNN-KF model improves upon the detection performance of both KF and CNN models as reported in Table 1.1. For instance, for instant anomalies of magnitude $25 \times \mathcal{N}(0, 0.01)$ added to the base value (row 1), it is seen that sensitivity and F1 score of the CNN-KF model respectively increase by 13.1% and 18.9% over the KF model,

Table 1.1: Detection performance of instant anomaly type for the KF, CNN and CNN-KF models.

	KF (%)				CNN (%)				CNN-KF (%)			
Anomaly Magnitude	Acc	Sens	Prec	F1	Acc	Sens	Prec	F1	Acc	Sens	Prec	F1
base value + 25 × $\mathcal{N}(0, 0.01)$	95.7	38.4	65.8	48.5	79.1	49.9	97.7	66.0	80.0	51.5	97.6	**67.4**
base value + 100 × $\mathcal{N}(0, 0.01)$	98.6	78.4	93.6	85.3	93.5	85.7	98.1	91.5	93.6	86.2	97.9	**91.7**
base value + 500 × $\mathcal{N}(0, 0.01)$	99.7	95.6	99.0	97.3	98.2	95.8	99.8	97.8	98.3	96.0	99.7	**97.8**
base value + 1,000 × $\mathcal{N}(0, 0.01)$	99.8	96.2	100	98.1	98.7	97.1	99.8	98.4	98.8	97.1	99.8	**98.4**
base value + 10,000 × $\mathcal{N}(0, 0.01)$	99.9	100	99.7	**99.8**	99.6	99.1	100	99.5	99.7	99.2	99.8	99.5

Table 1.2: Detection performance of constant anomaly type for KF, CNN and CNN-KF models.

		KF (%)				CNN (%)				CNN-KF (%)			
Anomaly Magnitude	Dur	Acc	Sens	Prec	F1	Acc	Sens	Prec	F1	Acc	Sens	Prec	F1
base value + $\mathcal{U}(0, 5)$	3	98.5	91.4	98.8	**95.0**	94.5	89.1	99.8	94.1	94.9	89.9	99.6	94.5
base value + $\mathcal{U}(0, 5)$	5	98.5	94.9	98.5	**96.7**	94.6	90.7	99.2	94.8	95.1	91.7	99.0	95.2
base value + $\mathcal{U}(0, 5)$	10	97.8	96.0	98.5	**97.3**	95.5	93.7	99.2	96.4	96.2	94.9	99.1	97.0
base value + $\mathcal{U}(0, 3)$	10	95.7	92.5	96.9	94.6	94.8	92.9	98.8	95.8	95.3	93.9	98.7	**96.2**
base value + $\mathcal{U}(0, 1)$	10	88.8	78.8	92.4	85.1	90.1	85.2	99.1	91.6	91.2	87.8	98.6	**92.7**

and by 1.6% and 1.4% over the CNN model. Note that the F1 scores of CNN-KF are larger that those of CNN in rows 4–5; these numbers only appear to be the same as the numbers in the table are rounded to one decimal place. Lastly, note that for anomalies with very large magnitudes (row 5), high performance is found in all models, especially for KF.

Constant

The constant anomaly type is simulated as a temporarily constant observation that is different compared to the “normal” sensor readings. Similar to the previous case, we simulate the magnitude of the anomaly that is added to the base value at the onset of the anomaly using a random variable to capture various magnitudes in any given experiment. Specifically, the magnitude of a given anomaly is sampled from a uniform distribution $\mathcal{U}(0, c)$, where $c \in \{1, 3, 5\}$. In addition, here we account for various durations of the anomalous behavior. Let d denote the number of epochs during which the anomalous behavior is present, where we use $d \in \{3, 5, 10\}$.

Table 1.2 shows the results of the constant anomaly type for the KF, CNN, and CNN-KF models. As seen in rows 1–3, the performance of the KF and CNN models generally increases in anomaly duration, given that anomaly magnitudes are drawn from the same random variable. In these cases, because the anomaly magnitude can be somewhat large, KF generally outperforms CNN. Similarly, as seen in rows 3–5, given a fixed anomaly duration (with $d = 10$), the performance of both KF and CNN models are typically better when the anomaly magnitudes are generally larger. In general, similar to the detection performance of the instant anomaly type, the KF model slightly underperforms compared to the CNN model in the case of low magnitude anomalies (rows 4–5) and slightly outperforms the CNN model in detecting anomalies with stochastically larger magnitudes (rows 1–3). In addition, the CNN model generally illustrates a more consistent detection performance across various anomaly magnitudes and durations compared to KF.

Considering the anomaly detection performance of the CNN-KF model for the constant anomaly type, the following is noted. The results illustrate that the CNN-KF model outperforms the KF model when the magnitude of anomalies is relatively small, i.e., in rows 4–5. In addition, the CNN-KF model clearly outperforms the CNN model with respect to accuracy, sensitivity, and F1-score across all experiments. Note that the magnitude of gain in performance is larger when comparing CNN-KF with KF, as opposed to when comparing CNN-KF with CNN. For instance, in row 5, using the CNN-KF model, as opposed to the KF model, increases the sensitivity and F1 score by up to 9% and 7.6%, respectively. Compare these numbers, respectively, with the observed increases of up to 2.6% and 1.1% when using the CNN-KF model, as opposed to the CNN model. Note that the improved performance of CNN-KF model over the CNN model is mainly due to the ability of the Kalman filtering aspect of the CNN-KF model to detect the onset of anomalous behavior faster than that of the CNN model, especially for larger anomaly magnitudes. Lastly, similar to the results in Table 1.1, it is seen that KF outperforms CNN-KF for anomalies with large magnitudes.

Gradual drift

The gradual drift anomaly type is simulated by adding a linearly increasing set of values to the base values of the sensors. Specifically, we use a vector of linearly increasing values from 0 to $c \in \{2, 4\}$, corresponding to 2 m/s and 4 m/s, respectively, denoted by the function $linspace(0, c)$. In addition, here again we account for various durations of the anomalous behavior, namely, $d \in \{10, 20\}$. For instance, when $c = 4$ and $d = 20$, a linearly increasing

Table 1.3: Detection performance of gradual drift anomaly type for the KF, CNN and CNN-KF models.

		KF (%)				CNN (%)				CNN-KF (%)			
Anomaly Magnitude	Dur	Acc	Sens	Prec	F1	Acc	Sens	Prec	F1	Acc	Sens	Prec	F1
base value + $\mathit{linspace}(0,4)$	10	94.7	91.4	95.3	93.4	94.4	92.0	99.3	95.5	94.7	93.1	99.2	**96.1**
base value + $\mathit{linspace}(0,4)$	20	92.2	93.0	94.7	93.8	95.7	95.1	99.4	97.2	96.0	95.6	99.3	**97.4**
base value + $\mathit{linspace}(0,2)$	10	90.3	86.5	89.3	87.9	92.7	89.1	99.4	94.0	93.0	89.6	99.3	**94.2**
base value + $\mathit{linspace}(0,2)$	20	83.1	86.5	86.9	86.7	92.8	92.0	98.7	95.3	93.7	93.2	98.7	**95.9**

Table 1.4: Detection performance of bias anomaly type for KF, CNN and CNN-KF models.

		KF (%)				CNN (%)				CNN-KF (%)			
Anomaly Magnitude	Dur	Acc	Sens	Prec	F1	Acc	Sens	Prec	F1	Acc	Sens	Prec	F1
base value + $\mathcal{U}(0,5)$	3	98.7	93.4	98.1	**95.7**	94.0	87.8	99.8	93.4	94.6	89.3	99.5	94.2
base value + $\mathcal{U}(0,5)$	5	98.2	94.6	97.5	**96.0**	94.2	89.2	99.9	94.3	94.8	90.6	99.6	94.9
base value + $\mathcal{U}(0,5)$	10	97.3	95.3	98.0	96.6	94.4	91.3	99.8	95.4	95.9	94.4	99.1	**96.7**
base value + $\mathcal{U}(0,3)$	10	95.9	93.2	96.5	94.8	92.4	88.4	99.6	93.7	94.4	92.6	98.6	**95.5**
base value + $\mathcal{U}(0,1)$	10	90.1	81.0	93.8	86.9	85.0	77.6	98.6	86.8	88.0	84.8	95.9	**90.0**

speed of up to 4 m/s (i.e., with an intercept of 0 and a slope of 4/19) is added to the base speed of the CAV over the next 20 epochs (i.e., 2 seconds).

Table 1.3 shows the results of the gradual drift anomaly type for the KF, CNN, and CNN-KF models. Gradual drift is one of the most difficult anomalies to detect since it increases sensor values gradually, therefore making it challenging to detect the onset of anomalous sensor behavior and differentiating it from normal behavior. Nevertheless, KF and CNN perform reasonably well across various values of magnitude and duration considered. Similar to the constant anomaly type, the detection performance of the CNN model increases in duration and magnitude of the anomalous sensor behavior. Furthermore, as seen in the table, CNN models consistently outperform KF models across all magnitudes and durations for the gradual drift anomaly type. That is mainly because the sliding window implementation of CNN provides additional opportunities to detect gradual drift anomalies compared to KF. This generally leads to an improved detection performance, even if the anomaly onset is missed by CNN, which is often the case for gradual drift anomalies.

Considering the anomaly detection performance of the CNN-KF model for the gradual drift anomaly type, the following is noted. As seen in Table 1.3, this model outperforms both KF and CNN models across all experiments. For instance, in row 4, using the CNN-KF model, the sensitivity and F1 score respectively increase by 6.7% and 9.2% compared to the KF model, and by 1.2% and 0.6% compared to the CNN model.

Bias

The bias anomaly type is simulated as a temporarily constant offset from the baseline sensor readings. Similar to the previous cases, we simulate the magnitude of the anomaly using a random variable to capture various magnitudes in any given experiment. Specifically, the magnitude of a given anomaly is sampled from a uniform distribution $\mathcal{U}(0, c)$, where $c \in \{1, 3, 5\}$. In addition, here we account for various durations of the anomalous behavior, where the sampled magnitude is added to all true sensor readings during the specified duration to generate the anomalous readings. Let d denote the number of epochs during which the anomalous behavior is present, where we use $d \in \{3, 5, 10\}$.

Table 1.4 shows the results of the bias anomaly type for the KF, CNN, and CNN-KF models. As seen in rows 1–3, the performance of the KF and CNN models generally increases in anomaly duration, given that anomaly magnitudes are drawn from the same random variable. Similarly, as seen in rows 3–5, given a fixed anomaly duration (with $d = 10$), the performance of both KF and CNN models generally decrease when the magnitude of anomalies stochastically decrease. Interestingly, different from previous cases, in this case the KF model consistently outperforms the CNN model in all cases examined.

Considering the anomaly detection performance of the CNN-KF model for the bias anomaly type, the following is noted. The results illustrate that the CNN-KF model outperforms the KF model when the magnitude of anomalies is relatively small and their duration is relatively long, i.e., in rows 3–5. In addition, the CNN-KF model clearly outperforms the CNN model with respect to sensitivity and F1-score across all experiments. The improved performance of CNN-KF model over the CNN model is mainly due to the ability of the Kalman filtering aspect of the CNN-KF model to detect the onset of anomalous behavior faster than that of the CNN model, especially for larger anomaly magnitudes.

In conclusion, as seen in Table 1.1, CNN-KF generally outperforms both CNN and KF in detecting the instant anomaly type. KF only outperforms CNN-KF when the magnitude of the anomaly is very large. As seen in Table 1.2, the CNN and CNN-KF models perform better for anomalies with smaller magnitudes. Similar to Table 1.1, KF performs better for anomalies with large magnitudes but less so for anomalies with small magnitudes. This is due to the fact that when the anomalies are small enough, they fall into the gating region of the KF model; therefore, they cannot be detected by the chi-square test. Also, as seen in Table 1.3, the CNN-KF model outperforms both KF and CNN models across all magnitudes and durations considered for the gradual drift anomaly type. This is mainly because CNN-KF combines the strength of CNN where the sliding window implementation provides additional opportunities for detection and the ability of KF in detecting the first few epochs of these anomalies. Lastly, as seen in Table 1.4 for the bias anomaly type, consistent with the results in Tables 1.1–1.3, the CNN-KF models perform well for anomalies with small magnitudes and long duration whereas KF performs better for anomalies with large magnitudes and a small duration.

1.4.2 Models Under Mixed Anomaly Types

In this section we investigate the performance of the models when applied in *detection* and *identification* of various types of anomalies as opposed to the single anomaly types considered in Section 1.4.1. First, we investigate the generalizability of the models presented in Section 1.4.1 with respect to unseen anomaly types to motivate the need to develop CNN-based models under mixed anomaly types. Next we develop new models, trained and tested in the presence of all four anomaly types, where the simulation is run multiple times to provide confidence intervals (CIs). Specifically, we present the mean performance along with the 95% CIs, and perform statistical tests to establish whether or not the observed improvements across models are significant. In addition, we analyze the effect of the rate at which anomalous sensor values may occur (at $\alpha = 5\%$ and $\alpha = 1\%$) on the performance of the models.

As seen in Section 1.4.1, CNN and CNN-KF models generally outperform KF models. However, note that in contrast to CNN models, KF models do not require much effort for training and they generalize well; only parameters γ and M need to be calibrated for KF models. Additionally, as we will demonstrate in this section, for CNN models to generalize well and correctly classify previously unseen observations, they require to be trained on representative training sets. However, in practice, CAV anomaly detection systems may encounter various instances of anomalies for which the models are not explicitly trained. This is particularly important for CAVs since these vehicles will be faced with numerous unfamiliar circumstances. Here we present the results of using the trained CNN models from Section 1.4.1 and testing them on datasets where all types of anomalous sensor values are present. We break down the results to present the performance of the models in terms of anomalous sensor values identification. The main objective of this analysis is to investigate the degree to which each of these models can generalize to detect/identify unseen anomalies.

Table 1.5 presents the performance of training CNN models on one type of anomaly and using them to identify anomalous sensor values where all anomaly types are present. Each case presented across three rows provides the performance of a trained model on a particular training set with the given anomaly type. In the test dataset, the instant, constant, gradual drift, and bias anomalies are all present and are modeled using $1{,}000 \times \mathcal{N}(0, 0.01)$, $\mathcal{U}(0, 5)$ with $d = 10$ epochs, $linspace(0, 4)$ with $d = 20$ epochs, and $\mathcal{U}(0, 5)$ with $d = 10$ epochs, respectively. For instance, for the first case illustrated in Table 1.5, we train the CNN with the instant anomaly type where anomalies are sampled from $1{,}000 \times \mathcal{N}(0, 0.01)$ and we test the model on the test set where all four anomaly types are present.

As seen in Table 1.5, training the CNN model using only instant anomalous sensor values results in poor performance, and particularity low sensitivity. This is expected, since the constant, gradual drift, and bias anomaly types are very different from the instant anomaly type in both magnitude and duration. Also, note that the identification performance generally varies across sensors. Specifically, for sensor 3 (i.e., in-vehicle acceleration), across all experiments, it is seen that the performance metrics are worse than those for the other two speed sensors. This is partly due to the large variability in consecutive acceleration measurements compared to the other two speed sensors that tends to report much smoother readings over time. Lastly, as seen in the table, using the CNN model that is trained on either constant, gradual drift or bias anomaly type results in reasonable performance across all sensors with an F1 score of up to 90.1%.

In the next set of experiments, we train the models using datasets in which all types of anomalous sensor values are present, to estimate the models' anomaly identification performance in practice. Table 1.6 illustrates the identification performance and the 95% CIs across 10 simulation runs, when the anomaly rate is set to 5% ($\alpha = 5\%$) and all types of anomalies are present. Similar to the results obtained for the specialized models in Section

Table 1.5: Identification performance of training CNN models on one type of anomalous sensor values and testing them to identify anomalous sensor values where all anomaly types are present. The reported values are in percentages.

Anomaly Type Used in Training	Sensor	Acc	Sens	Prec	F1
Instant, 1,000×$\mathcal{N}(0, 0.01)$	1	91.1	64.1	99.3	77.9
	2	88.1	59.0	95.0	72.8
	3	85.4	44.1	99.9	61.2
Constant, $\mathcal{U}(0, 5)$, $d = 10$	1	95.3	87.0	93.4	90.1
	2	90.9	70.8	94.0	80.7
	3	89.2	65.2	91.1	76.0
Gradual drift, $\mathit{linspace}(0, 4)$, $d = 20$	1	92.5	76.4	91.5	83.3
	2	90.6	70.2	93.5	80.2
	3	88.2	66.7	85.0	74.7
Bias, $\mathcal{U}(0, 5)$, $d = 10$	1	94.8	88.3	90.4	89.3
	2	91.7	70.6	98.1	82.1
	3	89.3	61.7	96.2	75.1

1.4.1, as seen in Table 1.6, the CNN model generally outperforms the KF model, especially with respect to sensitivity and F1 score. Furthermore, the CNN-KF model improves upon the performance of both KF and CNN models, especially with regard to F1 score as highlighted in the table. We perform paired t-tests and one-way ANOVA tests to investigate the statistical significance between the identification performance with respect to F1 score between all pairs of models, i.e., KF and CNN models, KF and CNN-KF models, and CNN and CNN-KF models. The p-values obtained indicate statistical significance at 5% level (p-value $<$ 0.05) across all tests performed.

Figure 1.2 presents the in-vehicle speed sensor readings, with and without superimposed anomalous sensor values, during a 3-second time window of a CAV trip in one of the test sets, and illustrates the instances at which the anomalous sensor values were detected by each of the three models. In this example, the anomaly is of type constant, has a relatively small magnitude of 0.17 m/s (i.e., results in anomalous sensor readings of 18.66 m/s compared to the base speed of 18.49 m/s at the anomaly onset), and lasts for a period of $d = 10$ epochs or 1 second, i.e., from 980 to 989 time epochs, into the CAV trip. As seen in the figure, the KF and CNN models both fail to identify all anomalous sensor readings during this 1 second period. In contrast, CNN-KF model identifies all anomaly instances. Note that, in this case, the anomalous sensor values caused by the constant anomaly type are very small

Table 1.6: Identification performance and the 95% CIs across 10 different executions for all three models, at the anomaly rate of $\alpha = 5\%$ and in the presence of all types of anomalies. P-values indicate statistical significance at 5% level using paired t-test and one-way ANOVA tests, between the identification performance of all pairs of models. The reported values are in percentages.

Model	Sensor	Acc	Sens	Prec	F1
KF	1	97.8 ±0.2	90.5 ±1.4	95.9 ±1.1	93.1 ±0.7
	2	98.0 ±0.2	90.6 ±1.1	96.0 ±1.1	93.2 ±0.8
	3	96.1 ±0.3	85.1 ±2.6	89.0 ±1.8	86.9 ±1.4
CNN	1	98.0 ±0.3	93.3 ±0.7	99.5 ±0.2	96.3 ±0.4
	2	97.0 ±0.2	90.4 ±0.6	98.7 ±0.3	94.4 ±0.4
	3	94.7 ±0.5	83.3 ±1.3	97.6 ±1.0	89.8 ±0.8
CNN-KF	1	98.1 ±0.2	94.2 ±0.5	99.4 ±0.2	**96.7** ±**0.3**
	2	97.6 ±0.2	92.9 ±0.5	98.4 ±0.4	**95.5** ±**0.4**
	3	95.7 ±0.4	87.3 ±1.0	97.3 ±0.7	**92.0** ±**0.8**

compared to the base speed value, illustrating the effectiveness of the CNN-KF framework in detecting/identifying the anomalous sensor values.

Lastly, we investigate the effect of the anomaly rate α on the identification performance of the trained models. Table 1.7 illustrates the identification performance and the 95% CIs when the previously trained models are tested across 20 different test sets in which the anomaly rate is set to 1% ($\alpha = 1\%$) and all anomaly types are present. In this experiment we use a larger number of test sets compared to the previous experiment due to the low anomaly rate. Similar to the $\alpha = 5\%$ case illustrated in Table 1.6, the CNN model outperforms the KF model, and the CNN-KF model outperforms both the KF and CNN models. Specifically, the p-values obtained using paired t-test and one-way ANOVA tests indicate statistical significance at 5% level between the identification performance of all pairs of models with respect to F1 score. As seen in Tables 1.6 and 1.7, model accuracy increases when the rate of anomalous sensor values is at $\alpha = 1\%$, compared to $\alpha = 5\%$, as there are fewer anomalous instances to misclassify; however, F1 score generally decreases at $\alpha = 1\%$, compared to $\alpha = 5\%$. Note that these results are in general better than those obtained if the training sets

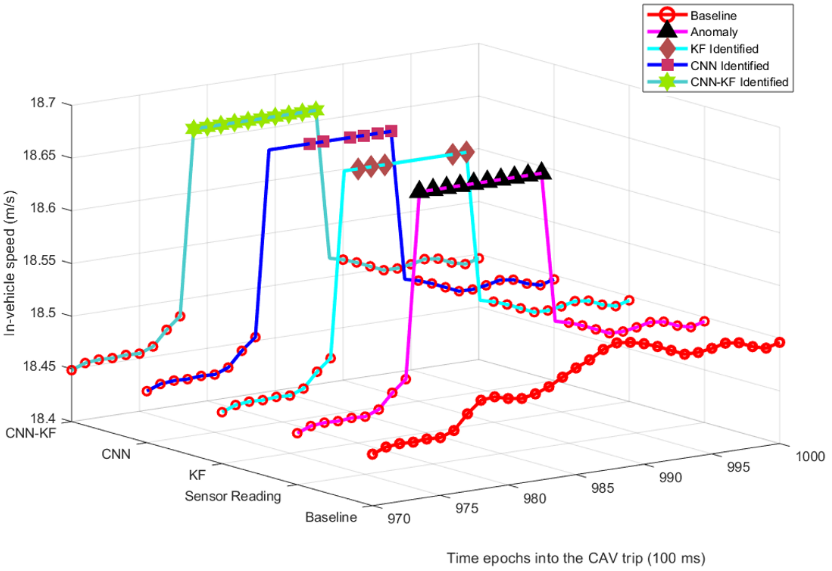

Figure 1.2: An example illustrating the performance of KF, CNN, and CNN-KF models in identifying anomalous sensor values of in-vehicle speed sensor readings during a 3-second time window of a CAV trip.

used were at $\alpha = 1\%$ anomaly rate, particularly for CNN and CNN-KF models. This is mainly because if the training set is highly unbalanced, classification models tend to favor the more representative class (in our case 'normal' readings) and hence, do not generalize well to detect anomalous sensor values. This is why when training a model on an unbalanced set, either oversampling or undersampling is utilized (Chawla et al., 2004; Park et al., 2016).

1.5 Discussion

The main objective of this study is to improve safety of CAVs and robustness of their decisions in the presence of faulty sensors or cyber attacks, which may pose significant risks to transportation network users. CAVs are expected to use a number of redundant sensors measuring the same parameters, e.g. speed or location, which can be used to detect and identify anomalous sensor values by comparing the data collected from the corresponding sensors. In addition, CAVs collect large volumes of data, often at 100ms or finer intervals, enabling the use of deep learning techniques to learn complex, nonlinear patterns in the data to improve overall detection/identification performance. We take advantage of these two

Table 1.7: Identification performance and the 95% CIs across 20 different executions for all three models, at the anomaly rate of $\alpha = 1\%$ and in the presence of all types of anomalies. P-values indicate statistical significance at 5% level using paired t-test and one-way ANOVA tests, between the identification performance of all pairs of models. The reported values are in percentages.

Model	Sensor	Acc	Sens	Prec	F1
KF	1	99.3 ±0.1	84.5 ±2.8	92.1 ±1.3	88.0 ±1.7
	2	99.3 ±0.1	84.8 ±3.1	92.7 ±1.8	88.5 ±2.3
	3	98.7 ±0.2	70.6 ±3.6	86.9 ±3.4	77.3 ±1.9
CNN	1	99.3 ±0.1	90.7 ±1.0	97.1 ±1.1	93.8 ±0.9
	2	99.1 ±0.1	89.8 ±1.3	95.0 ±1.5	92.2 ±0.9
	3	98.2 ±0.4	79.1 ±1.9	94.8 ±2.0	86.1 ±1.1
CNN-KF	1	99.3 ±0.1	91.3 ±0.9	96.7 ±1.1	**93.9** ±**0.8**
	2	99.1 ±0.1	90.9 ±1.0	94.8 ±1.4	**92.8** ±**0.9**
	3	98.5 ±0.3	83.2 ±1.9	95.0 ±1.9	**88.6** ±**1.1**

important features of CAVs by combining a deep learning technique, CNN, and a traditional anomaly detection technique, KF with a failure detector, to address the real-time anomalous sensor value detection and identification for CAVs. Our approach improves upon both CNN and KF models, when they are used separately, as it integrates their strengths.

Note that the developed models are able to perform detection and identification, not prediction. That is, they do not have the capability to preventively detect anomalous sensor values. However, the models are expected to be used in an online fashion, on high-frequency data (with the sampling frequency of approximately 100ms) to detect and identify anomalous sensor values. Therefore, if a sensor starts to transmit anomalous data, it can be identified and actions may be implemented within a fraction of a second to mitigate its effects.

Introducing sliding windows in CNN and KF-CNN models allows for evaluating sensor readings holistically and more than once, hence providing additional opportunities for detection and identification of anomalous sensor values. For instance, all models are at risk of missing bias and gradual drift anomaly types, particularly if the anomaly magnitudes are small. However, in CNN and CNN-KF, even if the onset of anomaly is initially missed, the anomaly is detected/identified after only a few time epochs, e.g., approximately in 300ms.

1.6 Conclusion and Future Work

The goal of this study is to develop an approach to detect/identify anomalous behaviors in CAVs to improve their safety. Our results show that the use of deep learning models such as CNN to detect/identify anomalous sensor values in CAV systems in real-time is a viable path and it can improve upon the well-established methods such as Kalman filtering with failure detectors. In addition, our results show that because of the inherent differences between CNN and KF, combining these approaches can build upon their individual strengths and hence result in an improved performance. More specifically, we show that by using a CNN-empowered KF on raw sensor data, it is possible to detect and identify anomalous sensor values in real-time with high accuracy, sensitivity, precision, and F1 score. This research contributes to the field of ITS safety as a whole since the success of ITS operations is heavily dependent on the safe operation of all its respective elements. In addition, CAV manufacturers and policy-makers may benefit from the observations in this study with regards to the value of having redundant information for a specific parameter such as the speed of a vehicle. As a result, more redundant sensors and information gathering devices may be implemented and considered in CAVs to increase their resiliency against anomalous sensor values. It is also expected that the CNN-KF framework presented in this study will be applied to various other sources of information in CAVs to increase their safety.

The study is subject to limitations. First, the anomalous sensor values used in the experiments, consistent with previous studies in the literature, are simulated, mainly because this type of data are not yet readily available. In addition, due to paucity of data on connected vehicles, the experiments are limited to on-board sensors. Although the framework is generic and can address anomaly detection/identification regardless of the data source, additional testing is needed as real data becomes readily available. To that end, it should be noted that the reported performance of the proposed CNN-based methods are only valid for those attack types whose effects can be reflected by the four anomaly types considered in this study.

Furthermore, in this study, we assume the *onset* of anomalous values in sensors, due to either attacks or faults, occur independently. Although we do not explicitly train models on datasets containing interdependent sensor failures or systemic cyber attacks on a vehicle's sensors, the framework is expected to still be able to detect such faults/attacks. To improve model performance under such scenarios, however, additional training using such data is required. Indeed, it is envisioned that real-world data would be available in the near future as a result of various ongoing pilot studies (Michigan, Wyoming, New York City, and Tampa) as well as the introduction of CAVs into society by companies such as Waymo, Uber, Audi, and Tesla.

In future work, it may be useful to distinguish between anomalous and malicious information, since this will influence the action taken to mitigate their effects. Also, it may be beneficial to also identify the type of anomaly occurring. This, in turn, will enable the development of certain real-time actions to minimize the impact of cyber attacks and/or faulty sensors, therefore contributing to the development of effective counter-measures.

Chapter 2

Optimal Switching Policy Between Driving Entities in Semi-Autonomous Vehicles

Disclosure: This chapter is based on a paper submitted by van Wyk et al. (2019) to Transportation Research Part C: Emerging Technologies.

van Wyk, F., Khojandi, A. and Masoud, N., 2019. Optimal Switching Policy Between Driving Entities in Semi-Autonomous Vehicles. Transportation Research Part C: Emerging Technologies.

My contributions to this paper include: (i) the development of the problem, (ii) reviewing the appropriate literature, (iii) the identification of study objectives, (iv) design and conducting of the numerical experiments, (v) majority of the writing responsibilities of the manuscript.

Abstract

In the future, autonomous vehicles are expected to safely move people and cargo around. However, as of now, automated entities do not necessarily outperform human drivers under all circumstances, particularly under certain road and environmental factors such as bright light, heavy rain, poor quality of road and traffic signs, etc. Therefore, in certain conditions it is safer for the driver to take over the control of the vehicle. However, switching control back and forth between the human driver and the automated driving entity may itself pose a short-term, elevated risk, particularly because of the out of the loop (OOTL) issue for humans. In this study, we develop a mathematical framework to determine the optimal driving-entity switching policy between the automated driving entity and the human driver. Specifically, we develop a Markov decision process (MDP) model to prescribe the entity in charge to minimize the expected safety cost of a trip, considering the dynamic changes of the road/environment during the trip. In addition, we develop a partially observable Markov decision process (POMDP) model to accommodate the fact that the risk posed by the immediate road/environment may only be partially observed. We conduct extensive numerical experiments and thorough sensitivity and robustness analyses, where we also compare the expected safety cost of trips under the optimal and single driving entity policies. In addition, we quantify the risks associated with the policies, as well as the impact of miss-estimating road/environment condition risk level by the driving entities, and provide insights.

2.1 Introduction

It is expected that connected and autonomous vehicles (CAVs) will increase road safety, reduce travel time, improve comfort, improve fuel efficiency and decrease fatal accidents by as much as 40% in the future (Fagnant and Kockelman, 2015; Guler et al., 2014). However, before transportation systems are fully connected and automated, there will be a transition period where the driver is required to retake control of the vehicle from the autonomous system at certain times under various circumstances (Campbell et al., 2018).

The Society of Automotive Engineers (SAE) has identified 6 levels of autonomy (levels 0 through 5) that reflect the nature of interactions between an automated vehicle and the driving environment as well as the degree of driver involvement (SAE, 2016). Level 0 refers to the driver performing all dynamic driving tasks. Level 1 automation entails assisted automation where advanced driver assistance systems (ADAS) perform steering, acceleration or deceleration. Level 2 automation is present if one or more assisted automation tasks are performed by the autonomous system where the driver is responsible for the monitoring of the driving environment and ultimately the control of the vehicle.

In level 3 and higher automation levels, the autonomous system continuously monitors the environment using sensors, cameras, radars, and a global positioning system (GPS) feeding information to the control software. A typical autonomous system in a vehicle acquires information, analyzes the information, and then implements the optimal action/decision. Specifically, in level 3 automation the vehicle can autonomously drive for the most part; however, drivers are encouraged to monitor the driving environment at all times and are expected to take over the control when requested by the autonomous system in certain situations. In level 4 automation, the autonomous driving system is able to perform all driving tasks under certain conditions and the driver has the option to control the vehicle. In level 5 automation, the autonomous driving system is able to perform all driving tasks in all conditions.

It is often argued that fully autonomous vehicles (level 5) will be able to outperform human drivers and hence relying on autonomous driving technology will improve safety; however, many experts argue that there is still a long way ahead. First, for the foreseeable future, the presence of human drivers will be required in all autonomous vehicles due to technology limitations and certain legislative factors (Goodrich and Boer, 2000; Parasuraman and Manzey, 2010; Kyriakidis et al., 2015). In addition, autonomous vehicles consist of highly complex electronic systems interacting with hardware and the environment making them vulnerable to certain threats that may pose risk to people in the vehicle as well as pedestrians and other road users (Petit and Shladover, 2015). As evident by the recent crash records for vehicles with varying degrees of autonomy, one major threat is extreme road and immediate environmental conditions which may affect the integrity and reliability of autonomous technologies. Road and environmental factors such as bright light, heavy rain, snow, or fog and poor road and traffic signs quality may affect the ability of autonomous systems to function properly (Tesla, 2017). For instance, in 2016, a fatal accident occurred when a level 2 autonomous vehicle was in control and collided with a tractor-trailer that was making a turn. The autonomous system sensors failed to recognize the difference between the truck and bright sky, causing the collision. In 2017, another vehicle with autonomous capabilities crashed into a road construction barrier after it failed to recognize the roadway and merge into another lane (Lambert, 2017). This occurred as a result of various factors including poorly implemented road construction and failure in the ability of the autonomous system to recognize the upcoming wall.

Overall, implementing intermediate levels of automation, i.e., levels 2 through 4, is seen as the next phase in the mass adoption of autonomous driving technologies. Indeed, over the past decade, there has been a rapid increase in the development of vehicles equipped with advanced driver assistance systems. Vehicle manufacturers such as Tesla, Toyota, BMW, Nissan, Audi, General Motors, and Volvo have equipped vehicles with autonomous technologies such as autonomous emergency braking (AEB), adaptive cruise control (ACC), lane keeping assist (LKA), and automatic parking constituting various levels of autonomy as specified by the SAE (SAE, 2014; Lu and de Winter, 2015). Manufacturers like Audi and Tesla already have implemented level 3 automation in recently released models. In levels 2 through 4, it is envisioned that the human driver has the option to take over the control of vehicle. Therefore, if high risk circumstances are anticipated, there is a possibility to pass the control to the human driver in a timely manner to reduce the overall safety risk.

Switching control back and forth between the human driver and the autonomous driving entity to maximize safety may not be straightforward as every such switch can itself pose a short-term, elevated risk. With intermediate levels of automation, drivers are expected to engage in various activities (e.g., smartphone and tablet use) while the autonomous system is in control, but will be required to take control of the vehicle at certain times or based on feedback from the system. Hence, one of the factors that makes the transition of control between the two driving entities challenging is the potentially long transition time for transferring the control from the autonomous system to the driver due to a phenomenon known as the 'out-of-the-loop' (OOTL) problem, caused by the disengagement of the driver from the environment.

After being disengaged from the driving environment during the period where the autonomous system is in control, drivers are naturally expected to have higher reaction times (RT). Even in levels 0-2 autonomy, drivers need time to recognize the occurrence of an out-of-the-ordinary event, decide on an appropriate action, and act upon this decision. Research shows that RT can vary widely, ranging from 0.7 seconds when an event is expected, to 1.5 seconds when it is not (e.g., sudden braking from the lead vehicle) (Green, 2000). Even when drivers have full control of the car during the entire trip, their "expectation" can affect reaction times by as much as a factor of 2 (Green, 2000). With the promise of freedom from constant engagement with the driving environment, level 3 autonomy can have more dramatic affects on driver reaction times, increasing the time it takes to regain the driver's attention to 3 to 7 seconds, even with visual and verbal warnings, according to a study by Audi (Davies, 2015).

To that end, OOTL problems arise when the driver has to re-take control of the vehicle from the automated system after engagement with secondary tasks over a period of time. De Winter et al. (2014) showed that the workload of drivers and situation awareness are vastly different for driving with assisted autonomy, i.e., levels 1 and 2 autonomy, compared to highly automated driving (HAD), i.e., level 3 and higher autonomy. More specifically, mental workload and situation awareness generally decrease with increasing levels of automation and the brake reaction time of drivers increase for automated systems compared to manual driving (Young and Stanton, 2007; Kaber and Endsley, 2004; Merat et al., 2014b). Other studies have investigated the effect of the transition of control authority on the way drivers reclaim control of the vehicle, also known as ‘take-over quality’ (Miller et al., 2015; Merat et al., 2014a; Strand et al., 2014; Koo et al., 2016). In general, these studies conclude that for higher levels of autonomy drivers need more time to re-obtain full control over the vehicle. In addition, for short warning times it was found that the take-over quality drastically decreases, therefore illustrating that accidents and near-accidents are likely to occur when the driver resumes control. In poor quality take-overs, it was found that the transition process may result in situations where drivers accidentally swerve, brake harshly, or perform sudden lane changes (Eriksson and Stanton, 2017). Automation may therefore often reduce the workload during non-dangerous driving conditions, but sudden control changes may be detrimental to driving safety (Rudin-Brown and Parker, 2004; Koo et al., 2016).

Therefore, it is necessary to balance the short-term risks of switching entity and the long-term risks of continuing with the entity in charge, given the dynamic changes of road/environment. In this study, we develop a mathematical framework to optimally plan a trip by dynamically switching the control between the human driver and self-driving technology to provide the safest driving profile. Specifically, first we develop a Markov decision process (MDP) model to prescribe the driving entity in charge and the timing of transfers as a function of the road condition and environmental changes. The objective is to determine the optimal driving-entity switching policy to minimize the total expected discounted cost of possible accidents, considering the dynamic changes of the road/environment during the trip. This model is relatively compact and provides an opportunity to easily investigate the impact of switching driving entities and draw insights about the risks involved.

However, note that in this MDP model, we assume the road/environment condition is completely observable, i.e., both driving entities can accurately assess the road/environment condition during the trip and determine its exact safety risk level. Clearly, this implies that the vehicle is equipped with an algorithm that can accurately evaluate the road/environment condition and determine its exact safety risk level. Given the advances in machine learning and image processing, this may soon become a reality. However, most existing algorithms, as well as human drivers, are not always one hundred percent accurate in their evaluations. Hence, we also relax this assumption and develop a partially observable Markov decision process (POMDP) model, in which the risk posed by the road/environment condition is only ‘partially’ observed and is prone to erroneous estimations.

The chapter is organized as follows. We formulate the model under complete and partial information in Section 2.2. In Section 2.3, we provide extensive computational studies to illustrate the benefits of switching control authority and investigate the model sensitivity and robustness with respect to those model parameters that are most difficult to calibrate. Lastly, we conclude in Section 2.4 and provide insights.

2.2 Model Formulation

In this section, we formulate models under different conditions to determine the optimal driving entity. First, we assume the model has complete information regarding the state of the system in which case we formulate a Markov decision process (MDP). That is, we assume the model has perfect information regarding the location, environment, and driving entity in charge. Next, we assume partial information regarding the state of the environment where it is assumed that the environmental risk is obtained through a separate algorithm. In this case, we formulate the system as a partially observable Markov decision process (POMDP).

2.2.1 Under Full Information

In this section, we develop an MDP model to optimally plan a trip by dynamically switching the control between the human driver and the autonomous driving entity to minimize the total expected cost of accidents throughout a trip. In this study, three types of consequences for a motor vehicle crash are considered, namely, vehicle damage, bodily injury, and fatality, to each of which a cost is assigned. Every time period (e.g., every second), a decision is made as to whether the human driver or the car needs to take control of the vehicle. It is assumed that the car can immediately take over the vehicle control from the human driver once a decision for this switch is made. However, dependent on the driver’s reaction time, it may take up to a few seconds for the human driver to take over the vehicle control if such a decision is made.

Let $\boldsymbol{s_t} = (\boldsymbol{\mu}, \phi, d) \in S$ denote the state of the process at time $t \leq T$, where $T < \infty$ denotes the length of the time horizon. Let the vector $\boldsymbol{\mu} = [\boldsymbol{\ell}, \boldsymbol{\xi}]$ denote the location-environment vector. Specifically, the vector $\boldsymbol{\ell} \in L$ denotes the location of the vehicle, where the set L includes the location of the origin and destination, denoted by $\boldsymbol{\ell_O}$ and $\boldsymbol{\ell_D}$, respectively, and all other locations in the path between the origin and the destination. In addition, the vector $\boldsymbol{\xi} \in \Xi$ denotes the state of the road/environment, e.g., weather, number of pedestrians, quality of the road segment, etc. Furthermore, we let $\phi \in \{I, C\}$ denote the entity in charge of driving the vehicle, where I refers to the 'individual' and C refers to the 'car.' Lastly, we let d denote the time to the next scheduled switch in the driving entity from the car to the individual, if it is previously scheduled, and assign to it the value -1, otherwise.

We discretize time into periods, e.g., seconds. At the beginning of every time period, a decision is made as to whether the human driver or the car needs to take control of the vehicle. Let $a \in A = \{I, C\}$ denote the action taken in each decision epoch. Recall that although the car can immediately take over the vehicle control from the individual, dependent on the individual's reaction time, it may take up to a few seconds for the individual to take over the vehicle control. Let $k > 0$ denote the length of time it takes for the driver to take over the vehicle control from the car once a decision is made to switch the control. Also, we let c_A denote the cost of alerting the individual to take over the control, and c_P denote the penalty of foregoing a previously made decision to hand over the control to the individual before it is implemented. These costs penalize unnecessary alerts that may cause alarm fatigue in the long run.

Let $p_\phi(\boldsymbol{\mu})$ denote the probability of accident for the driving entity ϕ at location-environment $\boldsymbol{\mu}$, and let $q_0(\phi, \boldsymbol{\mu})$, $q_1(\phi, \boldsymbol{\mu})$, and $q_2(\phi, \boldsymbol{\mu})$ denote the conditional probability of damage, injury and fatality, given an accident occurs for driving entity ϕ at location-environment $\boldsymbol{\mu}$, respectively. Similarly, let $\zeta_\phi(\boldsymbol{\mu})$ denote the probability of accident at location-environment $\boldsymbol{\mu}$ as a result of a switch of the vehicle control to entity ϕ, and let $\rho_0(\boldsymbol{\mu})$, $\rho_1(\boldsymbol{\mu})$, and $\rho_2(\boldsymbol{\mu})$ denote the conditional probability of damage, injury and fatality, given an accident occurs at location-environment $\boldsymbol{\mu}$ following the switch in driving entity, respectively.

Let c_0, c_1, and c_2 denote the cost of damage, injury and fatality of an accident, respectively. Consequently, let $\beta(\phi, \boldsymbol{\mu})$ denote the expected immediate cost of accident for driving entity ϕ at location-environment $\boldsymbol{\mu}$, given an accident occurs for this entity. Also, let $\gamma(\phi, \boldsymbol{\mu})$ denote the expected immediate cost of an accident after switching the vehicle control to entity ϕ at location-environment $\boldsymbol{\mu}$. These costs are given by

$$\beta(\phi, \boldsymbol{\mu}) = \sum_{i=0}^{2} q_i(\phi, \boldsymbol{\mu}) c_i \quad \text{and} \quad \gamma(\phi, \boldsymbol{\mu}) = \sum_{i=0}^{2} \rho_i(\boldsymbol{\mu}) c_i. \tag{2.1}$$

Let $p(\boldsymbol{\xi'}|\boldsymbol{\xi})$ denote the probability that the road/environment state transitions from vector $\boldsymbol{\xi}$ to $\boldsymbol{\xi'}$. In addition, it is assumed that the location of the vehicle along the path from the origin to the destination is fully observed through the GPS system at every time period. Let $\boldsymbol{\ell'}$ denote the location of the vehicle at the end of a time period. Let α denote the discount factor.

Finally, let $V_t^*([\boldsymbol{\ell}, \boldsymbol{\xi}], \phi, d)$ denote the minimum expected discounted cost-to-go starting at time t with the driving entity ϕ at location $\boldsymbol{\ell}$ under the road/environment state $\boldsymbol{\xi}$, when the next switch to individual is scheduled in d time periods. The problem terminates when $t = T$ or $\boldsymbol{\ell} = \boldsymbol{\ell_D}$, i.e.,

$$V_T^*([\boldsymbol{\ell}, \boldsymbol{\xi}], \phi, d) = 0 \ \forall \boldsymbol{\ell}, \boldsymbol{\xi}, \phi, d \text{ and } V_t^*([\boldsymbol{\ell_D}, \boldsymbol{\xi}], \phi, d) = 0 \ \forall t, \boldsymbol{\xi}, \phi, d. \tag{2.2}$$

For $t < T$ and $\boldsymbol{\ell} \neq \boldsymbol{\ell_D}$, when $\phi = I$, the minimum expected discounted cost starting from the location-environment vector $\boldsymbol{\mu}$ is given by

$$V_t^*(\boldsymbol{\mu}, I, -1) = \min_{a \in A} \tag{2.3}$$
$$\begin{cases} p_I(\boldsymbol{\mu}) \cdot \beta(I, \boldsymbol{\mu}) + (1 - p_I(\boldsymbol{\mu})) \cdot \sum_{\boldsymbol{\xi'} \in \Xi} p(\boldsymbol{\xi'}|\boldsymbol{\xi}) \cdot \alpha \cdot V_{t+1}^*([\boldsymbol{\ell'}, \boldsymbol{\xi'}], I, -1), \\ \zeta_C(\boldsymbol{\mu}) \cdot \gamma(C, \boldsymbol{\mu}) + (1 - \zeta_C(\boldsymbol{\mu})) \cdot \Big[p_C(\boldsymbol{\mu}) \cdot \beta(C, \boldsymbol{\mu}) + (1 - p_C(\boldsymbol{\mu})) \cdot \sum_{\boldsymbol{\xi'} \in \Xi} p(\boldsymbol{\xi'}|\boldsymbol{\xi}) \cdot \alpha \cdot V_{t+1}^*([\boldsymbol{\ell'}, \boldsymbol{\xi'}], C, -1) \Big]. \end{cases}$$

Starting from state $s_t = (\boldsymbol{\mu}, I, -1)$, the first expression in equation (2.3) gives the total expected discounted cost when the decision is to allow the individual to continue driving, i.e., $a = I$. In this case, if an accident occurs with the individual in control, a lump-sum cost incurs and the problem terminates. Otherwise, the process continues starting from the next period, with an updated location and a new road/environment state where the individual is driving and no switches are scheduled. Starting from state $s_t = (\boldsymbol{\mu}, I, -1)$, the second expression in equation (2.3) gives the total expected discounted cost when the decision is to hand over the control to the car, i.e., $a = C$. In this case, the car can immediately take over the control of the vehicle; however, such a switch can pose an instantaneous, elevated risk of accident. If an accident occurs as a result of the switch, a lump-sum cost incurs and the problem terminates. If the switch does not result in an accident, an accident can still occur with the new entity, i.e., the car, in charge. If such an accident occurs, again a lump-sum cost incurs and the problem terminates. Finally, if no accident occurs in this period, the process continues starting from the next period, with an updated location and a new road/environment state where the car is driving and no switches are scheduled.

For $t < T$ and $\boldsymbol{\ell} \neq \boldsymbol{\ell_D}$, when $\phi = C$ and $d = -1$, the minimum expected discounted cost starting from the location-environment vector $\boldsymbol{\mu}$ is given by

$$V_t^*(\boldsymbol{\mu}, C, -1) = \min_{a \in A} \tag{2.4}$$

$$\begin{cases} c_A + p_C(\boldsymbol{\mu}) \cdot \beta(C, \boldsymbol{\mu}) + (1 - p_C(\boldsymbol{\mu})) \cdot \sum_{\boldsymbol{\xi'} \in \Xi} p(\boldsymbol{\xi'}|\boldsymbol{\xi}) \cdot \alpha \cdot V_{t+1}^*([\boldsymbol{\ell'}, \boldsymbol{\xi'}], C, k-1), \\ p_C(\boldsymbol{\mu}) \cdot \beta(C, \boldsymbol{\mu}) + (1 - p_C(\boldsymbol{\mu})) \cdot \sum_{\boldsymbol{\xi'} \in \Xi} p(\boldsymbol{\xi'}|\boldsymbol{\xi}) \cdot \alpha \cdot V_{t+1}^*([\boldsymbol{\ell'}, \boldsymbol{\xi'}], C, -1). \end{cases}$$

Equation (2.4) is similar in structure to equation (2.3). Starting from state $s_t = (\boldsymbol{\mu}, C, -1)$, the first expression in equation (2.4) gives the total expected discounted cost when the decision is to hand over the control to the individual, i.e., $a = I$. In this case, the individual is immediately alerted about the decision at the immediate cost of c_A; however, the individual would not take over the control until k periods later. Meanwhile, the car remains in charge. If an accident occurs while the car is in charge, a lump-sum cost incurs and the problem terminates. Otherwise, the process continues starting from the next period, with an updated location and a new road/environment state where the car is still in charge but a switch is scheduled for $k - 1$ periods later. Starting from state $s_t = (\boldsymbol{\mu}, C, -1)$, the second expression in equation (2.4) gives the total expected discounted cost when the decision is to allow the car to continue driving, i.e., $a = C$. This expression is similar to the first expression in equation (2.3), with the exception of setting ϕ to be C instead of I throughout.

For $t < T$ and $\boldsymbol{\ell} \neq \boldsymbol{\ell_D}$, when $\phi = C$ and $d > 0$, the minimum expected discounted cost starting from the location-environment vector $\boldsymbol{\mu}$ is given by

$$V_t^*(\boldsymbol{\mu}, C, d) = \min_{a \in A} \tag{2.5}$$
$$\begin{cases} p_C(\boldsymbol{\mu}) \cdot \beta(C, \boldsymbol{\mu}) + (1 - p_C(\boldsymbol{\mu})) \cdot \sum_{\boldsymbol{\xi'} \in \Xi} p(\boldsymbol{\xi'}|\boldsymbol{\xi}) \cdot \alpha \cdot V_{t+1}^*([\boldsymbol{\ell'}, \boldsymbol{\xi'}], C, d-1), \\ c_P + p_C(\boldsymbol{\mu}) \cdot \beta(C, \boldsymbol{\mu}) + (1 - p_C(\boldsymbol{\mu})) \cdot \sum_{\boldsymbol{\xi'} \in \Xi} p(\boldsymbol{\xi'}|\boldsymbol{\xi}) \cdot \alpha \cdot V_{t+1}^*([\boldsymbol{\ell'}, \boldsymbol{\xi'}], C, -1). \end{cases}$$

Analogous to equations (2.3) and (2.4), the first and second expressions in equation (2.5) give the total expected discounted cost starting from state $s_t = (\boldsymbol{\mu}, C, d)$ for $a = I$ and $a = C$, respectively. If $a = I$, because a switch in control is previously scheduled, the car continues driving until the end of the period, at which point the remaining time to the scheduled switch is decreased by 1 unit to $d-1$. If $a = C$, it overrides the previously scheduled switch, an immediate penalty incurs and the vehicle remains the entity in charge with no switches scheduled.

Finally, for $t < T$ and $\boldsymbol{\ell} \neq \boldsymbol{\ell_D}$, when $\phi = C$ and $d = 0$, the minimum expected discounted cost starting from the location-environment vector $\boldsymbol{\mu}$ is given by

$$V_t^*(\boldsymbol{\mu}, C, 0) = \min_{a \in A} \tag{2.6}$$
$$\begin{cases} \zeta_I(\boldsymbol{\mu}) \cdot \gamma(I, \boldsymbol{\mu}) + (1 - \zeta_I(\boldsymbol{\mu})) \cdot \Big[p_I(\boldsymbol{\mu}) \cdot \beta(I, \boldsymbol{\mu}) + \\ \quad (1 - p_I(\boldsymbol{\mu})) \cdot \sum_{\boldsymbol{\xi'} \in \Xi} p(\boldsymbol{\xi'}|\boldsymbol{\xi}) \cdot \alpha \cdot V_{t+1}^*([\boldsymbol{\ell'}, \boldsymbol{\xi'}], I, -1) \Big], \\ c_P + p_C(\boldsymbol{\mu}) \cdot \beta(C, \boldsymbol{\mu}) + (1 - p_C(\boldsymbol{\mu})) \cdot \sum_{\boldsymbol{\xi'} \in \Xi} p(\boldsymbol{\xi'}|\boldsymbol{\xi}) \cdot \alpha \cdot V_{t+1}^*([\boldsymbol{\ell'}, \boldsymbol{\xi'}], C, -1). \end{cases}$$

Analogous to equations (2.3)-(2.5), the first and second expressions in equation (2.6) give the total expected discounted cost starting from state $s_t = (\boldsymbol{\mu}, C, 0)$ for $a = I$ and $a = C$, respectively. If $a = I$, because $d = 0$, the driving entity immediately switches to the individual, due to which an accident can occur. In this case, if an accident occurs either as a result of the switch or after the individual takes complete control, a lump-sum cost incurs and the problem terminates. Otherwise, the process continues starting from the next period with the individual in charge, where no switches are scheduled. If $a = C$, it overrides the previously scheduled switch and the same expression as the second expression in equation (2.5) follows.

2.2.2 Under Partial Information

In this section, we assume that the state of the environment, $\boldsymbol{\xi}$, is only partially observed. That is, we assume the vehicle is equipped with an algorithm, e.g., a sequential image classification algorithm, that can estimate the degree of risk in the environment. Clearly, such an algorithm is subject to error and does not necessarily have 100% sensitivity or specificity. Hence, we assume the information only partially informs the authority switching decision making process.

We assume the set Ξ is countable, and let $\boldsymbol{\pi_t} = [\pi_t^{\xi}(\boldsymbol{\xi_1}), \pi_t^{\xi}(\boldsymbol{\xi_2}), \ldots, \pi_t^{\xi}(\boldsymbol{\xi_{|\Xi|}})]$ denote the belief state of the environment, where $\pi_t^{\xi}(\boldsymbol{\xi_j}) \geq 0$ is the probability that the vehicle is in road/environment state $\boldsymbol{\xi_j} \in \Xi$ at time t and $\sum_{j=1}^{|\Xi|} \pi_t^{\xi}(\boldsymbol{\xi_j}) = 1$. At every time epoch, the algorithm is used to observe the state of the environment, where the observation is later incorporated to update the belief vector. Let $\boldsymbol{o_t^{\xi}}$ denote the observation made about the state of the environment at time t.

Let $\boldsymbol{z_t} = (\boldsymbol{\ell}, \boldsymbol{\pi}, \phi, d)$ denote the state of the process, including the fully known information and partially informed state of the environment, at time $t \leq T$, where $T < \infty$ denotes the length of the time horizon. Let $W_t^*(\boldsymbol{\ell}, \boldsymbol{\pi}, \phi, d)$ denote the minimum expected discounted cost-to-go starting at time t, the driving entity ϕ in charge, at location $\boldsymbol{\ell}$ under the environment belief vector $\boldsymbol{\pi}$, when the next switch to individual is scheduled in d time periods. Similar to Section 2.2.1, the problem terminates when $t = T$ or $\boldsymbol{\ell} = \boldsymbol{\ell_D}$, i.e.,

$$W_T^*(\boldsymbol{\ell}, \boldsymbol{\pi}, \phi, d) = 0 \;\; \forall \boldsymbol{\ell}, \boldsymbol{\pi}, \phi, d \;\text{ and }\; W_t^*(\boldsymbol{\ell_D}, \boldsymbol{\pi}, \phi, d) = 0 \;\; \forall t, \boldsymbol{\pi}, \phi, d. \tag{2.7}$$

For $t < T$ and $\boldsymbol{\ell} \neq \boldsymbol{\ell_D}$, when $\phi = I$, the minimum expected discounted cost starting from any location $\boldsymbol{\ell}$ and environment belief vector $\boldsymbol{\pi}$ is given by

$$W_t^*(\boldsymbol{\ell}, \boldsymbol{\pi}, I, -1) = \min_{a \in A} \tag{2.8}$$

$$\begin{cases} \sum_{\boldsymbol{\xi} \in \Xi} \pi_t^{\xi}(\boldsymbol{\xi}) \cdot p_I(\boldsymbol{\mu}) \cdot \beta(I, \boldsymbol{\mu}) + \\ \quad \sum_{\boldsymbol{\xi} \in \Xi} \pi_t^{\xi}(\boldsymbol{\xi}) \cdot (1 - p_I(\boldsymbol{\mu})) \cdot \sum_{\boldsymbol{\xi'} \in \Xi} \sum_{\boldsymbol{o_{t+1}^{\xi}} \in \Xi} p(\boldsymbol{\xi'}|\boldsymbol{\xi}) p(\boldsymbol{o_{t+1}^{\xi}}|\boldsymbol{\xi'}) \cdot \alpha \cdot W_{t+1}^*(\boldsymbol{\ell'}, \boldsymbol{\pi'}, I, -1), \\ \sum_{\boldsymbol{\xi} \in \Xi} \pi_t^{\xi}(\boldsymbol{\xi}) \cdot \Big[\zeta_C(\boldsymbol{\mu}) \cdot \gamma(C, \boldsymbol{\mu}) + (1 - \zeta_C(\boldsymbol{\mu})) \cdot p_C(\boldsymbol{\mu}) \cdot \beta(C, \boldsymbol{\mu}) \Big] + \sum_{\boldsymbol{\xi} \in \Xi} \pi_t^{\xi}(\boldsymbol{\xi}) \cdot \\ \quad (1 - \zeta_C(\boldsymbol{\mu})) \cdot (1 - p_C(\boldsymbol{\mu})) \cdot \sum_{\boldsymbol{\xi'} \in \Xi} \sum_{\boldsymbol{o_{t+1}^{\xi}} \in \Xi} p(\boldsymbol{\xi'}|\boldsymbol{\xi}) \cdot p(\boldsymbol{o_{t+1}^{\xi}}|\boldsymbol{\xi'}) \cdot \alpha \cdot W_{t+1}^*(\boldsymbol{\ell'}, \boldsymbol{\pi'}, C, -1), \end{cases}$$

where $\boldsymbol{\pi'} = [\pi_{t+1}^{\xi}(\boldsymbol{\xi_1}), \pi_{t+1}^{\xi}(\boldsymbol{\xi_2}), \ldots, \pi_{t+1}^{\xi}(\boldsymbol{\xi_{|\Xi|}})]$ and

$$\pi_{t+1}^{\xi}(\boldsymbol{\xi_i}) = \frac{p(\boldsymbol{o_{t+1}^{\xi}}|\boldsymbol{\xi_i}) \sum_{\boldsymbol{\xi_j} \in \Xi} p(\boldsymbol{\xi_i}|\boldsymbol{\xi_j}) \pi_t^{\xi}(\boldsymbol{\xi_j})}{\sum_{\boldsymbol{\xi_i} \in \Xi} p(\boldsymbol{o_{t+1}^{\xi}}|\boldsymbol{\xi_i}) \sum_{\boldsymbol{\xi_j} \in \Xi} p(\boldsymbol{\xi_i}|\boldsymbol{\xi_j}) \pi_t^{\xi}(\boldsymbol{\xi_j})} \quad \forall \boldsymbol{\xi_i} \in \Xi. \tag{2.9}$$

Equation (2.8) is analogous to equation (2.3) in Section 2.2.1, where the first and second expressions in the equation give the total expected discounted cost when the decisions are to allow the individual to continue driving, i.e., $a = I$, and to hand over the control to the car, i.e., $a = C$, respectively. Similarly, analogous to equations (2.4), (2.5), and (2.6) in Section 2.2.1, Bellman equations can be written for $t < T$ and $\boldsymbol{\ell} \neq \boldsymbol{\ell_D}$, when $\phi = C$ and $d = -1$, $d > 0$, and $d = 0$, respectively.

To solve the developed POMDP model, we use the asynchronous advantage actor critic (A3C) algorithm (Mnih et al., 2016). In summary, the A3C algorithm is a deep reinforcement learning (DRL) algorithm where a global control network employs multiple agents (each having their own set of network parameters) interacting with an environment to maximize the total expected discounted rewards resulting from their actions. At the start of each training epoch, the agents reset their network parameters to that of the global network. The agents then interact with the environment, calculating the value loss and policy loss in the process. Each agent then gets new learning gradients from these losses, after which the global network is updated asynchronously with these gradients. In the A3C algorithm, being an *actor-critic* method, a critic learns the value function while the actor interacts with the environment attempting to learn a policy to maximize/minimize a given objective function. The global network is updated *asynchronously* to learn more efficiently and to reduce correlation between training episodes. This leads to an overall more diverse set of training samples where the learning experience of each agent is independent. The A3C algorithm uses *advantage*, as opposed to Q-values used by numerous other DRL methods (e.g., see Van Hasselt et al. (2016); Gu et al. (2016)). The benefit of using advantage rather than discounted rewards is that the agent can determine how much better certain actions are for a particular system state.

2.3 Computational Study

In this section, we present various numerical experiments under both full- and partial information regarding the environment. Under full/complete information, we assume the model has perfect information regarding the state of the system in which the MDP model is utilized. Under partial information, we assume the environmental risk is obtained through a separate algorithm (such as a convolutional neural network) and is therefore only partially observable to the system in which case we use the POMDP model.

2.3.1 Computational Study Under Full Information

In this section we first present an illustrative example, for which we find an optimal policy and examine the impact of its implementation during an example trip. We then introduce a number of additional metrics to quantify the risks associated with different driving entity switching policies. Finally, we perform extensive sensitivity and robustness analyses to investigate the effect of model parameters on the total expected discounted cost and risk under the optimal and benchmark policies. The models are calibrated using simulated data. For detailed information on model calibration refer to Appendix B.

In our computational study, to facilitate the presentation of the results, without loss of generality, we use a one-dimensional map where we set the vehicle to advance a unit of distance per time period. This also eliminates the need to include both t and $\boldsymbol{\ell}$ in the model. Consequently, we simplify the state definition to $s = ([\ell, \boldsymbol{\xi}], \phi, d)$, where the process transitions from s to $s' = ([\ell + 1, \boldsymbol{\xi}'], \phi', d')$ in every time period and it terminates when

$\ell = \ell_D$. In addition, for simplicity, in our computational study the road/environment vector, $\boldsymbol{\xi}$, is summarized into three 'risk levels,' namely, $\xi = 0, 1, 2$, corresponding to low, average, and high risk, respectively. To obtain the optimal policy, i.e., the cost-minimizing driving entity switching policy, the backward induction algorithm is executed (see Puterman (1994), page 92).

To put the total expected discounted cost under the optimal policy in perspective, two benchmark policies are used throughout the computational study, corresponding to cases when only the car or the individual can drive throughout the entire path from the origin to the destination. We let π^* denote the optimal policy, and π^C and π^I denote the policies where only the car or the individual can drive, respectively. In addition, we let $V^\chi(s)$ denote the total expected discounted cost obtained starting from state s under policy $\pi^\chi \in \{\pi^*, \pi^C, \pi^I\}$.

An Illustrative Example

In this section, we present an example optimal policy and the impact of its implementation during an example trip. We then compare the total expected discounted cost under the optimal and benchmark policies.

In this example, a destination on the line segment [0,500] is randomly generated and then links are randomly selected on the path from the origin at location 0 to the destination. The path and its junction points are as follows: [0, 18, 90, 144, 202, 231, 253], with the following link lengths from the origin to the destination: [18, 72, 54, 58, 29, 22]. This path may be interpreted as follows: Starting from the origin, i.e., location 0, the vehicle first needs to traverse a link of length 18 units to reach location 18. From this location, the vehicle needs to travel through a link of length 72 units to reach location 90, etc. Finally, the vehicle reaches the destination at location 253. Note that the definition of a link in this context is different from the typical link definition in transportation networks. A link here is defined as a path that is distinct from its connecting links in at least one of the following criteria: Speed limit, road curvature, road quality, etc. For more details on parameter values, see Appendix B.

In general, in this illustrative example, the car is considered to be a safer driving entity than the individual, and the probabilities $p_\phi(\boldsymbol{\mu})$ and $\zeta_\phi(\boldsymbol{\mu})$ are generated to reflect this

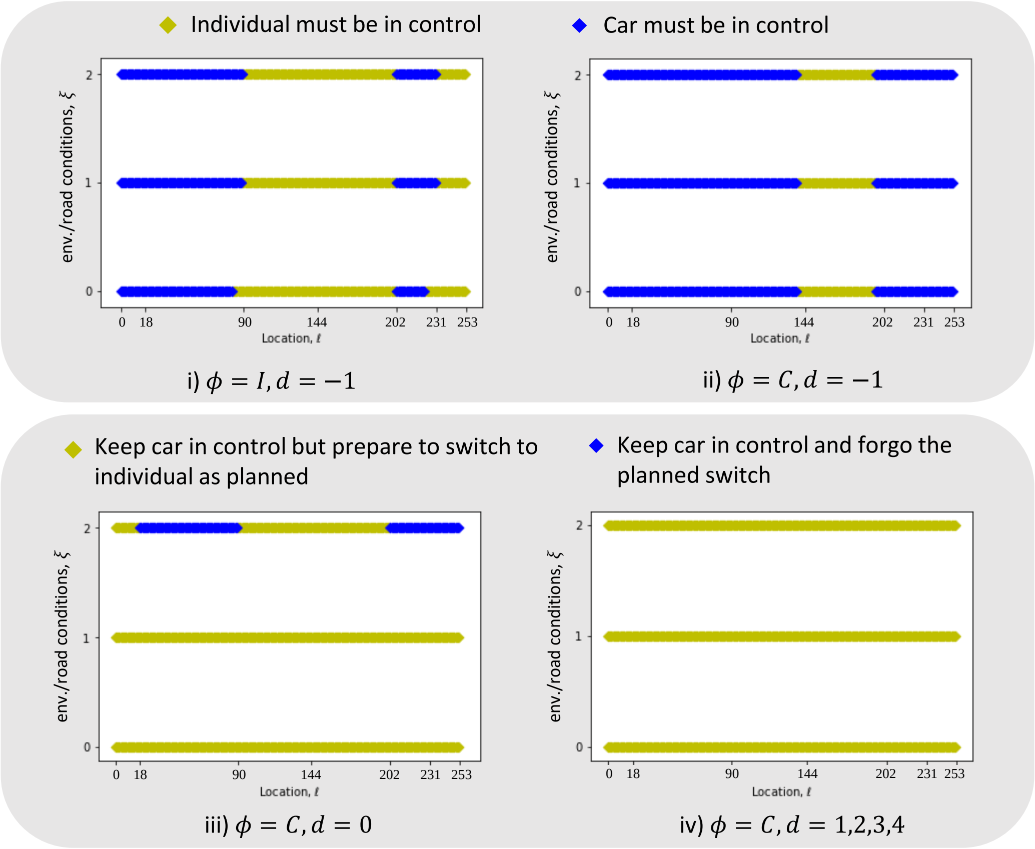

i) $\phi = I, d = -1$

ii) $\phi = C, d = -1$

iii) $\phi = C, d = 0$

iv) $\phi = C, d = 1,2,3,4$

Figure 2.1: An example MDP-generated optimal authority switching policy.

assumption. On the fourth link, however, the probability distributions are changed so as to create a situation in which an individual driver would be the safer choice to possibly trigger a change in driving entity. In addition, the probability $p_C(\boldsymbol{\mu})$ is increased by 50 and 100 folds for average and high risk conditions, respectively, on this specific link. In real-world conditions, this increase in risk of accident for the automated driving entity may be related to a road section in which lane changes are poorly implemented due to construction activities. It has been shown that such circumstances can cause major uncertainty in the autonomous system's decision-making capabilities (Lambert, 2017). For more details on the probability distributions, refer to Appendix B.

Figure 2.1 presents the optimal MDP-generated authority switching policy for the calibrated model. The optimal driving entity switching policy prescribes the optimal action for every state of the system. Specifically, Figures 2.1(i)-(ii) present the optimal policy plots when the individual (I) and the car (C) are in control, respectively, and no switch is scheduled, i.e., $d = -1$. Figures 2.1(iii)-(iv) present the optimal policy plots when the car is in control, but a switch is scheduled in d seconds. The horizontal axes in the figure display the set of locations alongside the trip, and the vertical axes show the road/environment conditions. At a given location and under a given risk level, a dark-shaded (blue) dot indicates that the optimal policy is for the human driver to be in control, while a light-shaded (gold) dot indicates that it is optimal for the autonomous entity to be in control.

It is interesting to observe and interpret optimal control policies to find structures that would be present regardless of parameter values. Similar to the example policy plots in Figure 2.1, in our numerical experiments, we consistently observe that the plots are identical for all $d \in \{1, \ldots, k-1\}$. This is because when the car is in control, but a non-imminent switch to the individual is scheduled ($\phi = C$ and $d > 0$), the car must retain control for d time epochs, which translates into a distance of d units under a constant speed, while issuing an alert to the individual to minimize the effect of OOTL problems. Hence, foregoing the alert at $d > 0$ does not hold any additional value as there is still an opportunity to forgo the alert until d reaches 0. Therefore, the model prescribes the vehicle to issue an alert as planned and only forgo the alert at the last decision epoch prior to the switch, i.e., when $d = 0$, if needed to assure that the best decision is made considering the dynamic changes of the road/environment.

In addition, we also observe intuitive behavior with respect to changes in total expected discounted cost. For instance, across all our experiments, we observe that the total expected discounted cost $V([\ell, \xi], \phi, d)$ is non-increasing in ℓ for a trip, for any given ξ, ϕ, and d values. This is mainly because the shorter the remaining length of the trip, the smaller the overall likelihood of getting involved in an accident, hence the observed decreasing behavior in total expected discounted cost-to-go starting from any state along the path. Also, we observe that the total expected discounted cost $V([\ell, \xi], \phi, d)$ is non-decreasing in ξ for any given ℓ, ϕ, and d values. This is also consistent with intuition, which suggests that starting from any state, the higher the risk of the road/environment state (as a result of bad weather, traffic congestion, pedestrians in the immediate physical environment, etc.), the higher the total expected discounted cost-to-go, mainly because of the greater likelihood of getting involved in an accident right away due to the higher risk.

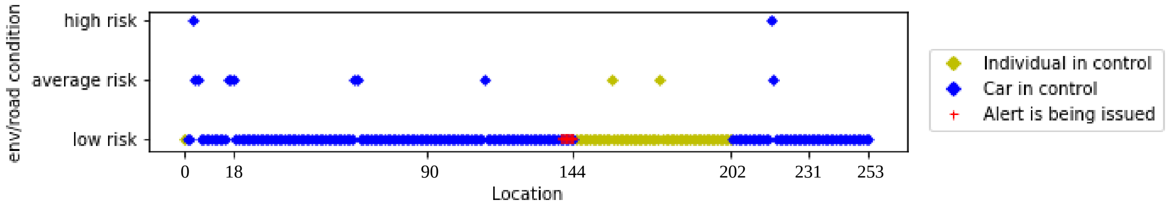

Figure 2.2: A sample path of states under the optimal policy starting from state $s = ([0, 0], I, -1)$.

Figure 2.2 illustrates the optimal actions for a sample path of road/environment condition along this trip, starting from state $s = ([0, 0], I, -1)$. Specifically, the figure depicts the observed state of the road/environment during the trip from the origin to destination, where the shade of the points represent the entity in control as prescribed by the optimal policy, illustrated in Figure 2.1. The light- and dark-shaded points represent the individual and the car are in control, respectively. Lastly, the plus-shaped markers indicate that an alert is being issued for the driver to take over the control from the car, while the car is still in control.

As seen in the figure, the individual is in charge at the origin. However, consistent with the optimal policy in Figure 2.1(i), the control is immediately handed over to the car. Based on the optimal policy in Figure 2.1(ii), the car remains in charge throughout the first three links, namely, (0, 18) and (18, 90), and (90, 144). During this part of the trip the car occasionally faces average and high risk conditions. Finally, consistent with the optimal policy in Figure 2.1(ii), and intuition, starting from location 140, as the vehicle approaches link 4 (in which the individual is the safer control authority), it becomes optimal for the vehicle to prepare for passing the control to the individual. Hence, consistent with the optimal policy in Figures 2.1(iii)-(iv), the car remains in control for the next $k = 5$ seconds while an alert is being issued to the individual to prepare to take over the control. Consequently, the control is passed to the individual. Consistent with the optimal policy in Figure 2.1(i), the individual remains in control during the high risk link (144, 202) until the car takes back the control at location 202. Lastly, consistent with the optimal policy in Figure 2.1(ii), the vehicle continues the trip during the final two links with the car in control, until it reaches the destination at location 253. Note that no accident occurred during this trip as the vehicle started from the origin and reached the destination.

Table 2.1: Comparison of the optimal policy with the two benchmark policies π^I and π^C.

Road/environment condition, ξ	**Starting driving entity, ϕ**	**Total expected discounted cost**		
		Under the optimal policy, V^*	**When only the individual can drive, V^I**	**When only the car can drive, V^C**
Low risk	Individual	462.89	1,623.23	-
	Car	456.29	-	937.81
Average risk	Individual	593.57	1,985.05	-
	Car	579.73	-	1,061.04
High risk	Individual	1,087.46	2,582.09	-
	Car	1,046.90	-	1,527.81

Table 2.1 presents the total expected discounted cost obtained starting from the origin when no switch is scheduled, i.e., $d = -1$, under various initial road/environment conditions, ξ, and entities in charge, ϕ. First note that, as expected, the worse the initial road/environment condition, the higher the total expected discounted cost of the trip under any given policy. More importantly, as seen in the table, the cost under the optimal policy is much lower, compared with that under the two benchmark policies. Note that the cost corresponding to π^I is generally higher than under π^C as the model calibration renders the car as the generally safer option, except in the fourth link (144, 202).

Additional Metrics

In the following, we introduce a number of additional metrics to quantify risks associated with different policies and facilitate their comparison.

Total expected discounted risk of accidents under policy π^χ, $R^\chi(\boldsymbol{\mu}, \phi, d)$. This metric calculates the total expected discounted likelihood of accident during a trip, starting from the state $s = (\boldsymbol{\mu}, \phi, d)$, under a given driving entity switching policy $\pi^\chi \in \{\pi^*, \pi^C, \pi^I\}$. The risks consist of the probability of accident while driving with the entity in charge due to location/environment-related reasons and when switching the driving entity.

To calculate the total expected discounted risk, we first slightly modify the formulations presented in Section 2.2 to allow the model to accumulate risks, instead of costs. Then, we conduct *policy evaluation* where we fix the input policy and use the new formulation to recursively calculate the total expected discounted risk starting from any starting state. We let $a^{\chi}(s)$ denote the action in state s under policy π^{χ}.

First note that we set the risk-to-go equal to 0 when the problem terminates. Hence, analogous to equation (2.2) we have

$$R^{\chi}([\ell_D, \xi], \phi, d) = 0 \ \ \forall \xi, \phi, d. \tag{2.10}$$

Recall that starting from Section 2.3, we set the vehicle to advance a unit of distance per time period, hence the removal of dependency on time. Furthermore, we modify the immediate cost functions to capture immediate risks. That is, we set the cost vector $[c_0, c_1, c_2]$ to an all-ones vector, i.e., $[1, 1, 1]$, in equation (2.1). This results in $\beta(\phi, \boldsymbol{\mu}) = 1$ and $\gamma(\phi, \boldsymbol{\mu}) = 1$, simply capturing risk instead of cost. Hence, for instance, analogous to equation (2.3), the total expected discounted risk under policy π^{χ}, starting from state $s = (\boldsymbol{\mu}, I, -1)$, is given by

$$\begin{aligned} &R^{\chi}(\boldsymbol{\mu}, I, -1) = \qquad\qquad\qquad\qquad\qquad\qquad\qquad\qquad\qquad\qquad\qquad\qquad\qquad (2.11)\\ &\begin{cases} p_I(\boldsymbol{\mu}) + (1 - p_I(\boldsymbol{\mu})) \cdot \sum_{\xi' \in \Xi} p(\xi'|\xi) \cdot \alpha \cdot R^{\chi}([\ell + 1, \xi'], I, -1) & \text{if } a^{\chi}(s) = I, \\ \zeta_C(\boldsymbol{\mu}) + (1 - \zeta_C(\boldsymbol{\mu})) \Big[p_C(\boldsymbol{\mu}) + (1 - p_C(\boldsymbol{\mu})) \cdot \sum_{\xi' \in \Xi} p(\xi'|\xi) \cdot \alpha & \\ \quad \cdot R^{\chi}([\ell + 1, \ \xi'], C, -1) \Big] & \text{if } a^{\chi}(s) = C. \end{cases} \end{aligned}$$

In addition, we set the cost of alerting the individual to take over the control, c_A, and the penalty cost of foregoing a planned switch in authority, c_P, to 0, i.e., $c_A = c_P = 0$. Hence, equations (2.4)-(2.6) may also be re-written to only account for risks.

Total expected discounted risk of accidents due to location/environment-related reasons under policy π^{χ}, $R_e^{\chi}(\boldsymbol{\mu}, \phi, d)$. This metric calculates the total expected discounted likelihood of accident during a trip due to location/environment-related reasons, starting from state $s = (\boldsymbol{\mu}, \phi, d)$, under a given driving entity switching policy $\pi^{\chi} \in \{\pi^*, \pi^C, \pi^I\}$. Similar to the previous metric, we calculate this metric by modifying the formulations presented in Section 2.2. Specifically, to calculate $R_e^{\chi}(s)$, we use the formulations used to calculate $R^{\chi}(s)$ where we also set $\gamma(\phi, \boldsymbol{\mu})$ equal to zero to only account for the location/environment-related risks.

Total expected discounted risk of accidents due to switching driving entities under policy π^χ, $R_s^\chi(\boldsymbol{\mu}, \phi, d)$. Lastly, this metric calculates the total expected discounted likelihood of accidents during a trip due to switching the driving entity, starting from the state $s = (\boldsymbol{\mu}, \phi, d)$, under a given driving entity switching policy $\pi^\chi \in \{\pi^*, \pi^C, \pi^I\}$. Similar to the previous metric, we calculate this metric by modifying the formulations presented in Section 2.2. Specifically, to calculate $R_s^\chi(s)$, we use the formulations used to calculate $R^\chi(s)$ where we also set $\beta(\phi, \boldsymbol{\mu})$ equal to zero to only account for the driving entity switching-related risks.

Note that in this study we overall define two categories of risks, i.e., $R^\chi(s) = R_s^\chi(s) + R_e^\chi(s)$. In addition, note that starting any state s, under policies $\pi^\chi \in \{\pi^C, \pi^I\}$, $R^\chi(s) = R_e^\chi(s)$ and $R_s^\chi(s) = 0$ because these policies are *single* entity driving policies, without any possibilities for switching.

Sensitivity and Robustness Analyses

In this section, we investigate the effect of various model parameters on the results under the optimal and benchmark policies. Specifically, we first investigate the impact of trip length on the results. We then fix the trip length and examine the impact of parameters such as road-environment dynamics and probability of accident by the driving entities. To facilitate these comparisons, we use various performance metrics, including cost and risks, during entire trips by using starting states $s_o = ([0, 0], \phi, -1)$, i.e., starting at location $\ell_O = 0$ under a low risk road/environment state $\xi = 0$, with driving entity ϕ, when no switch in authority is scheduled, $d = -1$. Note that under the benchmark policies π^I and π^C, we use the starting states in which the value of ϕ equals to I and C, respectively. Under the optimal policy π^*, we report the best performance metric obtained starting with either $\phi = I$ or $\phi = C$. Because the models are calibrated with simulated data, we repeat all analyses 25 times to assure that the results are not biased and to also provide a 95% confidence interval (CI) for the reported means.

First, we investigate the impact of trip length on the results, when all else is held constant. To do so, we simulate a trip, consisting of a given number of equal length links, where accident-related probabilities are randomly generated (see Appendix B). We then scale the links to generate three sets of trips with lengths 500, 1000, and 1500 units. As a result, any

Table 2.2: Mean percentage difference in total expected discounted cost, under the optimal and benchmark policies for the 25 sample trips, starting from state s_o. The 95% CI for the means are provided.

Trip length	$\frac{V^C(s_o)-V^*(s_o)}{V^*(s_o)}$	$\frac{V^I(s_o)-V^*(s_o)}{V^*(s_o)}$
500	3.9% ± 3.2%	84.4% ± 28.6%
1000	3.9% ± 3.3%	84.3% ± 29.6%
1500	3.9% ± 3.3%	84.3% ± 29.7%

observed difference in total expected cost under the examined policies would be associated with the differences in trip lengths. We repeat the process 25 times, where we use 5 links per trip, and report the means and the associated CIs under the optimal and benchmark policies. Specifically, Table 2.2 presents the mean percentage difference in total expected discounted cost under the optimal and benchmark policies for these 25 trips, starting from state s_o. In addition, the 95% CI for the means are reported. First, note that the mean percentage difference between the car-only policy and the optimal policy is consistently lower than that between the individual-only policy and the optimal policy. This is mainly because the car is generally considered (and calibrated in the model) to be the safer driving entity. Also, as seen in the table, the mean difference in total expected discounted cost between the optimal and benchmark policies essentially remains the same across all trip lengths. This suggests that the benefits of switching between driving authorities persist regardless of the trip length. Hence, in the remainder of the computational study, we use the fixed length of 1000 for the trips to maintain a low computational time, while allowing for long enough individual links. Specifically, in the remainder of the computational study, we use a sample of 25 randomly generated trips, each with 10 links, and a total trip length of 1000. During each experiment, we only modify one factor at a time and consequently, evaluate the impact of its change on the results.

Next, we investigate the impact of changes in transition probability between road and/or environment states, $p(\xi'|\xi)$. As discussed in Appendix B, we let the matrix $\boldsymbol{P}$ denote the one-step transition probability matrix (TPM) of the road/environment state, where each row presents the conditional probability distribution of the state of the road/environment in

Table 2.3: Mean total expected discounted cost, and mean percentage difference in total expected discounted cost, under the optimal and benchmark policies for the sample 25 trips, starting from state s_o, under $\boldsymbol{P_l}$, $\boldsymbol{P}$, and $\boldsymbol{P_h}$. The 95% CI for the means are provided.

TPM	$V^*(s_o)$	$V^C(s_o)$	$V^I(s_o)$	$\frac{V^C(s_o)-V^*(s_o)}{V^*(s_o)}$	$\frac{V^I(s_o)-V^*(s_o)}{V^*(s_o)}$
$\boldsymbol{P_l}$	431.7 ± 48.5	449.0 ± 55.0	761.6 ± 63.2	3.5% ± 2.6%	92.5% ± 32.8%
$\boldsymbol{P}$	521.2 ± 52.0	536.0 ± 50.4	894.4 ± 82.3	3.1% ± 2.4%	80.3% ± 26.7%
$\boldsymbol{P_h}$	1499.3 ± 73.3	1525.8 ± 106.7	2469.7 ± 174.6	1.7% ± 2.2%	70.0% ± 19.0%

the next time period, i.e.,

$$\boldsymbol{P} = \begin{bmatrix} 0.95 & 0.04 & 0.01 \\ 0.6 & 0.35 & 0.05 \\ 0.25 & 0.7 & 0.05 \end{bmatrix}. \tag{2.12}$$

We allow this TPM to represent the baseline/average risk profile and use stochastic ordering to generate low and high risk profiles (Levy, 2015). Specifically, we let $\boldsymbol{P_l}$ and $\boldsymbol{P_h}$ denote the TPM of low and high risk profiles, respectively, where the conditional road/environment random variables are stochastically smaller and larger than those under the baseline/average scenario, respectively, i.e.,

$$\boldsymbol{P_l} = \begin{bmatrix} 0.96 & 0.03 & 0.01 \\ 0.72 & 0.25 & 0.03 \\ 0.35 & 0.6 & 0.05 \end{bmatrix}, \boldsymbol{P_h} = \begin{bmatrix} 0.85 & 0.1 & 0.05 \\ 0.5 & 0.4 & 0.1 \\ 0.15 & 0.75 & 0.1 \end{bmatrix}. \tag{2.13}$$

With reference to real-world situations, a low risk profile may refer to conditions where the weather is conducive to safe driving or when traffic is not congested. In contrast, a high risk profile may refer to conditions where the vehicle is, on average, more likely to transition to high risk conditions and remain there, such as in urban areas where there is higher levels of interaction between vehicles and pedestrians, and numerous factors may influence the performance of sensors required for automated driving.

Table 2.3 presents the mean total expected discounted cost, and the mean percentage difference in total expected discounted cost, under the optimal and benchmark policies for the 25 sample trips, starting from state s_o, under $\boldsymbol{P_l}$, $\boldsymbol{P}$, and $\boldsymbol{P_h}$. In addition, the 95%

Table 2.4: Mean percentage difference, and the corresponding 95% CI, in total expected discounted risk of accident associated with the optimal and benchmark policies of the sample 25 trips, starting from state s_o, under $\boldsymbol{P_l}$, $\boldsymbol{P}$, and $\boldsymbol{P_h}$.

TPM	$\frac{R^C(s_o)-R^*(s_o)}{R^*(s_o)}$	$\frac{R^I(s_o)-R^*(s_o)}{R^*(s_o)}$
$\boldsymbol{P_l}$	16.7% ± 12.9%	123.9% ± 163.6%
$\boldsymbol{P}$	20.8% ± 15.8%	99.4% ± 124.7%
$\boldsymbol{P_h}$	10.0% ± 9.9%	29.4% ± 38.7%

Table 2.5: The breakdown of risk of accident (mean and the corresponding 95% CI) associated with the optimal policy for the sample 25 trips, starting from state s_o, under $\boldsymbol{P_l}$, $\boldsymbol{P}$, and $\boldsymbol{P_h}$.

TPM	**% location/environment risk,** $\frac{R_e^*(s_o)}{R^*(s_o)}$	**% switching driving entity risk,** $\frac{R_s^*(s_o)}{R^*(s_o)}$
$\boldsymbol{P_l}$	98.2% ± 1.0%	1.8% ± 1.0%
$\boldsymbol{P}$	97.9% ± 1.1%	2.1% ± 1.1%
$\boldsymbol{P_h}$	97.0% ± 1.4%	3.1% ± 1.4%

CI for the means are reported. First, note that the costs under the car-only policy, π^C, are much lower than those under the individual-only policy, π^I. This is mainly because the car is generally considered (and calibrated in the model) to be the safer driving entity (see Appendix B for more details). In addition, consistent with intuition, the mean total expected discounted cost under all policies increase in the risk profile. This is because of the elevated risk of accident during high risk road/environment conditions. Interestingly, the results show a higher average difference in total expected discounted cost between the optimal policy and the benchmark policies, for the low risk profile compared with the high risk profile. This suggests that, under the calibrated TPMs, in lower risk profiles, if switching between driving entities occurs optimally, it can provide even more benefits.

As noted in Table 2.3, the optimal policy results in costs lower than those under the single-entity driving policies π^I and π^C. This is mainly because the risk of accident due to road/environment are lowered through switching driving entities when appropriate. Table 2.4 quantifies the magnitude of change in risk of accident under the three risk profiles for the 25 sample trips, evaluated using the metric $R^{\chi}(\cdot)$, under the switching policy $\pi^{\chi} \in \{\pi^*, \pi^I, \pi^C\}$ introduced in Section 2.3.1. As seen in the table, the mean risk of accident consistently decreases by following the optimal policy, as opposed to the benchmark policies, resulting in a much safer trip on average. Consistent with the results in Table 2.3, the magnitude of change in risk of accident is larger when following π^* as opposed to π^I, compared with when following π^* as opposed to π^C, as in the model, the car is considered to generally be safer than the individual.

Table 2.5 further investigates the breakdown of risk of accident under the optimal policy for the sample 25 trips. Specifically, it provides the distribution of risk of accident, i.e., due to location-environmental-related reasons $R_e^*(\cdot)$ or switching driving entity $R_s^*(\cdot)$, under the optimal policy for the sample 25 trips, starting from state s_o, under $\boldsymbol{P_l}$, $\boldsymbol{P}$, and $\boldsymbol{P_h}$. Similar to previous tables, mean and 95% CI for the mean are provided. First, note that the distribution of risk under benchmark policies are not provided in Table 2.5 as they are trivial; under these policies, a single entity is always in charge and hence, all risks arise due to location-environmental-related reasons. As seen in the table, under the optimal policy, location-environmental-related reasons are responsible for the majority of risk. However, switching also occurs, which, despite introducing new risks, reduces the overall risk of accident as previously seen in Table 2.4. In addition, as seen in Table 2.5, the percentage of switching driving entity risk slightly increases in risk profile. Based on additional experiments conducted, this increase is not necessarily caused by an increase in the average number of switches per trip. Rather, the increase is mainly due to the fact that under a high risk profile, the road/environment condition, ξ, is on average more often in the high risk condition, and based on model calibration, the conditional probability of accident severity following the switch in driving entity, $\boldsymbol{\rho(\mu)}$, is set to be increasing in road/environment condition, ξ (see Appendix B).

Note that so far all results in Section 2.3.1, presented in Tables 2.2-2.5, are obtained where the total expected discounted *cost* of trips are minimized to obtain the optimal policy. In Tables 2.4 and 2.5, we quantify the risks associated with such cost-minimizing optimal policies. We can alternatively minimize the total expected discounted *risk* of trips. These new results are obtained if instead of evaluating the metric $R^*(\cdot)$ under the cost-minimizing policy π^*, value iteration is used to minimize risks. Let $Q^*(s)$ denote the minimum total expected discounted risk of a trip, starting from state s. The resulting risk-minimizing

Table 2.6: Mean percentage difference, and the corresponding 95% CI, between the minimum total expected discounted risk of accident and the total expected discounted risk of accident under benchmark policies for the sample 25 trips, starting from state s_o, under $\boldsymbol{P_l}$, $\boldsymbol{P}$, and $\boldsymbol{P_h}$.

TPM	$\frac{Q^C(s_o)-Q^*(s_o)}{Q^*(s_o)}$	$\frac{Q^I(s_o)-Q^*(s_o)}{Q^*(s_o)}$
$\boldsymbol{P_l}$	47.7% ± 22.0%	146.6% ± 166.9%
$\boldsymbol{P}$	45.4% ± 21.0%	115.5% ± 122.3%
$\boldsymbol{P_h}$	32.9% ± 14.8%	43.7% ± 35.2%

driving entity switching policy treats all types of accidents the same, and essentially ignores costs associated with different types of accidents. Table 2.6 presents the mean percentage difference, and the corresponding 95% CI, between the minimum total expected discounted risk of accident and the total expected discounted risk of accident under benchmark policies for the sample 25 trips, starting from state s_o, under $\boldsymbol{P_l}$, $\boldsymbol{P}$, and $\boldsymbol{P_h}$. Compare this table with Table 2.4. As expected, the risk-minimizing driving entity switching policy in Table 2.6 results in a larger magnitude of change in total risk, compared with the cost-minimizing driving entity switching policy presented in Table 2.4.

Next, we conduct sensitivity analysis on the probability of accident for driving entity ϕ at location-environment $\boldsymbol{\mu}$, $p_\phi(\boldsymbol{\mu})$. Specifically, we decrease and increase the calibrated values for $p_\phi(\boldsymbol{\mu})$ along the sample 25 trips by 20% and 50%, respectively, and examine its impact on the total expected discounted cost. Note that because $p_\phi(\boldsymbol{\mu})$ values are generally low, they do not exceed 1 after the increase. Table 2.7 illustrates the mean total expected discounted cost, and mean percentage difference in total expected discounted cost, under the optimal and benchmark policies for the sample 25 trip starting from state s_o, under three sets of probabilities of accident for the two driving entities. The 95% CI for the means are provided. Note that as in previous cases, the costs under the car-only policy, π^C, are much lower than those under the individual-only policy, π^I, because the car is calibrated in the model to be the safer driving entity. Consistent with intuition, in Table 2.7 the mean total expected discounted cost increases in the probability of accident under all policies. However, it is interesting to note that the change in probability of accident does not greatly impact the degree to which the optimal policy outperforms the single entity driving benchmark policies.

Table 2.7: Mean total expected discounted cost, and mean percentage difference in total expected discounted cost, under the optimal and benchmark policies for the sample 25 trips starting from state s_o, under the corresponding sets of probabilities of accident for the two driving entities. The 95% CI for the means are provided.

Probability of accident	$V^*(s_o)$	$V^C(s_o)$	$V^I(s_o)$	$\frac{V^C(s_o)-V^*(s_o)}{V^*(s_o)}$	$\frac{V^I(s_o)-V^*(s_o)}{V^*(s_o)}$
$0.5 \times p_\phi(\boldsymbol{\mu})$	262.7 ± 26.3	268.4 ± 25.8	449.5 ± 44.1	2.5% ± 2.3%	79.9% ± 26.9%
$0.8 \times p_\phi(\boldsymbol{\mu})$	418.1 ± 41.8	428.9 ± 40.6	717.0 ± 70.1	3.0% ± 2.4%	80.2% ± 26.8%
$p_\phi(\boldsymbol{\mu})$	521.2 ± 52.0	536.0 ± 50.4	894.4 ± 82.3	3.1% ± 2.4%	80.3% ± 26.7%
$1.2 \times p_\phi(\boldsymbol{\mu})$	623.8 ± 64.2	640.6 ± 62.0	1071.1 ± 108.5	3.1% ± 2.4%	80.3% ± 26.6%
$1.5 \times p_\phi(\boldsymbol{\mu})$	777.1 ± 76.9	798.2 ± 74.2	1334.8 ± 129.6	3.1% ± 2.4%	80.3% ± 26.5%

Table 2.8: Mean difference in total expected discounted cost between $V^\chi(s)$, $\pi^\chi \in \{\pi^*, \pi^I, \pi^C\}$, and $U(s)$ for the sample 25 trips starting from state s_0, for the two extreme TPMs $\boldsymbol{P_l}$ and $\boldsymbol{P_h}$. The 95% CI for the means are provided.

Actual TPM	**Miss-specified TPM**	$\frac{U(s_o)-V^*(s_o)}{V^*(s_o)}$	$\frac{V^C(s_o)-U(s_o)}{U(s_o)}$	$\frac{V^I(s_o)-U(s_o)}{U(s_o)}$
$\boldsymbol{P_h}$	$\boldsymbol{P_l}$	0.4% ± 0.7%	1.3% ± 1.5%	69.6% ± 19.2%
$\boldsymbol{P_l}$	$\boldsymbol{P_h}$	0.2% ± 0.4%	3.7% ± 2.5%	90.9% ± 33.3%

Finally, we conduct a robustness analysis to evaluate the extent to which possible estimation errors in transition probabilities can affect the results. Specifically, we investigate the effect of making sub-optimal switches in the driving entity as a result of using a miss-specified TPM. Suppose a car is set to travel during rush hour, where based on historical data, a TPM such as $\boldsymbol{P_h}$, characterizing a high risk level, should be used to find the optimal entity switching policy. However, suppose that on this particular day, a nearby school is closed, which results in a less congested traffic, where based on historical data a TPM such as $\boldsymbol{P_l}$, characterizing a low risk profile, must indeed be used to optimize the trip. Accordingly, in this analysis, we quantify the degree to which such miss-specification of TPM can impact the results.

To facilitate the comparisons, we introduce a new piece of notation. Let $U(s)$ denote the total expected discounted cost-to-go starting from state s that is obtained when implementing the switching policy that is optimal under a *miss-specified* TPM. Clearly, this policy can be sub-optimal under the *actual* TPM, hence $V^*(s) \leq U(s)$.

Table 2.8 illustrates the mean difference in total expected discounted cost between $V^{\chi}(s)$, $\pi^{\chi} \in \{\pi^*, \pi^I, \pi^C\}$, and $U(s)$ for the sample 25 trips starting from state s_0, for the two extreme TPMs $\boldsymbol{P_l}$ and $\boldsymbol{P_h}$. The 95% CI for the means are provided. First, note that despite the difference between the actual and miss-specified TPMs, the mean difference between total expected discounted cost under the optimal and miss-specified policies is relatively small, i.e., up to 0.4% on average. Furthermore, as seen in the last two columns, using the switching policy that is optimal under a miss-specified TPM still, on average, results in better outcomes, compared with the single driving entity benchmark policies. Indeed, for all of the sample 25 trips, the costs obtained under the benchmark policies starting from the starting state, i.e., $V^I(s_0)$ or $V^C(s_0)$, are never lower than those obtained under the miss-specified TPM, $U(s_0)$.

2.3.2 Computational Study Under Partial Information

In this section, we perform numerical experiments to investigate the case where the environmental risk factor is partially observable to the system. As a result, we use the POMDP model solved using the A3C algorithm. We first illustrate the capability of A3C to solve a fully observable case, i.e., the MDP case, for a specific trip setting. Specifically, we compare the cost under the A3C policy compared to the benchmark policies where only the car or individual can drive throughout a trip. We then investigate cases where the environmental risk is observable to different degrees.

We let π^A denote the (near-)optimal policy obtained from solving the POMDP model using A3C. Recall that π^* denotes the optimal policy, and π^C and π^I denote the policies where only the car or the individual can drive, respectively. Analogous to the fully observable case, to facilitate comparisons, we evaluate the total expected discounted costs starting from $z_o = (0, [1, 0, 0], \phi, -1)$, i.e., starting at location $\ell_O = 0$, under the belief that we are in a low risk road/environment state $\boldsymbol{b} = [1, 0, 0]$, with driving entity ϕ, when no switch in authority is scheduled, $d = -1$. Lastly, we let $W^\chi(z)$ denote the total expected discounted cost obtained starting from state z under policy $\pi^\chi \in \{\pi^A, \pi^C, \pi^I\}$. To obtain $W^\chi(z)$, we conduct forward simulation using the formulation in Section 2.2.2 to obtain the total expected discounted cost starting from state z. Specifically, we simulate 50,000 random sample paths according to the particular trip setting of interest, which we let the vehicle navigate while following the policy π^χ. We then report the average total expected discounted cost over the 50,000 sample paths as $W^\chi(z)$.

To illustrate the capability of A3C solving a fully observable case, we generate an example trip. The path and its junction points are as follows: [0, 26, 39, 50], with the following link lengths from the origin to the destination: [26, 13, 11]. This path may be interpreted as follows: Starting from the origin, i.e., location 0, the vehicle first needs to traverse a link of length 26 units to reach location 26. From this location, the vehicle needs to travel through a link of length 13 units to reach location 39. Finally, the vehicle reaches the destination at location 50 after traversing the last link of length 11. In general, in this illustrative example, the car is considered to be a safer driving entity than the individual, and the probabilities $p_\phi(\boldsymbol{\mu})$ and $\zeta_\phi(\boldsymbol{\mu})$ are generated to reflect this assumption. On the second link, however, the probability distributions are changed to create a situation in which the individual would be the safer choice to possibly trigger a change in driving entity. As such, the probability $p_C(\boldsymbol{\mu})$ is increased by 500 folds for low, average and high risk conditions, respectively, on this specific link. As discussed in Section 2.3.1, such increase in risk of accident for the automated driving entity may be related to a road section in which lane changes are poorly implemented due to construction activities, among others.

First, we use this example trip to illustrate the ability of A3C in solving the POMDP model. Note that if the road/environment risk factor is accurately evaluated by the driving entities, i.e., 100% observable, the POMDP model reduces to the MDP model. Hence, we set the accuracy of the road/environment risk level evaluation to 100%, and use A3C to obtain the (near-)optimal policy, which we compare with benchmark policies as well as the optimal policy obtained from solving the MDP model using backward induction. Note that $W^C(z_o) = V^C(s_o)$, and $W^I(z_o) = V^I(s_o)$, hence we simply report the costs $V^C(s_o)$ and $V^I(s_o)$, respectively, as obtained from the backward induction to avoid any estimation errors.

Table 2.9 illustrates the total expected discounted cost, under the A3C and benchmark policies, starting from state z_o. From the table it is seen that following the A3C policy results in a total expected discounted cost that is significantly less than the benchmark policies. Recall that we set the car to be overall a safer driving entity than the the individual. However, due to the increased risk of accident in the second link for the car entity, a high total expected discounted cost of 16,233.9 is obtained following the car-only policy. Compare this with the individual-only policy with a total expected discounted cost of 1,028.6. Under the A3C policy, a total expected cost of 833.2 is incurred, which is substantially lower than those obtained under the benchmark policies. This is because the A3C policy recognizes the dangers of the second road link and switches to the individual driving entity during this link.

It should be noted that when solving the same problem to optimality using backward induction, an optimal cost of $V^*(s_o) = 759.8$ is obtained. Hence, the difference between the solution resulting from implementing the A3C policy and the optimal policy is relatively small, i.e., $833.2 - 759.8 = 73.4$ or approximately 9%. Note that in general, longer training of the A3C algorithm is expected to result in improvements in the approximate solution (Mnih et al., 2016).

Finally, we investigate the effect of partial observability on the solutions. To do so, we generate two cases, in which we account for a lowered degree of observability, i.e., possibility of error in road/environment risk level evaluation. Under 'complete' observability, as in the previous example, it is assumed that road/environment risk level evaluation is 100% accurate.

Table 2.9: Total expected discounted cost under the A3C policy and benchmark policies, starting from state z_o.

$W^A(z_o)$	$W^C(z_o)$	$W^I(z_o)$
833.2	16,233.9	1,028.6

Table 2.10: Total expected discounted cost, $W^A(z_o)$, under various degrees of observability, starting from state z_o.

Total expected discounted cost, $W^A(z_o)$		
Complete observability	Average observability	Limited observability
833.2	850.9	874.8

We next generate an 'average' case in which the road/environment risk level evaluation is only 95% accurate, allowing for 2.5% miss-classification of a risk level as the other two risk level, i.e.,

$$\begin{bmatrix} 0.95 & 0.025 & 0.025 \\ 0.025 & 0.95 & 0.025 \\ 0.025 & 0.025 & 0.95 \end{bmatrix}.$$

Similarly, we generate a 'limited' observable case in which the road/environment risk level evaluation is only 90% accurate, allowing for 5% miss-classification of a risk level as the other two risk level.

Table 2.10 illustrates the total expected discounted cost under various degrees of observability, starting form state z_o. From the table, it is seen that the total expected discounted cost increases as the observability of the road/environment risk factor decreases. This is due to the uncertainty created regarding the actual condition of the road/environment risk factor, sometimes resulting in sub-optimal switches in driving authority. However, it is noted that these reported costs (under the A3C policy) in the partially observable environment are still substantially less than the costs under the benchmark policies.

2.4 Conclusion and Future Work

This chapter presents a framework for determining the cost-minimizing control-authority switching policy in semi-autonomous vehicles. Specifically, we develop an MDP model that determines the authority in charge at any point along a trip, as a function of the current location and road-environment conditions. The model considers not only the risk of accident due to location/environmental-related reasons, but also that due to switching driving entities. To that end, it also accounts for the current entity in charge and the time to any previously scheduled switch to prescribe actions. The goal is to determine the optimal driving entity at each point in time to minimize the total expected discounted safety cost of a trip. The framework is set up such that it accounts for a delay in authority transfer to the human driver who may be affected by OOTL. Costs are considered for false switching alerts that do not take effect to help prevent alarm fatigue in drivers. In addition, we develop a partially observed Markov decision process (POMDP) model where it is assumed that the risk posed by the immediate environment is only partially observed. We solve the POMDP using the asynchronous advantage actor-critic (A3C) algorithm.

This framework facilitates understanding and quantifying the risks and benefits involved in the control authority transitions in semi-autonomous vehicles where the driver is expected to take over control of the vehicle under certain conditions. In addition, with the necessary model calibration, the framework can be used by city planners and policy makers to investigate the type of network (e.g., urban/suburban) in which one driving entity would outperform the other. Such an investigation would allow for the identification of characteristics/dynamics of regions that would be appropriate candidates for certain levels of automation, or not suitable for autonomous driving at all. Different regions can be modeled through the one-step transition probability matrix that quantifies the dynamics of the environment and the probability of accident for a given driving entity. In addition, such an investigation would allow policy makers to compare and contrast the controllable factors that make a region suitable for autonomous driving.

Before this model can be directly used in practice, it needs to be calibrated for real-world applications. To calibrate the models, some parameters may be readily obtained from the literature, e.g., cost of accidents. Other parameters, however, may require additional estimation efforts. For instance, an important part of our models is a set of probability distributions that quantify the risks of manual driving, autonomous driving, and authority switching under various driving scenarios. Although data to estimate these probability distributions with a high degree of accuracy is not readily available, it is possible to approximate such distributions. Specifically, we use the existing literature to obtain probability distributions for accident severity in the manual driving mode under various driving scenarios. For autonomous driving, one could examine the failure records of autonomous features currently on-board of vehicles (e.g., brake assist, blind spot assist, active lane keeping assist, adaptive cruise control) to estimate the likelihood of elevated risk due to such failures. Finally, the existing literature on driver perception-reaction times may be used to quantify the level of driver distraction and its associated risks after being disengaged from the driving environment for an extended period of time.

Various extensions can be considered to improve the practicality of the proposed method. For instance, in this work, we present the optimal driving-entity switching policy given a fixed route. Clearly, the route choice itself may impact the expected safety of a trip. Note that conventional passenger vehicle route guidance systems aim to direct vehicles from their origin to destination so as to minimize travel time, maximize fuel efficiency, etc., but not directly to maximize safety as it pertains to autonomous and semi-autonomous driving. Hence, as a future work, we aim to extend the current model to also account for dynamic routing to maximize safety. That is, the extended model would determine the optimal path as well as the optimal driving entity in charge, as a function of road and environmental factors, to minimize the safety risk of a trip, or equivalently to minimize the total expected discounted cost/harm of possible accidents. This will further increase the complexity of the model and the number of decisions, possibly requiring the use of approximate solution strategies to solve the problem.

Chapter 3

A Dynamic Deep Reinforcement Learning-Bayesian Framework for Anomaly Detection

Disclosure: This chapter is based on a paper submitted by van Wyk et al. (2019) to IEEE Transactions on Intelligent Transportation Systems.

van Wyk, F., Watts, J., Khojandi, A. and Masoud, N., 2019. A Dynamic Deep Reinforcement Learning-Bayesian Framework for Anomaly Detection. IEEE Transactions on Intelligent Transportation Systems.

My contributions to this paper include: (i) the development of the problem, (ii) reviewing the appropriate literature, (iii) the identification of study objectives, (iv) design and conducting of the numerical experiments, (v) majority of the writing responsibilities of the manuscript.

Abstract

The successful operation of connected and automated vehicles depends on a large number of information sources such as on-board sensors, roadside units, cloud data, and other vehicles. As a result, these vehicles are susceptible to false/incorrect information, originating from malicious or non-malicious sources, which could have fatal consequences if not processed correctly. It is therefore critical to detect and isolate anomalous and/or faulty information in a timely manner. To do so, anomaly detection techniques should be implemented in real-time where if the probability of anomalous information exceeds a certain threshold, the information is dealt with accordingly. Traditionally, in the literature, the threshold that determines if information is anomalous or not, is fixed and determined *a priori*. However, this approach not only does not account for the feedback obtained during a trip on the performance of the algorithms, but also fails to respond to potential changes in rates of anomalies. Hence, it is important to develop an approach that can dynamically alter this threshold in response to exogenous factors to assure reliable and robust system operation. In this study, we develop a mathematical framework to determine the optimal dynamic threshold of an anomaly classification algorithm in order to maximize the safety of a trip. Specifically, we develop and pair an anomaly classification algorithm based on convolutional neural networks (CNN), with a partially observable Markov decision process (POMDP) model. We solve the resulting POMDP model using the asynchronous advantage actor critic

(A3C) deep reinforcement learning algorithm. The prescribed policy determines the optimal level of anomaly classification threshold in real-time that maximizes the performance. Our numerical experiments suggest that the addition of the A3C model improves the anomaly detection performance of the CNN, resulting in high accuracy, sensitivity, and positive predictive value.

3.1 Introduction

In recent times, the transportation community has directed considerable research efforts into the development of various aspects of an intelligent transportation system (ITS). An ITS includes numerous concepts such as traffic management, traveler information systems, and intelligent vehicle capabilities (Ni, 2015). These measures aim to relieve traffic congestion, improve transportation mobility, reduce emissions, enhance user experience, and improve safety. Connected and automated vehicles (CAVs) are expected to be an integral part of achieving the aforementioned ITS objectives (Rios-Torres and Malikopoulos, 2016).

CAVs make use of an array of sensors and communication technologies to control vehicle operation in a safe and efficient manner. CAVs use sensors such as cameras, ultrasonic sensors, radar, and LiDAR to capture the driving environment in order to operate the vehicle autonomously (with varying degrees of autonomy) (NHTSA, 2013). In addition, connected vehicles communication (V2X) is facilitated through wireless technologies such as dedicated short range communications (DSRC) and long-term evolution-advanced (LTE-A) which allow CAVs to transmit relevant information to other vehicles, roadside infrastructure, and devices. The implementation of these technologies are expected to drastically reduce the approximately 94% of serious crashes in which human error plays a decisive role (Singh, 2015).

While there are many advantages associated with the implementation of CAV technologies, the potential dangers associated with them should not be neglected. The safe operation of CAVs is highly dependent on the information they obtain from their sensors and wireless communication sources. As a result, there exist a great number of sources in which false information may be present, which poses great risk to the safe operation of CAVs. The false information may be from a malicious source, i.e., a cyber attack, or from a non-malicious source such as faulty sensors. It should be noted that both origins of false information represent significant threats to the safe operation of CAVs.

There is a rapidly growing body of literature illustrating the potential dangers of CAV technologies resulting in anomalous/false information (Petit and Shladover, 2015; Koscher et al., 2010; Weimerskirch and Gaynier, 2015; Parkinson et al., 2017). For instance, illustrating the injection of anomalous/false information with a malicious intent, researchers showed that it is possible to interfere with LiDAR systems of CAVs by artificially creating obstacles in the perceived environment using a laser and a pulse generator (Curtis, 2015). Illustrating the injection of false information from a source with a non-malicious intent, researchers found that under certain environmental conditions such as bright light, heavy snow, and poor quality of road and traffic signs, CAVs can malfunction and perceive the driving environment incorrectly (Moavenzadeh and Lang, 2018; Field, 2017). As a result, anomalous/false sensor values, originating from sources with malicious or non-malicious intent, can result in dangerous circumstances for CAVs. It is therefore critical that anomaly detection techniques are implemented to detect anomalous/faulty information in CAVs.

There exists a large body of research in anomaly detection (e.g., see surveys by (Chandola et al., 2009; Ahmed et al., 2016)). A significant number of these anomaly detection algorithms apply classification algorithms, where labeled data instances are used to train a model (classifier). In the testing phase, each test instance is assigned a probability of belonging to a certain class by the trained model. For instance, in binary classification, this probability is translated into two classes (normal/anomalous) using an 'a priori' cut-off, e.g., 0.5. Generally, the classification threshold is determined to balance sensitivity (the proportion of anomalous instances correctly classified) and specificity (the proportion of non-anomalous instances correctly classified). Two types of errors may occur when classifying instances: (1) classifying an anomalous instance as normal (non-anomalous), i.e., false negatives; (2) classifying a normal instance as anomalous, i.e., false positives. False negatives are a clear concern in most applications. However, false positives can also have major consequences. For instance, in the classification of anomalous sensor values, false positives may eventually lead to the false exclusion of non-anomalous sensor data from the data fusion process. This can have a detrimental impact on the quality of fused data and potentially compromise the autonomous operation of the vehicle.

In the literature, classification models used to detect anomalous information are mostly used in isolation and in a myopic manner. That is, after being built, a classification model remains unchanged regardless of the past success rate experienced within the system of interest (Kruegel et al., 2003). Indeed, most models, even when they are designed to be used in an online fashion, such as throughout a CAV trip, they are simply trained to present the best performance (e.g., high accuracy, sensitivity, or F-1 score) under *an expected trajectory*, e.g., 5% anomaly rate. Although such a strategy *on average* works well, it falls short of reacting to the real-time information experienced/gained throughout a specific *sample path or sequence of events.* Online machine learning tries to somewhat combat this issue by (re-)learning the model parameters over time, in response to the new experiences gained. However, such learning can be relatively slow and fail to respond in a timely manner to the temporary changes in the environment as it relates to cyber threats faced from other moving vehicles or stationary roadside units (RSUs) with limited ranges. In addition, by the time the model 'learns' to respond to such threats, the environments may have completely changed and the newly learned parameters may cause worse performance.

To address these issues, a decision-making system is needed to quickly respond to changes in the environment, without a long time lag or too much dependency on long-term memory. This can be achieved by dynamically adjusting the classification threshold, as opposed to a constant threshold, based on the complexity of the environment and previously learned information (e.g., performance metrics in the last n time epochs) to respond to the temporal changes in a timely manner. Dynamic thresholds have been proposed in various applications (Kalmuk et al., 2016; Arad et al., 2013; Idé and Kashima, 2004). However, to the best of our knowledge, the framework presented in this study is the first application of dynamic classification thresholds in the transportation domain with the objective of anomaly detection.

In this work, we develop a partially observable Markov decision process (POMDP) model to prescribe the level of the threshold used in an anomaly detection algorithm, in real-time, to minimize the total expected 'cost' of false positives/negatives during a CAV trip. Specifically, the POMDP model makes decisions about the classification threshold as a function of the belief about the core state of the system, the perceived past anomaly detection performance during a CAV trip, the classification threshold used during the past epoch, and an imperfect 'observation' received about the current state of the system. The inclusion of these parameters assures that both long-term and short-term past performance and beliefs about the state of the system are considered when making decisions.

Solving POMDP models using exact approaches are often intractable due to the curse of dimensionality (Roy et al., 2005). Reinforcement learning based approaches can hence be used to solve such problems. In reinforcement learning (RL), for a system in state s, an agent chooses an action a to maximize its total discounted future rewards in a given environment (Sutton and Barto, 2018). This process is typically repeated until the most likely sample paths are all explored and the 'best' actions and rewards starting from any state are estimated. If the size of the policy space is too large, RL is typically not tractable as it requires too many iterations to explore the most likely sample paths to accurately estimate 'best' actions and rewards. Deep reinforcement learning (DRL) attempts to alleviate this problem by using the information collected from limited exploration of the policy space to estimate the actions and rewards starting from the states that are not often, if ever, explored.

Advances in computation capabilities in the past decade have led to substantial growth in using DRL algorithms in many domains. DRL combines the traditional strengths of neural networks with reinforcement learning algorithms. Neural networks are known for their time series prediction, machine vision, and classification capabilities while reinforcement learning focuses on the correlation of immediate actions with the future rewards they produce. Popular applications of DRL algorithms include teaching machines to play video games using the screen display as input (Mnih et al., 2016) or solving problems such as robotic control (Levine et al., 2016) and control of ramp metering (Belletti et al., 2017). The emergence of policy gradient-based methods such as the asynchronous advantage actor critic (A3C) (Mnih et al., 2015) algorithm have enabled the use of continuous action space and state space. This development addressed the curse of dimensionality problem faced by Q-learning approaches (Lillicrap et al., 2015) for large problems. Despite the potential of DRL techniques in anomaly detection, a review of the literature indicates that its application is very limited in this domain. Anomaly detection using DRL have been proposed by de La Bourdonnaye et al. (2017) to learn binocular fixations and by Huang et al. (2018) for a threshold-free detector in network time series problems. However, these studies do not focus on anomaly detection in transportation and the models do not incorporate observations in a hierarchical manner, as proposed in our framework.

In this study, we solve the POMDP model using the A3C algorithm and compare the results with a benchmark convolutional neural network (CNN) model, as developed in van Wyk et al. (2019). To the best of our knowledge, this is the first application of the A3C algorithm in a partially observable environment for the purpose of anomaly detection in the transportation domain.

Consistent with the CNN model and definitions for anomalies used by van Wyk et al. (2019), we train, validate, and test the benchmark model accordingly. We provide numerical experiments in which we compare the performance of the POMDP model with benchmark policies, i.e., CNN-only models with a fixed threshold throughout a trip. We provide numerical experiments for trips with various parameter settings to obtain further insights.

The main contributions of this work are as follows: (*i*) We embed CNN into a Bayesian framework, where instead of relying on the *raw* predictions of CNN on whether sensors are faulty/attacked, we use the CNN predictions as 'imperfect observations,' fed into a Bayesian framework for further processing; (*ii*) we further incorporate the recent trip trajectory (or history) into the Bayesian framework to more actively react to environmental changes and anomaly rates during a trip. The developed framework is extremely flexible and allows for a large degree of control over penalizing false positives/negatives to various degrees in different applications; (*iii*) we use A3C to solve a mathematical POMDP model, as opposed to existing studies using A3C where the underlying model is a structured emulator (e.g., a video game).

The rest of the chapter is organized as follows. In Section 3.2, we describe our framework. Specifically, we provide details for the POMDP model and the A3C training process and how the CNN is incorporated in the classification process. In Section 3.3, we describe the data set we use for training, validating, and testing the various approaches. In Section 3.4, we perform various numerical experiments to investigate the anomaly detection performance of the approaches under various parameter settings. Lastly, we conclude in Section 3.5.

3.2 Methods

In this section, we develop a framework to adaptively prescribe the anomaly classification threshold to improve the anomaly detection performance. In this study, we assume the true state of the system, i.e., normal or anomalous, is unknown. Hence, we use a Bayesian model to update the beliefs about the underlying state of the system. In this Bayesian model, specifically the POMDP model, we associate 'costs' to incurring false positives/negatives, and develop a solution strategy that aims to minimize the trip-specific total expected cost. Specifically, we solve this model with the A3C algorithm since POMDPs suffer from the curse of dimensionality and the problem investigated in this study has a large state space and continuous action space. As a result, exact methods are intractable for the problem investigated here.

In the following, we first provide an overview of the framework. Next, we discuss the two main components used in developing and solving the models, namely, POMDP and A3C algorithm.

Figure 3.1 illustrates an overview of the anomaly detection framework proposed in this study. At each time epoch, the sensor readings collected within the past several time epochs (using a fixed width sliding window) are used as an input to the CNN model. It should be noted that the CNN model can be replaced by any other classification model producing a probability of belonging to a certain class. The CNN model outputs a probability of the sensor data being anomalous at each time epoch. Next, the CNN output probabilities, plus a few additional problem-specific features, are fed into the POMDP model. The POMDP model is solved to (approximate) optimality using A3C algorithm to obtain the policy that prescribes anomaly classification threshold for any given system belief state. This policy can be used to discriminate normal and anomalous readings by the control system of the CAV in real-time.

The CNN model used in this study is based on that developed in van Wyk et al. (2019). This CNN model uses a traditional image recognition architecture, and the Adam optimizer from Tensorflow in Python is implemented to minimize binary cross-entropy Kingma and Ba

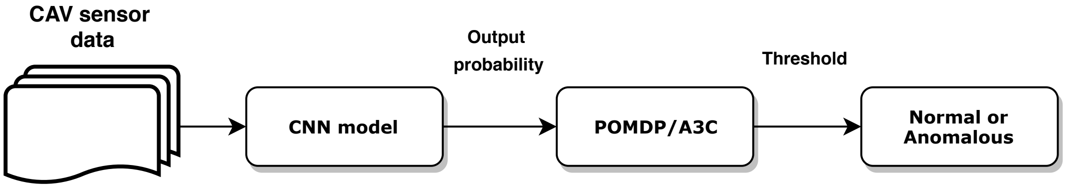

Figure 3.1: Overview of the anomaly detection framework. At each time epoch, the sensor readings collected within the past several time epochs are used as an input to the CNN model. The CNN model outputs the probability of the sensor data being anomalous at each time epoch. Next, the CNN output probabilities, plus a few additional problem-specific features, are fed into the POMDP model as 'imperfect observations.' The POMDP model is solved to (approximate) optimality using the A3C algorithm to obtain the policy that prescribes the anomaly classification threshold for any given system belief state, discriminating normal and anomalous sensor readings.

(2014). In addition, to reduce the risk of overfitting, random dropout and an early stopping algorithm monitoring the validation set accuracy, are used.

3.2.1 POMDP

Partially observable Markov decision processes (POMDPs) are described as a six-tuple (S, A, O, P, Ψ, R) with a set of states S, a set of actions A, a set of observations O, a transition probability matrix P, an information matrix Ψ, and a reward function R, which is dependent upon the state and the action taken. At each decision epoch $t = 0, 1, 2..., T : T < \infty$ the system is at a core state $s_t \in S$, which represents the true state of the system. We let $S = \{0, 1\}$, where the states '0' and '1' correspond to normal and anomalous states, respectively.

Let $\boldsymbol{\pi}_t = [\pi_0, \pi_1]$ denote the belief about the core state at time t, where π_0 and π_1 denote the probabilities that system is in non-anomalous and anomalous states, respectively. Note that $\pi_0 + \pi_1 = 1$. To more explicitly account for the immediate history, i.e., last n time epochs, we augment the belief vector $\boldsymbol{\pi}_t$, with the perceived past anomaly detection performance during a CAV trip, and the classification threshold used during the past epoch. Specifically, we let $b_t = [\boldsymbol{\pi}_t, \alpha, \beta, a_{t-1}] \in B$ denote the belief state of the process at time t, where α and β denote the expected weighted false negative (FN) and false positive (FP) rates over the past m decision epochs, respectively, and a_{t-1} denotes the action, i.e. the classification threshold, used in the previous time epoch $t-1$.

Recall that the system core state is only partially observable to the model. Hence, at each time epoch t, an observation $o_t \in O = [0,1]$ is made, which provides imperfect information about the system core state. In our context, this observation is the CNN-estimated probability that the system is in the anomalous state. Once an observation is made, an action $a_t \in A = [0,1]$ is taken, as a function of belief state b_t and the observation o_t to adjust the the classification threshold.

At every decision epoch, the system incurs an immediate reward as function of the action a_t taken in belief state b_t. This immediate reward accounts for whether the threshold chosen is expected to correctly detect anomalous and normal readings. That is, the system is rewarded by a unit of one for true positives (TP) and true negatives (TN), and is penalized by a unit of one for false positives (FP) and false negatives (FN), i.e., $R_{TP} = R_{TN} = 1$ and $R_{FP} = R_{FN} = -1$. In addition, it is further rewarded/penalized based on the weighted expected rates of FN and FP in the past m time epochs in addition to the current expected value. The rewards function $R(\cdot)$ is as follows:

$$R_t(b,o,a) =$$
$$\begin{cases} \pi_0 \cdot R_{TN} + \pi_1 \cdot R_{FN} + \alpha \cdot R_{FN}, & \text{if } o_t < a_t, \\ \pi_0 \cdot R_{FP} + \pi_1 \cdot R_{TP} + \beta \cdot R_{FP}, & \text{if } o_t \geq a_t. \end{cases}$$

In the beginning of time epoch $t+1$, the belief state b_t is updated to obtain b_{t+1}. Specifically, the belief about the new core state $s' \in S$ at time $t+1$ is updated as follows:

$$\pi_{s'} = \frac{\Psi\left(\mathbb{1}_{\{o>a\}}|s'\right) \sum\limits_{s\in S} P(s'|s) \cdot \pi_s}{\sum\limits_{o\in O} \Psi\left(\mathbb{1}_{\{o>a\}}|s'\right) \sum\limits_{s\in S} P(s'|s) \cdot \pi_s} \tag{3.1}$$

where $P(s'|s)$ denotes the probability that system core state transitions from state s to state s', and $\Psi\left(\mathbb{1}_{\{o>a\}}|s'\right)$ denotes the probability that the observed system state is anomalous/non-anomalous given the core state s'.

$$\alpha' = \frac{\alpha \cdot m + \mathbb{1}_{\{a>o\}} \cdot \pi_1}{m+1}, \tag{3.2}$$

$$\beta' = \frac{\beta \cdot m + \mathbb{1}_{\{a\leq o\}} \cdot \pi_0}{m+1}. \tag{3.3}$$

Finally, we let γ denote the discount factor and $V_t(b)$ give the maximum total expected discounted reward starting from belief state b_t, i.e.,

$$\begin{aligned} V_t(b) = \max_{a\in A}\{R_t(b,a,o) + \gamma \sum_{o\in O}\sum_{s'\in S} \Psi\left(\mathbb{1}_{\{o>a\}}|s'\right) \\ \sum_{s\in S} \pi_s \cdot P(s'|s) \cdot V_{t+1}(b)\}. \end{aligned} \tag{3.4}$$

For the terminal case $t = T$, the expected discounted reward is given by $V_T(b) = R_T(b, o, a)$.

3.2.2 A3C

We use the A3C algorithm to solve the developed POMDP model. In the A3C algorithm, being an *actor-critic* method, a critic learns the value function while the actor interacts with the environment attempting to learn a policy to maximize/minimize a given objective function. Among the common DRL algorithms such as deep Q-network (DQN), double DQN, etc. (Mnih et al. (2016); Van Hasselt et al. (2016)), A3C generally achieves the best performance and it is suitable for both discrete and continuous spaces (Mnih et al., 2016). In addition, the training time for A3C is substantially less and, in general, obtains more robust policies compared to other DRL techniques. The A3C algorithm achieves this by exploring the environment with multiple agents in parallel on multiple threads.

To reduce the correlation between training episodes, other DRL algorithms often utilize a technique called *experience replay.* A3C reduces correlation by creating a copy of the environment for each agent during the training process and updating the global/master network *asynchronously.* Therefore, after every gradient update, each of the individual agents synchronize their weights with the global network.

The A3C algorithm (Mnih et al., 2016) maintains a policy $\pi(a_t|s_t;\phi)$, where a_t denotes the action at time t, s_t denotes the state, and ϕ denotes the parameters of the global actor network. The algorithm also estimates a value function $V(s_t;\phi_v)$, for state s_t using parameters ϕ_v for the global critic network. The value function is updated with n-step returns. The policy and the value networks are updated after every episode of length t_{max} or when a terminal state is reached.

The A3C algorithm uses *advantage*, as opposed to Q-values in many other DRL algorithms, to estimate how advantageous certain actions are for a particular state. The advantage function $A(\cdot)$ is estimated as follows:

$$A(s_t,a_t;\phi,\phi_v) = \sum_{i=0}^{k-1} \gamma^i r_{t+i} + \gamma^k V(s_{t+k};\phi_v) - V(s_t;\phi_v), \tag{3.5}$$

where k is bounded above by t_{max}.

The gradient update to minimize total loss can be seen as

$$\nabla_{\phi'} \log \pi(a_t|s_t;\phi') A(s_t,a_t;\phi,\phi_v), \tag{3.6}$$

where ϕ' is the thread-specific network parameters. Also, Mnih et al. (2016) found that if the entropy of policy π is added to the objective function, exploration is encouraged which limits the premature convergence to sub-optimal deterministic policies. As a result, the gradient of the objective function which includes an entropy regularization term with respect to the policy parameters is given as

$$\nabla_{\phi'} \log \pi(a_t|s_t;\phi') A(s_t,a_t;\phi,\phi_v) + \eta \nabla_{\phi'} H(\pi(s_t;\phi')), \tag{3.7}$$

where H is the policy entropy and the parameter η controls the strength of the entropy regularization term.

To solve the POMDP model with the A3C algorithm, we use TensorFlow (Abadi et al., 2016) in Python where we utilize the RMSProp optimizer (Tieleman and Hinton, 2012) for training the neural networks of the actor and critic. Table 3.1 illustrates a summary of the hyperparameters used in the model during the training process.

Table 3.1: Hyperparameters utilized in the training of the A3C model.

Hyperparameter	Value	Description
Maximum Global Episodes	25000	Total number of training sample paths generated
Discount Factor (γ)	1	Parameter used to discount future rewards
Global Update Iterations	10	Number of epochs between global parameter updates
Entropy Regularization (η)	0.001	Encourages exploration of various policies
Window Size	10	The number of past epochs used to weight FN and FP incurred
Neural Network Nodes	100	Number of nodes in each hidden layer
Actor Learning Rate	0.001	Rate used by RMSProp optimizer for actor network
Critic Learning Rate	0.001	Rate used by RMSProp optimizer for critic network

3.3 Data

The data used in the numerical experiments for this study are obtained from the research data exchange (RDE) database for the Safety Pilot Model Deployment (SPMD) program (Bezzina and Sayer, 2014). The SPMD program was conducted to demonstrate the feasibility of CAVs, investigating V2X technologies in real-world conditions. Data were collected from on-board vehicle devices as well as roadside units (RSUs) including basic safety messages (BSM), signal phase and timing (SPaT) messages, vehicle trajectories, and data for driver-vehicle interactions. Data were collected for approximately 3,000 vehicles over a period of two years with a collection frequency of 100 ms for selected variables.

Consistent with van Wyk et al. (2019), in-vehicle speed, GPS speed, and in-vehicle acceleration are extracted from the data set to use in the numerical study. Also, we use the anomaly simulation process found in van Wyk et al. (2019) to generate the 'bias' and 'gradual drift' anomaly types where anomalies are added at specified rates ξ (dependent on the experiment). Specifically, for the bias anomaly type, the anomaly magnitude is sampled from a uniform distribution $\mathcal{U}(0, 5)$, where the sampled magnitude is added to all true sensor readings for a time period of 10 epochs. Similarly, for the gradual drift anomaly type, a vector of linearly increasing values from 0 to 2, for a duration of 10 epochs are added to all true sensor readings.

Figure 3.2 illustrates how the data set (consisting of in-vehicle speed, GPS speed, and in-vehicle acceleration) that is augmented with anomalous readings is used to train and test the various components of the framework. First, a portion of the data is set aside to train and validate the CNN model. The trained CNN model is then used to generate probabilities

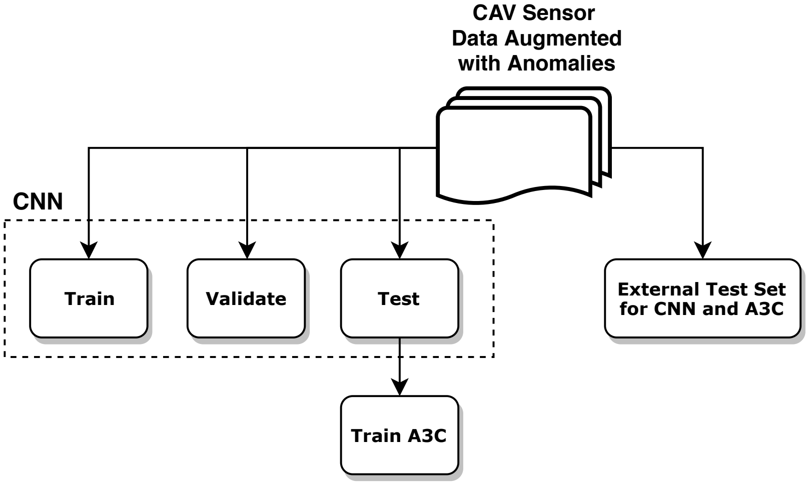

Figure 3.2: Illustration of data breakdown and flow of information. The CNN model is trained and validated using CAV sensor data. The CNN model is then used to generate probability streams of the system being anomalous on an internal test set. These probabilities are used as observations in the POMDP model trained by the A3C algorithm. Finally, an external test set is used to compare the performance of the CNN-only and A3C models.

of the system being anomalous on an internal test set. These probability streams are used in the POMDP model as *observations* when training the A3C algorithm. Finally, to compare performance and investigate the value of adding the A3C model, an external/unseen test set is used and the results are presented in the numerical study.

3.4 Results

In this section, we perform various analyses to investigate the anomaly detection performance of the models discussed in Section 3.2. We first investigate the performance of the CNN and A3C models where the anomaly rate is fixed and the trip length is varied for both anomaly types. This experiment presents the value that A3C can provide over time. Next, we investigate the performance of the CNN and A3C models where we fix the trip length and vary the anomaly rate for both anomaly types. This experiment can help showcase the potential of using A3C in a dynamic road environment where the rate of anomaly changes as the CAV drives through the network. Lastly, we illustrate the performance of the two models for an anomaly encountered in a sample path.

Throughout our analyses, we evaluate the performance of the models in terms of accuracy, sensitivity, specificity, positive predictive value (PPV), and F1 score. We consider F1 score, a balance between sensitivity and PPV, as the main metric of comparison between the models. To highlight the percentage improvement in error rate between the F1 scores of the CNN and A3C models, we also introduce the metric $\Delta Improve$, i.e.,

$$\Delta Improve = \frac{F1_{A3C} - F1_{CNN}}{100 - F1_{CNN}} \cdot 100\%.$$

For all experiments, we test the models using 10 distinct sample paths and present the mean and 95% confidence interval (CI) for the performance metrics.

3.4.1 Performance Under Fixed Anomaly Rate

In this section, we compare the performance of the CNN and A3C models for a fixed anomaly rate of $\xi = 5\%$ (in the test sets), and vary the trip length T for both the bias and gradual drift anomaly types. All models are trained using an anomaly rate of 5%. The experimental design is illustrated in Fig. 3.3. This setup represents the effects of different time exposures to anomalous events from a single roadside unit, assuming the roadside unit is responsible for the injection of anomalies, and evaluates the ability of A3C and CNN to determine the presence of anomalies in a trip. Specifically, for an anomaly rate of $\xi = 5\%$, we vary the trip length to be $T \in \{5000, 15000, 25000\}$. These trip lengths represent the total number of decision epochs at which a decision/classification is made as to whether the system is normal or anomalous, with each epoch equivalent to a travel time of 0.1s.

Table 3.2 illustrates the mean and 95% CI for the performance metrics for various trip lengths for the bias anomaly type. First, note that as the trip length increases, the anomaly detection performance slightly decreases for both CNN and A3C. This is expected as anomalies occur randomly over time and during relatively short trips, e.g., $T = 5000$, few anomalies may be present. Also, in general, it is seen that the A3C model outperforms the CNN model across the considered trip lengths. This is particularly reflected by the $\Delta Improve$ metric. Specifically, we conduct paired t-tests to investigate the difference in F1 score between the CNN and A3C models. The obtained p-values indicate statistical significance at a 5% level

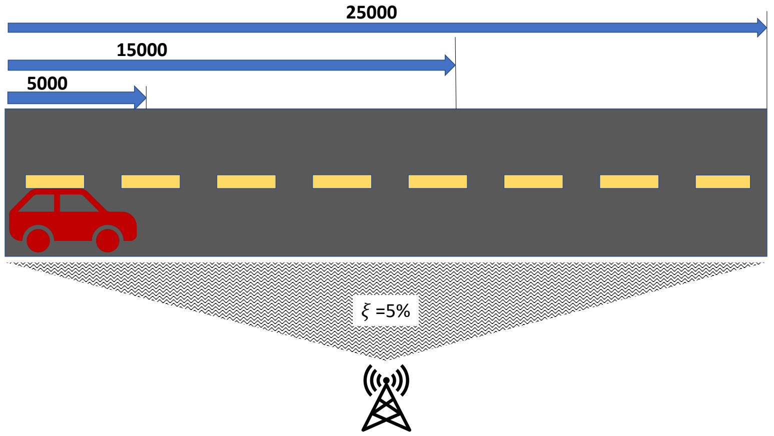

Figure 3.3: Illustration of a sample path with a fixed anomaly rate and different trip lengths. A fixed anomaly rate of $\xi = 5\%$ is used for trips with lengths of 5000, 15000, and 25000 epochs.

(p-value < 0.05) for all trip lengths considered. It is important to note that in our preliminary experiments with very short trip lengths, e.g., $T = 200$, the improvement in F1 score was not always statistically significant. This is mainly because not many anomalies are encountered in very short trip lengths due to the low anomaly rate. As a result, there are very few opportunities (anomalies) for A3C to improve upon the performance of CNN.

Table 3.3 illustrates the mean and 95% CI for the performance metrics for various trip lengths for the gradual drift anomaly type. Similar to Table 3.2, overall the anomaly detection performance slightly decreases for both CNN and A3C as trip length increases. In addition, from the results, it is seen that A3C improves upon the F1 score of CNN for all trip lengths. The obtained p-values from a paired t-test for F1 score indicate statistical significance at a 5% level (p-value < 0.05) for all trip lengths.

3.4.2 Performance Under Variable Anomaly Rate

In this section, we investigate the effect of having different anomaly rates in a trip. First, we train and test the CNN model under various anomaly rates for the bias anomaly type to gain insights into the importance of knowing the test environment's anomaly rate. We then use the best performing CNN based on this experiment, and compare its performance for a variable anomaly rate and fixed trip length for both the bias and gradual drift anomaly

Table 3.2: The mean and 95% CI anomaly detection performance of the bias anomaly type for a fixed anomaly rate, $\xi = 5\%$, and various trip lengths. P-values indicate statistical significance at 5% level using paired t-tests, between the F1 scores for the CNN and A3C models for all trip lengths.

	$T = 5000$		$T = 15000$		$T = 25000$	
	A3C	CNN	A3C	CNN	A3C	CNN
Accuracy	97.48	97.30	96.91	96.79	96.38	96.27
	±0.40	±0.40	±0.13	±0.12	±0.09	±0.18
Sensitivity	91.76	91.10	90.99	90.48	90.56	89.92
	±1.37	±1.36	±0.51	±0.49	±0.41	±0.37
Specificity	99.89	99.90	99.30	99.35	98.75	98.86
	±0.06	±0.05	±0.10	±0.11	±0.07	±0.11
PPV	99.73	99.76	98.13	98.25	96.72	96.98
	±0.16	±0.13	±0.30	±0.33	±0.27	±0.37
F1 score	95.57	95.22	94.43	94.20	93.54	93.32
	±0.76	±0.74	±0.30	±0.29	±0.27	±0.30
Δ Improve	7.58 ± 0.03%		3.94± 0.01%		3.32 ± 0.01%	

Table 3.3: The mean and 95% CI anomaly detection performance of the gradual drift anomaly type for a fixed anomaly rate, $\xi = 5\%$, and various trip lengths. P-values indicate statistical significance at 5% level using paired t-tests, between the F1 scores for the CNN and A3C models for all trip lengths.

	$T = 5000$		$T = 15000$		$T = 25000$	
	A3C	CNN	A3C	CNN	A3C	CNN
Accuracy	96.75	96.52	95.53	95.17	94.81	94.64
	±0.20	±0.20	±0.15	±0.15	±0.35	±0.41
Sensitivity	89.94	89.99	90.00	90.38	88.88	86.24
	±0.53	±0.46	±0.36	±0.32	±0.64	±0.62
Specificity	99.63	99.29	97.78	97.12	97.23	96.99
	±0.27	±0.24	±0.24	±0.26	±0.26	±0.34
PPV	99.00	98.14	94.21	92.66	92.89	92.32
	±0.76	±0.68	±0.71	±0.81	±0.74	±0.92
F1 score	94.25	93.89	92.05	91.50	90.84	90.58
	±0.43	±0.37	±0.36	±0.41	±0.65	±0.73
Δ Improve	5.77 ± 0.07%		6.35± 0.02%		2.65±0.01%	

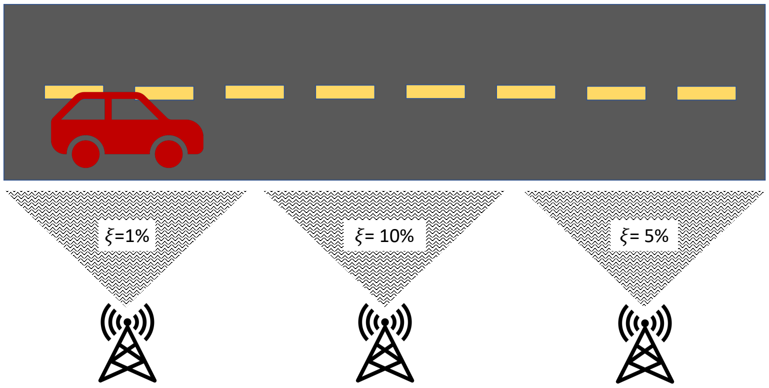

Figure 3.4: Illustration of a sample path with different rates of anomaly for road segments with a fixed length. In this sample path, the CAV goes through three road segments where it communicates with RSUs that can inject anomalies at different rates, i.e., starting from ξ = 1%, anomaly rate first increases to $\xi = 10\%$ and then decreases to $\xi = 5\%$.

types. The experimental design is illustrated in Fig. 3.4. This setup represents the effects of exposure to different anomaly rates and the ability of A3C and CNN to determine the presence of anomalies in a trip. Specifically, for a trip length of $T = 15000$, we vary the anomaly rate to be $\xi \in \{1\%, 5\%, 10\%\}$. This experiment is motivated by the scenario in which the CAV does not know the anomaly rate of the road segment it is in, hence it may be unclear which trained model with regard to anomaly rate to use in these circumstances.

Table 3.4 illustrates the mean and 95% CI for the F1 score obtained from the CNN model when using various anomaly rates for training and testing for the bias anomaly type. First, note that a model that is trained using a given anomaly rate, presents different performances when tested under different anomaly rates. For instance, when testing a model that is trained on $\xi = 1\%$ (first row in Table 3.4) on anomaly rates $\xi \in \{1\%, 5\%, 10\%\}$, the resulting F1 score on average ranges between 86.82%–89.47%. Indeed in this case, the model that is trained and tested in the same type of environment, i.e., $\xi = 1\%$ for both training *and* test sets, presents the highest performance. As seen in the table, such trend generally holds; better performance is achieved when using the same anomaly rate in training and testing. The only exception observed in the table is in the case of $\xi = 5\%$ in training. In this case, testing the model when $\xi = 10\%$, compared with $\xi = 5\%$, results in approximately 1% higher performance. These results overall suggest that, in general, given the often unknown

Table 3.4: The mean and 95% CI for F1 score of the CNN model, obtained for various training and testing combinations of anomaly rate under bias anomaly type.

		Anomaly rate in testing		
		$\xi = 1\%$	$\xi = 5\%$	$\xi = 10\%$
Anomaly rate in training	$\xi = 1\%$	89.47 ± 1.54	87.94 ± 0.74	86.82 ± 0.55
	$\xi = 5\%$	92.01 ± 0.88	94.20 ± 0.29	95.53 ± 0.25
	$\xi = 10\%$	67.08 ± 1.71	89.93 ± 0.50	94.54 ± 0.55

Table 3.5: The mean and 95% CI for F1 score of the CNN model, obtained for various training and testing combinations of anomaly rate under gradual drift anomaly type.

		Anomaly rate in testing		
		$\xi = 1\%$	$\xi = 5\%$	$\xi = 10\%$
Anomaly rate in training	$\xi = 1\%$	87.20 ± 0.96	88.14 ± 0.61	89.00 ± 0.33
	$\xi = 5\%$	77.59 ± 0.81	91.50 ± 0.41	94.21 ± 0.17
	$\xi = 10\%$	86.35 ± 0.59	93.83 ± 0.19	95.31 ± 0.16

circumstances in which a previously trained model may be used, measures (such as dynamic thresholding) may need to be taken to achieve the pre-trained algorithm's full potential. Similar results are seen under the gradual drift anomaly type, presented in Table 3.5.

In the remainder of this section, we use the average anomaly rate of $\xi = 5\%$ to train the CNN model. This is consistent with real-world conditions where a single trained model is often implemented, without the knowledge on the true anomaly rate to be experienced by the CAVs.

Table 3.6 illustrates the anomaly detection performance of the models for the bias anomaly type for trip length $T = 15000$, and anomaly rate $\xi \in \{1\%, 5\%, 10\%\}$. From the results, it is seen that the addition of the A3C model improves the performance of the CNN model across all anomaly rates, particularly for F1 score. Specifically, paired t-tests indicate a statistically significant difference at a 5% level in F1 score between the A3C and CNN models for an anomaly rate of 5% and 10%. For the 1% anomaly rate, a statistical difference is not obtained which is, in part, due to the few anomalies encountered by the models. However, a better sensitivity and F1 score is still apparent from the results for the A3C model.

Similarly, Table 3.7 illustrates the anomaly detection performance of the models for the gradual drift anamaly type for trip length $T = 15000$, and anomaly rate $\xi \in \{1\%, 5\%, 10\%\}$. From the results, considering F1 score, it is seen that the addition of the A3C model improves

Table 3.6: The mean and 95% CI Anomaly detection performance of the bias anomaly type for trip length $T = 15000$, and anomaly rate $\xi \in \{1\%, 5\%, 10\%\}$. P-values indicate statistical significance at 5% level using paired t-tests, between the F1 scores for the CNN and A3C models for anomaly rates $\xi \in \{5\%, 10\%\}$.

	ξ =1%		ξ = 5%		ξ =10%	
	A3C	CNN	A3C	CNN	A3C	CNN
Accuracy	98.91 ±0.11	98.91 ±0.12	96.91 ±0.13	96.79 ±0.12	95.99 ±0.25	95.78 ±0.24
Sensitivity	91.48 ±1.14	91.03 ±1.22	90.99 ±0.51	90.48 ±0.49	92.46 ±0.48	91.92 ±0.48
Specificity	99.46 ±1.14	99.49 ±0.07	99.30 ±0.10	99.35 ±0.11	99.48 ±0.12	99.50 ±0.11
PPV	92.64 ±1.04	93.04 ±1.04	98.13 ±0.30	98.25 ±0.33	99.43 ±0.15	99.45 ±0.13
F1 score	92.04 ±0.82	92.01 ±0.88	94.43 ±0.30	94.20 ±0.29	95.82 ±0.25	95.53 ±0.25
Δ Improve	0.21 ± 0.02%		3.94± 0.01%		6.54 ± 0.02%	

the performance of the CNN model across all anomaly rates. Paired t-tests indicate a statistically significant difference at a 5% level in F1 score between the A3C and CNN models for all anomaly rates considered.

3.4.3 An Illustrative Example

In this section, we illustrate the performance of the CNN and A3C models for a bias anomaly encountered in a sample path. The example shows how the A3C model can improve upon the performance of the CNN model by changing its threshold to detect anomalous instances missed by the CNN. Fig. 3.5 illustrates a bias anomaly encountered in a sample path. More specifically, the top panel of the figure presents the baseline GPS speed (without anomalous instances), GPS baseline speed augmented with the anomaly, in-vehicle speed, and the acceleration. The bottom panel of the figure, shows the real-time CNN output probability, the fixed CNN threshold of 0.5, as well as the adaptive threshold specified by A3C. For the CNN model, while its output probability is less than 0.5, the system is classified as normal, and when it is greater than or equal to 0.5, the system is classified as anomalous. Similarly, for the A3C model, while the CNN-estimated probability is less than the A3C threshold, the system is classified as normal and vice versa.

Table 3.7: The mean and 95% CI Anomaly detection performance of the gradual drift anomaly type for trip length T = 15000, and anomaly rate $\xi \in \{1\%, 5\%, 10\%\}$. P-values indicate statistical significance at 5% level using paired t-tests, between the F1 scores for the CNN and A3C models for all anomaly rates, $\xi \in \{1\%, 5\%, 10\%\}$.

	ξ =1%		ξ = 5%		ξ =10%	
	A3C	CNN	A3C	CNN	A3C	CNN
Accuracy	96.79 ±0.11	96.42 ±0.09	95.53 ±0.15	95.17 ±0.15	94.55 ±0.21	94.41 ±0.17
Sensitivity	89.51 ±0.68	89.89 ±0.64	90.00 ±0.36	90.38 ±0.32	91.43 ±0.30	91.46 ±0.24
Specificity	97.33 ±0.08	96.91 ±0.07	97.78 ±0.24	97.12 ±0.26	97.63 ±0.25	97.35 ±0.22
PPV	71.23 ±1.38	68.27 ±1.28	94.21 ±0.71	92.66 ±0.81	97.45 ±0.30	97.15 ±0.28
F1 score	79.34 ±0.97	77.59 ±0.81	92.05 ±0.36	91.50 ±0.41	94.34 ±0.23	94.21 ±0.17
Δ Improve	7.83 ± 0.02%		6.35± 0.02%		2.24 ± 0.02%	

From the figure, it is seen that the bias anomaly starts at time epoch 1864 during the trip. As a result, the CNN output probability is consistently low (approximately 0.03) before this time. It is also seen that the threshold specified by the A3C is approximately 0.6 before the anomaly onset. It is seen that both the CNN and A3C models fail to correctly classify the first instance of the anomaly. However, from time epoch 1865, both models start to detect the anomaly, i.e., the CNN output probability is greater than or equal to both 0.5 and the A3C threshold. Over the next few epochs, the A3C threshold starts to lower (from 0.6 to 0.14) as the CNN-estimated probability increases, hence illustrating the changing threshold of A3C as anomalous instances are recognized and the A3C model grows more confident of its belief that the system is anomalous. At time epoch 1870, the CNN model outputs a probability of 0.27 meaning that the CNN classifies the system as normal, i.e., a FN is incurred. However, for A3C, its lowered threshold ensures that the CNN output probability is greater than its current threshold resulting in the A3C model correctly classifying the system as anomalous. Both models correctly detect the remainder of the anomaly. After the last instance of the anomaly occurs at time epoch 1873, the CNN probability lowers to approximately 0.03 again, and the A3C thresthreshouldhold is raised to approximately 0.6 again with both models correctly classifying the system as normal in the following time epochs.

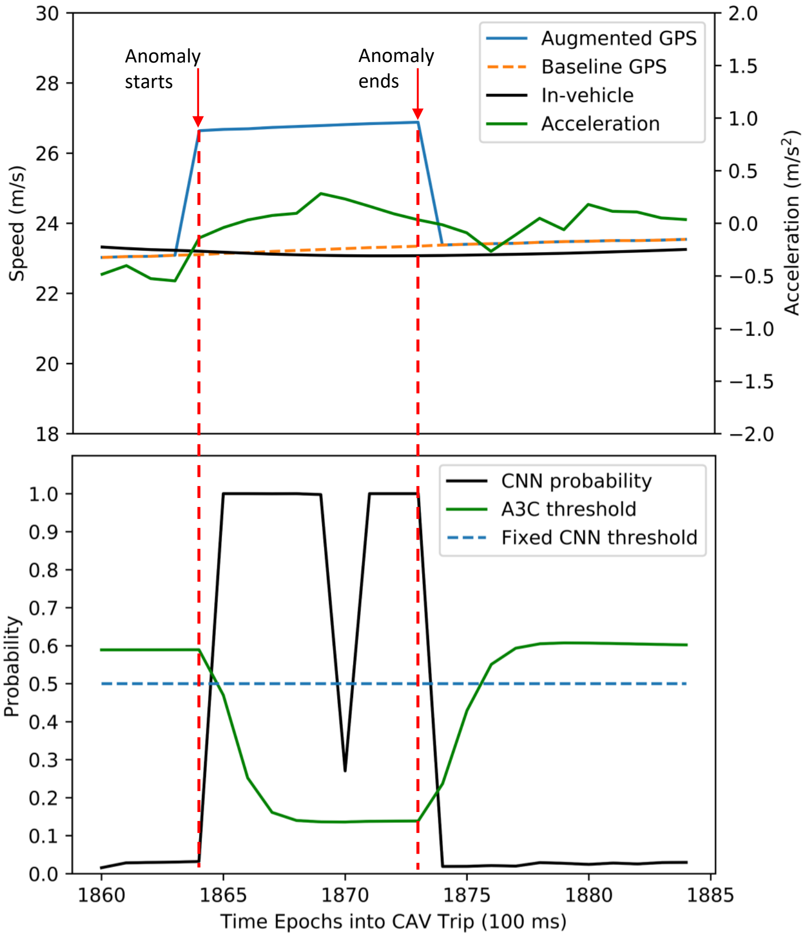

Figure 3.5: Illustration of a bias anomaly encountered in a sample path. The baseline speed, baseline speed augmented with the anomaly, the CNN output probability, and the threshold specified by A3C are illustrated.

3.5 Conclusion

The goal of this study is to develop a framework to detect anomalous behaviors in CAVs. Specifically, we develop an approach that embeds a CNN classification model into a Bayesian framework with the main objective of improving the performance of the primary classification model. It should be noted that any classification model can be used as part of the framework. The Bayesian framework consists of a POMDP model which is solved using the A3C algorithm. In addition, we incorporate recent trip information to more actively react to environmental changes and anomaly rates during a trip. The framework is also flexible to use in other applications where the cost of false negatives/positives can be adjusted as needed for specific purposes.

Our results show that the addition of the POMDP model leads to an improved performance, especially with respect to F1 score. Specifically, we conduct experiments where we fix the anomaly rate and vary the trip length and vice versa. In general, paired t-tests illustrate a statistical significant improvement for the A3C model compared to the CNN model's performance. This research contributes to the field of ITS safety. Specifically, the proposed framework addresses the issue of using a single trained classification model to detect anomalies. In real-world conditions, the anomaly rate of road segments are not known in advance. Hence, as illustrated in this study, using a hierarchical decision model may improve the anomaly detection capabilities of the primary classification model.

The study is subject to certain limitations. In our experiments, similar to previous studies in the literature, the anomalous instances in the speed sensor data are simulated. In our experiments, to illustrate the capabilities of the framework, anomaly types are limited to bias and gradual drift. Additional testing is required for other anomaly types and sensor types. It is envisioned that data collected from recently completed and ongoing pilot studies may contribute to the availability of real-world data including anomalous instances.

In future work, it may be useful to test additional models as the primary classification model in the framework. Also, other deep reinforcement learning techniques can be used to solve the POMDP model to compare to the performance of the A3C algorithm. In addition, it may be interesting to use the stream of belief probabilities generated by the POMDP in real-time as an input to an additional decision making model to more accurately approximate the true state of the system.

Conclusion

In this research, we investigate the several aspect of CAVs under cyber-security and safety uncertainties. Specifically, in Chaper 1, we investigate real-time sensor anomaly detection and identification in CAVs. We develop a robust anomaly detection approach through combining a deep learning method, namely convolutional neural network (CNN), with a well-established anomaly detection method, Kalman filtering, to detect and identify anomalous behavior in CAVs in real-time. Our numerical experiments demonstrate that the developed approach can detect anomalies and identify their sources with high accuracy, sensitivity, and F1 score.

In *Chapter 2*, we focus on the limitations of semi-autonomous vehicles under certain circumstances where it is safer for the human driver to be in control compared to the automated driving system. We investigate the transfer of control authority in semi-autonomous vehicles to improve overall road safety. We develop a Markov decision process (MDP) model to prescribe the entity in charge to minimize the expected safety risk of a trip. We also develop a partially observable Markov decision process (POMDP) model to account for cases when only partial information of the environmental risk is available. We gain insights into the associated risks and advantages of authority control transitions for semi-autonomous vehicles in certain conditions.

In *Chapter 3* we investigate real-time dynamic thresholding in classification algorithms to adapt to complex road and environmental conditions. Traditional classification algorithms use fixed and *a priori* determined thresholds which determine if information is anomalous or not. However, this approach does not allow for incorporating feedback obtained during a trip on the performance of the classification algorithm which may result in excessive false positive/negatives. To address this problem, we develop a mathematical framework in which we pair an anomaly classification algorithm, based on CNN, with a POMDP model to determine the optimal dynamic threshold of an anomaly classification algorithm to maximize the safety of a trip. The numerical experiments suggest that the addition of the POMDP model improves the anomaly detection performance of the CNN model, resulting in high accuracy, sensitivity, and positive predictive value. As a result, we gain insights into the associated benefits and disadvantages of implementing a dynamic classification threshold in response to complex exogenous factors.

Bibliography

Abadi, M., Barham, P., Chen, J., Chen, Z., Davis, A., Dean, J., Devin, M., Ghemawat, S., Irving, G., Isard, M., et al. (2016). Tensorflow: A system for large-scale machine learning. In *12th Symposium on Operating Systems Design and Implementation*, pages 265–283. 80

Ahmed, M., Mahmood, A. N., and Hu, J. (2016). A survey of network anomaly detection techniques. *Journal of Network and Computer Applications*, 60:19–31. 72

Arad, J., Housh, M., Perelman, L., and Ostfeld, A. (2013). A dynamic thresholds scheme for contaminant event detection in water distribution systems. *Water research*, 47(5):1899–1908. 73

Bai, F., Stancil, D. D., and Krishnan, H. (2010). Toward understanding characteristics of dedicated short range communications (dsrc) from a perspective of vehicular network engineers. In *Proceedings of the sixteenth annual international conference on Mobile computing and networking*, pages 329–340. ACM. 8

Belletti, F., Haziza, D., Gomes, G., and Bayen, A. M. (2017). Expert level control of ramp metering based on multi-task deep reinforcement learning. *IEEE Transactions on Intelligent Transportation Systems*, 19(4):1198–1207. 74

Bezemskij, A., Loukas, G., Gan, D., and Anthony, R. J. (2017). Detecting cyber-physical threats in an autonomous robotic vehicle using bayesian networks. In *Internet of Things (iThings) and IEEE Green Computing and Communications (GreenCom) and IEEE Cyber, Physical and Social Computing (CPSCom) and IEEE Smart Data (SmartData), 2017 IEEE International Conference on*, pages 98–103. IEEE. 10, 109

Bezzina, D. and Sayer, J. (2014). Safety pilot model deployment: Test conductor team report. *Report No. DOT HS*, 812:171. 18, 81

Bhuyan, M. H., Bhattacharyya, D. K., and Kalita, J. K. (2014). Network anomaly detection: methods, systems and tools. *Ieee communications surveys & tutorials*, 16(1):303–336. 11

Campbell, J. L., Brown, J. L., Graving, J. S.and Richard, C. M., Lichty, M. G.and Bacon, L. P., and Sanquist, T. (2018). Human factors design guidance for level 2 and level 3 automated driving concepts. 37

Chandola, V., Banerjee, A., and Kumar, V. (2009). Anomaly detection: A survey. *ACM computing surveys (CSUR)*, 41(3):15. 72

Chawla, N. V., Japkowicz, N., and Kotcz, A. (2004). Special issue on learning from imbalanced data sets. *ACM Sigkdd Explorations Newsletter*, 6(1):1–6. 31

Checkoway, S., McCoy, D., Kantor, B., Anderson, D., Shacham, H., Savage, S., Koscher, K., Czeskis, A., Roesner, F., Kohno, T., et al. (2011). Comprehensive experimental analyses of automotive attack surfaces. In *USENIX Security Symposium*. San Francisco. 8, 9, 109

Christiansen, P., Nielsen, L. N., Steen, K. A., Jørgensen, R. N., and Karstoft, H. (2016). Deepanomaly: Combining background subtraction and deep learning for detecting obstacles and anomalies in an agricultural field. *Sensors*, 16(11):1904. 10, 109

Currie, R. (2015). Developments in car hacking. *SANS Institute, InfoSec Reading Room, Accepted Dec*, 5:33. 19

Curtis, S. (2015). Self-driving cars can be hacked using a laser pointer. *The Telegraph, Sept*, 8. 72

Darms, M., Rybski, P., and Urmson, C. (2008). Classification and tracking of dynamic objects with multiple sensors for autonomous driving in urban environments. In *Intelligent Vehicles Symposium, 2008 IEEE*, pages 1197–1202. IEEE. 9

Davies, A. (2015). Ford's skipping the trickiest thing about self-driving cars. [Online; accessed 7/17/2017]. 39

de La Bourdonnaye, F., Teulière, C., Chateau, T., and Triesch, J. (2017). Learning of binocular fixations using anomaly detection with deep reinforcement learning. In *2017 International Joint Conference on Neural Networks (IJCNN)*, pages 760–767. IEEE. 74

De Winter, J. C., Happee, R., Martens, M. H., and Stanton, N. A. (2014). Effects of adaptive cruise control and highly automated driving on workload and situation awareness: A review of the empirical evidence. *Transportation research part F: traffic psychology and behaviour*, 27:196–217. 39

Eriksson, A. and Stanton, N. A. (2017). Takeover time in highly automated vehicles: Noncritical transitions to and from manual control. *Human factors*, 59(4):689–705. 40

Fagnant, D. J. and Kockelman, K. (2015). Preparing a nation for autonomous vehicles: opportunities, barriers and policy recommendations. *Transportation Research Part A: Policy and Practice*, 77:167–181. 37

Field, M. (2017). Graffiti on stop signs could trick driverless cars into driving dangerously. [Online; accessed 09-01-2017]. 8, 72

Foo, G. H. B., Zhang, X., and Vilathgamuwa, D. M. (2013). A sensor fault detection and isolation method in interior permanent-magnet synchronous motor drives based on an extended kalman filter. *IEEE Transactions on Industrial Electronics*, 60(8):3485–3495. 10

Goodrich, M. A. and Boer, E. R. (2000). Designing human-centered automation: Trade-offs in collision avoidance system design. *IEEE Transactions on Intelligent Transportation Systems*, 1(1):40–54. 38

Green, M. (2000). How long does it take to stop? Methodological analysis of driver perception-brake times. *Transportation Human Factors*, 2(3):195–216. 39

Greenberg, A. (2015). Hackers remotely kill a jeep on the highwaywith me in it. *Wired*, 7:21. 7, 8

Gu, S., Lillicrap, T., Sutskever, I., and Levine, S. (2016). Continuous deep q-learning with model-based acceleration. In *International Conference on Machine Learning*, pages 2829–2838. 48

Guler, S. I., Menendez, M., and Meier, L. (2014). Using connected vehicle technology to improve the efficiency of intersections. *Transportation Research Part C: Emerging Technologies*, 46:121–131. 37

Huang, C., Wu, Y., Zuo, Y., Pei, K., and Min, G. (2018). Towards experienced anomaly detector through reinforcement learning. In *Thirty-Second AAAI Conference on Artificial Intelligence*. 74

Huq, N., Vosseler, R., and Swimmer, M. (2017). Cyberattacks against intelligent transportation systems. Technical report, TrendLabs, Tech. Rep., 2017, available at https://documents. trendmicro. com . 8

Idé, T. and Kashima, H. (2004). Eigenspace-based anomaly detection in computer systems. In *Proceedings of the tenth ACM SIGKDD international conference on Knowledge discovery and data mining*, pages 440–449. ACM. 73

Jo, M., Park, J., Baek, Y., Ivanov, R., Weimer, J., Son, S. H., and Lee, I. (2016). Adaptive transient fault model for sensor attack detection. In *Cyber-Physical Systems, Networks, and Applications (CPSNA), 2016 IEEE 4th International Conference on*, pages 59–65. IEEE. 8, 109

Kaber, D. B. and Endsley, M. R. (2004). The effects of level of automation and adaptive automation on human performance, situation awareness and workload in a dynamic control task. *Theoretical Issues in Ergonomics Science*, 5(2):113–153. 39

Kalman, R. E. (1960). A new approach to linear filtering and prediction problems. *Journal of basic Engineering*, 82(1):35–45. 10

Kalmuk, A., Granichin, O., Granichina, O., and Ding, M. (2016). A dynamic threshold based algorithm for change detection in autonomous systems. *IFAC-PapersOnLine*, 49(13):141–145. 73

Kang, M.-J. and Kang, J.-W. (2016). Intrusion detection system using deep neural network for in-vehicle network security. *PloS one*, 11(6):e0155781. 10, 109

Khalastchi, E., Kaminka, G. A., Kalech, M., and Lin, R. (2011). Online anomaly detection in unmanned vehicles. In *The 10th International Conference on Autonomous Agents and Multiagent Systems-Volume 1*, pages 115–122. International Foundation for Autonomous Agents and Multiagent Systems. 10, 109

Kingma, D. P. and Ba, J. (2014). Adam: A method for stochastic optimization. *International Conference on Learning Representations (ICLR), San Diego, USA*. 17, 76

Koo, J., Shin, D., Steinert, M., and Leifer, L. (2016). Understanding driver responses to voice alerts of autonomous car operations. *International journal of vehicle design*, 70(4):377–392. 40

Koscher, K., Czeskis, A., Roesner, F., Patel, S., Kohno, T., Checkoway, S., McCoy, D., Kantor, B., Anderson, D., Shacham, H., et al. (2010). Experimental security analysis of a modern automobile. In *Security and Privacy (SP), 2010 IEEE Symposium on*, pages 447–462. IEEE. 7, 8, 71, 109

Krizhevsky, A., Sutskever, I., and Hinton, G. (2012). Imagenet classification with deep convolutional neural networks. *Advances in neural information processing systems*, pages 1097–1105. 16, 17

Kruegel, C., Mutz, D., Robertson, W., and Valeur, F. (2003). Bayesian event classification for intrusion detection. In *19th Annual Computer Security Applications Conference, 2003. Proceedings.*, pages 14–23. IEEE. 72

Kyriakidis, M., Happee, R., and de Winter, J. C. (2015). Public opinion on automated driving: Results of an international questionnaire among 5000 respondents. *Transportation research part F: traffic psychology and behaviour*, 32:127–140. 38

Lambert, F. (2017). Tesla autopilot crash caught on dashcam shows how not to use the system. Accessed 6/17/2017. 38, 50

Levi, M., Allouche, Y., and Kontorovich, A. (2018). Advanced analytics for connected car cybersecurity. In *2018 IEEE 87th Vehicular Technology Conference (VTC Spring)*, pages 1–7. IEEE. 109

Levine, S., Finn, C., Darrell, T., and Abbeel, P. (2016). End-to-end training of deep visuomotor policies. *The Journal of Machine Learning Research*, 17(1):1334–1373. 74

Levy, H. (2015). *Stochastic dominance: Investment decision making under uncertainty.* Springer. 57

Lillicrap, T. P., Hunt, J. J., Pritzel, A., Heess, N., Erez, T., Tassa, Y., Silver, D., and Wierstra, D. (2015). Continuous control with deep reinforcement learning. *arXiv preprint arXiv:1509.02971*. 74

Lin, R., Khalastchi, E., and Kaminka, G. A. (2010). Detecting anomalies in unmanned vehicles using the mahalanobis distance. In *Robotics and Automation (ICRA), 2010 IEEE International Conference on*, pages 3038–3044. IEEE. 10, 109

Litman, T. (2017). *Autonomous vehicle implementation predictions*. Victoria Transport Policy Institute Victoria, Canada. 7

Loebis, D. B., Sutton, R., Chudley, J., and Naeem, W. (2004). Sensor faults: Detection methods and prevalence in real-world datasets. *Control engineering practice*, 12(12):1531–1539. 15

Lu, Z. and de Winter, J. C. (2015). A review and framework of control authority transitions in automated driving. *Procedia Manufacturing*, 3:2510–2517. 38

Malhotra, P., Vig, L., Shroff, G., and Agarwal, P. (2015). Long short term memory networks for anomaly detection in time series. In *Proceedings*, page 89. Presses universitaires de Louvain. 13

Marchetti, M., Stabili, D., Guido, A., and Colajanni, M. (2016). Evaluation of anomaly detection for in-vehicle networks through information-theoretic algorithms. In *2016 IEEE 2nd International Forum on Research and Technologies for Society and Industry Leveraging a better tomorrow (RTSI)*, pages 1–6. IEEE. 109

Merat, N., Jamson, A. H., Lai, F. C., Daly, M., and Carsten, O. M. (2014a). Transition to manual: Driver behaviour when resuming control from a highly automated vehicle. *Transportation research part F: traffic psychology and behaviour*, 27:274–282. 40

Merat, N., Jamson, H. A., Lai, F., and Carsten, O. (2014b). Human factors of highly automated driving: results from the easy and citymobil projects. In *Road vehicle automation*, pages 113–125. Springer. 39

Meyer, G. and Beiker, S. (2014). *Road Vehicle Automation*. Springer. 7

Miller, D., Sun, A., Johns, M., Ive, H., Sirkin, D., Aich, S., and Ju, W. (2015). Distraction becomes engagement in automated driving. In *Proceedings of the Human Factors and Ergonomics Society Annual Meeting*, volume 59, pages 1676–1680. SAGE Publications Sage CA: Los Angeles, CA. 40

Mnih, V., Badia, A. P., Mirza, M., Graves, A., Lillicrap, T., Harley, T., Silver, D., and Kavukcuoglu, K. (2016). Asynchronous methods for deep reinforcement learning. In *International conference on machine learning*, pages 1928–1937. 47, 64, 74, 79, 80

Mnih, V., Kavukcuoglu, K., Silver, D., Rusu, A. A., Veness, J., Bellemare, M. G., Graves, A., Riedmiller, M., Fidjeland, A. K., Ostrovski, G., et al. (2015). Human-level control through deep reinforcement learning. *Nature*, 518(7540):529. 74

Mo, Y., Garone, E., Casavola, A., and Sinopoli, B. (2010). False data injection attacks against state estimation in wireless sensor networks. In *Decision and Control (CDC), 2010 49th IEEE Conference on*, pages 5967–5972. IEEE. 11

Moavenzadeh, J. and Lang, N. (2018). Reshaping urban mobility with autonomous vehicles lessons from the city of boston. Technical report. 72

Mohamed, A. H. and Schwarz, K. P. (1999). Adaptive kalman filtering for ins/gps. In *Adaptive Kalman filtering for INS/GPS*. 14

Müter, M. and Asaj, N. (2011). Entropy-based anomaly detection for in-vehicle networks. In *Intelligent Vehicles Symposium (IV), 2011 IEEE*, pages 1110–1115. IEEE. 10, 109

National Safety Council (2015). Injury facts. 112

NHTSA (2013). Preliminary statement of policy concerning automated vehicles. *National Highway Traffic Safety Administration and others, Washington, DC*, pages 1–14. 10, 71

Ni, D. (2015). *Traffic flow theory: Characteristics, experimental methods, and numerical techniques*. Butterworth-Heinemann. 71

Parasuraman, R. and Manzey, D. H. (2010). Complacency and bias in human use of automation: An attentional integration. *Human factors*, 52(3):381–410. 38

Park, J., Ivanov, R., Weimer, J., Pajic, M., and Lee, I. (2015). Sensor attack detection in the presence of transient faults. In *Proceedings of the ACM/IEEE Sixth International Conference on Cyber-Physical Systems*, pages 1–10. ACM. 10, 109

Park, S.-h., Kim, S.-m., and Ha, Y.-g. (2016). Highway traffic accident prediction using vds big data analysis. *The Journal of Supercomputing*, 72(7):2815–2831. 31

Parkinson, S., Ward, P., Wilson, K., and Miller, J. (2017). Cyber threats facing autonomous and connected vehicles: Future challenges. *IEEE transactions on intelligent transportation systems*, 18(11):2898–2915. 71

Petit, J. and Shladover, S. E. (2015). Potential cyberattacks on automated vehicles. *IEEE Transactions on Intelligent Transportation Systems*, 16(2):546–556. 8, 11, 19, 38, 71, 109

Pous, N., Gingras, D., and Gruyer, D. (2017). Intelligent vehicle embedded sensors fault detection and isolation using analytical redundancy and nonlinear transformations. *Journal of Control Science and Engineering*, 2017. 9

Puterman, M. (1994). *Markov Decision Processes: Discrete Stochastic Dynamic Programming*. John Wiley and Sons, New York, NY. 49

Ran, B. and Boyce, D. (2012). *Dynamic urban transportation network models: theory and implications for intelligent vehicle-highway systems*, volume 417. Springer Science & Business Media. 7

Realpe, M., Vintimilla, B., and Vlacic, L. (2015). Sensor fault detection and diagnosis for autonomous vehicles. In *MATEC Web of Conferences*, volume 30, page 04003. EDP Sciences. 9

Rios-Torres, J. and Malikopoulos, A. A. (2016). A survey on the coordination of connected and automated vehicles at intersections and merging at highway on-ramps. *IEEE Transactions on Intelligent Transportation Systems*, 18(5):1066–1077. 71

Roy, N., Gordon, G., and Thrun, S. (2005). Finding approximate pomdp solutions through belief compression. *Journal of artificial intelligence research*, 23:1–40. 74

Rudin-Brown, C. M. and Parker, H. A. (2004). Behavioural adaptation to adaptive cruise control (acc): implications for preventive strategies. *Transportation Research Part F: Traffic Psychology and Behaviour*, 7(2):59–76. 40

SAE (2014). Taxonomy and definitions for terms related to on-road motor vehicle automated driving systems. *SAE Standard J3016*, pages 01–16. 38

SAE (2016). Taxonomy and definitions for terms related to driving automation systems for on-road motor vehicles. 37

Schmidhuber, J. (2015). Deep learning in neural networks: An overview. *Neural networks*, 61:85–117. 10, 17

Sharma, A. B., Golubchik, L., and Govindan, R. (2010). Sensor faults: Detection methods and prevalence in real-world datasets. *ACM Transactions on Sensor Networks (TOSN)*, 6(3):23. 11

Singh, S. (2015). Critical reasons for crashes investigated in the national motor vehicle crash causation survey. Technical report. 71

Srivastava, N., H. G. K. A. S. I. and Salakhutdinov, R. (2014). Dropout: a simple way to prevent neural networks from overfitting. *Journal of machine learning research*, 15(1):1929–1958. 17

Strand, N., Nilsson, J., Karlsson, I. M., and Nilsson, L. (2014). Semi-automated versus highly automated driving in critical situations caused by automation failures. *Transportation research part F: traffic psychology and behaviour*, 27:218–228. 40

Sutton, R. S. and Barto, A. G. (2018). *Reinforcement learning: An introduction.* MIT press. 74

Taylor, A., Leblanc, S., and Japkowicz, N. (2016). Anomaly detection in automobile control network data with long short-term memory networks. In *2016 IEEE International*

Conference on Data Science and Advanced Analytics (DSAA), pages 130–139. IEEE. 10, 109

Tesla (2017). Tesla model s owner's manual. Accessed 6/17/2017. 38

Tieleman, T. and Hinton, G. (2012). Lecture 6.5-rmsprop: Divide the gradient by a running average of its recent magnitude. In *COURSERA: Neural networks for machine learning.* 80

Trippel, T., Weisse, O., Xu, W., Honeyman, P., and Fu, K. (2017). Walnut: Waging doubt on the integrity of mems accelerometers with acoustic injection attacks. In *Security and Privacy (Euro S&P), 2017 IEEE European Symposium*, pages 3–18. IEEE. 19

Truong, K. N., Patel, S. N., Summet, J. W., and Abowd, G. D. (2005). Preventing camera recording by designing a capture-resistant environment. In *International Conference on Ubiquitous Computing*, pages 73–86. Springer. 8

USDOT (2016). United states department of transportation. connected vehicles and cyber security. [Online; accessed 09-03-2017]. 7

Van Hasselt, H., Guez, A., and Silver, D. (2016). Deep reinforcement learning with double q-learning. In *Thirtieth AAAI Conference on Artificial Intelligence.* 48, 79

van Wyk, F., Wang, Y., Khojandi, A., and Masoud, N. (2019). Real-time sensor anomaly detection and identification in automated vehicles. *IEEE Transactions on Intelligent Transportation Systems.* 75, 76, 81

Wei, X., Verhaegen, M., and van Engelen, T. (2010). Sensor fault detection and isolation for wind turbines based on subspace identification and kalman filter techniques. *International Journal of Adaptive Control and Signal Processing*, 24(8):687–707. 10

Weimerskirch, A. and Gaynier, R. (2015). An overview of automotive cybersecurity: Challenges and solution approaches. In *TrustED@ CCS*, page 53. 7, 8, 71

Williams, C. (2017). Hackers hit d.c. police closed-circuit camera network, city officials disclose. Technical report, Available at:https://www.washingtonpost.com/local/public-safety/hackers-hit-dcpolice- closed-circuit-camera-network-city-officials-disclose. 8

Yan, C., Xu, W., and Liu, J. (2016). Can you trust autonomous vehicles: Contactless attacks against sensors of self-driving vehicle. *DEF CON*, 24. 8, 109

Yang, S., Liu, Z., Li, J., Wang, S., and Yang, F. (2016). Anomaly detection for internet of vehicles: A trust management scheme with affinity propagation. *Mobile Information Systems*, 2016. 10, 109

Young, M. S. and Stanton, N. A. (2007). Back to the future: Brake reaction times for manual and automated vehicles. *Ergonomics*, 50(1):46–58. 39

Appendices

A Summary of Key Literature and Notation for Chapter 1

Table A.1: Summary of key literature related to anomaly detection in CAVs.

Author(s)	Cyber-security/anomaly aspects investigated	Key relevant findings	Study approach (method)	Type of data used
Yang et al. (2016)	Anomaly detection for internet of vehicles, specifically, detecting abnormal vehicles operating in a platoon	Low detection failure rate below 1%, demonstrating its ability to detect and filter the abnormal vehicles	Affinity propagation framework	Simulation in TransModeler
Jo et al. (2016)	An adaptive transient fault model for sensor attack detection for multiple operating mode systems	Improvement on existing non-transient fault models. Uses a dynamic look-up table for the applicable system parameters	Transient fault model (TFM) using graph theory	Data obtained from an unmanned ground vehicle. Simulated attacks
Checkoway et al. (2011)	Analysis of external attack surfaces of a modern automobile	Remote exploitation is feasible via a broad range of attack vectors	Experimental analyses on vehicles in the sedan segment	Real experiments on vehicles
Christiansen et al. (2016)	Obstacle/anomaly detection algorithm using deep learning	High accuracy, low computation time and low memory footprint	Combine background subtraction and CNN	Field experiments
Yan et al. (2016)	Examines the security of the sensors of autonomous vehicles, and investigate the trustworthiness of the sensors	Off-the-shelf hardware were able to perform jamming and spoofing attacks which can compromise the safety of self-driving cars	Laboratory and outdoor experiments	Collected data through experiments
Lin et al. (2010)	A model-free approach for detecting anomalies in unmanned autonomous vehicles, based on sensor readings	Works well for a limited number of attributes	Anomaly detection using Mahalanobis distance	Data from unmanned aerial vehicle
Bezemskij et al. (2017)	Detecting cyber-physical threats in real time in an autonomous robotic vehicle	Can determine whether an AV is under attack and also whether the attack originated from the cyber or the physical domain	Heuristic binary classifier and Bayesian network	Simulated attacks using an unmanned ground vehicle
Müter and Asaj (2011) Marchetti et al. (2016)	Detecting anomalies (attacks) for in-vehicle networks	Certain attacks on the CAN-bus of a vehicle were detected using the proposed methodology. Difficult to detect low-volume attacks	Signal entropy	Field experiments using a vehicle, CAN data
Koscher et al. (2010)	Experimental security analysis of a modern automobile	It is possible to bypass rudimentary network security protections such as the malicious bridging between a cars internal subnets	Experiments in laboratory and road tests	Various experiments
Khalastchi et al. (2011)	Online anomaly detection in unmanned vehicles	Method is able to take into account a large number of monitored sensors and internal measurements	Anomaly detection using Mahalanobis distance	Data from robot, and a high-fidelity flight simulator
Petit and Shladover (2015)	State of the art in identifying potential cyber attacks on automated vehicles	Identifies risks of various importance. Identifies GNSS spoofing and injection of fake messages as most dangerous attacks on AVs	Exploratory study	Review of literature
Kang and Kang (2016)	A deep learning model to enhance in-vehicular safety by detecting malicious CAN packets	Real-time response to the attack with a significantly improved detection ratio in controller area network (CAN) bus	Multilayer perceptron (MLP) model	Simulated data using software package (OCTANE)
Park et al. (2015)	Addresses the problem of detection and identification of sensor attacks in the presence of transient faults	Able to detect and identify attacks using sensor fusion	Pairwise inconsistencies between sensors to detect and identify attacks	Unmanned ground vehicle
Taylor et al. (2016)	Deep learning to detect attacks on CAN bus	Detect anomalies with low false alarm rates	Long Short-Term Memory (LSTM) recurrent neural network (RNN)	Synthesize anomalies with modified CAN bus data
Levi et al. (2018)	Machine learning approach is proposed to protect connected vehicles	Detect anomalies with a large number of features	Combine Hidden Markov Model and regression model	Simulation using software (SUMO)

Table A.2: Summary of notation for Chapter 1.

Variable	**Description**
n	Number of sensors
α	Anomaly rate
x	State variable of Kalman filter
z	Sensor measurement
w	Process noise of state-transition model
v	Sensor measurement noise
ν	Innovation between measurement and predicted value of the measurement
A	State-transition matrix
H	Sensor measurement matrix
R	Process noise covariance matrix
Q	Measurement noise covariance matrix
$\hat{R}$	Process noise covariance matrix estimate
$\hat{Q}$	Measurement noise covariance matrix estimate
S	Covariance matrix of innovation
P	Error covariance matrix, where the error is the difference between true and predicted state values
M	Window size of adaptive Kalman filter
γ	χ^2 detector parameter

B Model Calibration

In this study, due to lack of access to data, trips and their characteristics are simulated. That is, given the length of a trip and the number of links connecting the trip origin to destination, the link lengths and accident probabilities are randomly generated on the path from the origin to the destination where probabilities of an accident occurring remain unchanged throughout a given link. All trips in the computational study, except when stated otherwise, use a fixed trip length of 1000 consisting of 10 links.

For simplicity, in our computational study, the road/environment vector, $\boldsymbol{\xi}$, is summarized into three risk levels, namely, $\xi = 0, 1, 2$ corresponding to low, average, and high risk, respectively. We let the stochastic matrix $\boldsymbol{P}$ denote the one-step transition probability matrix (TPM) for the road/environment condition where the element (i, j) represents the probability of transitioning from condition i to j, $p(j|i)$. We use the following matrix as the base matrix in our computational study representing an average risk profile:

$$\boldsymbol{P} = \begin{bmatrix} 0.95 & 0.04 & 0.01 \\ 0.6 & 0.35 & 0.05 \\ 0.25 & 0.7 & 0.05 \end{bmatrix}. \tag{8}$$

For instance, according to the probabilities provided in the matrix, if the road/environment is in the low risk condition, then in the next time epoch, e.g., one second later, the state of the road/environment will remain in the low risk condition with probability 0.95, or transitions to an average or a high risk condition with probabilities 0.04 and 0.01, respectively.

Due to lack of access to real-world data, all probability values are generated based on the existing literature and the know-how of the authors and other experts in the field. Specifically, to obtain probability distributions for accident severity in the manual driving mode under various driving scenarios, we use the existing literature, as will be elaborated in the following. Similarly, we use expert knowledge to approximate the probability distributions for accident severity in the autonomous driving mode under various driving scenarios. Table B.1 summarizes the parameter values for the conditional probabilities of accident severity at location-environment $\boldsymbol{\mu}$, used in the computational study, where a random error $\epsilon \sim \mathcal{U}(0, 0.01)$ is incorporated for each link and then the vectors are normalized. Note that an accident may occur due to local road/environment conditions or due to a switch in control authority. For the probability of accident for the driving entity ϕ under $[\ell, \xi]$, $p_\phi(\boldsymbol{\mu})$, random numbers are generated from $\mathcal{U}(0, 0.001)$ for each link and driving entity such that the probability of accident increases in ξ. Similarly, for the probability of accident as a result of a switch of the vehicle control to entity ϕ under $[\ell, \xi]$, $\zeta_\phi(\boldsymbol{\mu})$, random numbers are generated for each link from $\mathcal{U}(0, 0.01)$ and $\mathcal{U}(0, 0.0001)$ for switching to the individual and the car, respectively, such that the probability of accident increases in ξ.

Table B.1: Parameter value generation for $\boldsymbol{q}(\phi, \boldsymbol{\mu})$ and $\boldsymbol{\rho}(\boldsymbol{\mu})$

Road/environment condition, ξ	**Driving entity,** ϕ	$q_0(\phi, \boldsymbol{\mu})$, $q_1(\phi, \boldsymbol{\mu})$, $q_2(\phi, \boldsymbol{\mu})$	$\rho_0(\boldsymbol{\mu})$, $\rho_1(\boldsymbol{\mu})$, $\rho_2(\boldsymbol{\mu})$
Low risk	Individual	$0.95 + \epsilon, 0.04 + \epsilon, 0.01 + \epsilon$	$0.55 + \epsilon, 0.4 + \epsilon, 0.05 + \epsilon$
	Car	$0.99 + \epsilon, 0.01 + \epsilon, 0 + \epsilon$	
Average risk	Individual	$0.1 + \epsilon, 0.7 + \epsilon, 0.2 + \epsilon$	$0.2 + \epsilon, 0.7 + \epsilon, 0.1 + \epsilon$
	Car	$0.2 + \epsilon, 0.7 + \epsilon, 0.1 + \epsilon$	
High risk	Individual	$0.05 + \epsilon, 0.45 + \epsilon, 0.5 + \epsilon$	$0.05 + \epsilon, 0.65 + \epsilon, 0.3 + \epsilon$
	Car	$0.05 + \epsilon, 0.65 + \epsilon, 0.3 + \epsilon$	

We set $k = 5$ seconds, an average RT value based on tests conducted by Audi as described in Section 1.1. A 2015 report from the national safety council reports the average economic cost of fatalities, injuries, and property damage to be \$1.5 million, \$80,700, and \$9,300 per accident, respectively (National Safety Council, 2015). Hence, the accident cost vector is calibrated accordingly, i.e., $c = [9300, 80700, 1500000]$. The costs of alerting and foregoing the alert are set to 5000, i.e., $c_A = c_p = 5000$, to make their combined value comparable to the cost of property damage following an accident. Finally, the discount factor is set to 0.97, i.e., $\alpha = 0.97$.

Vita

Franco van Wyk is from Upington, South Africa. He attended the Duineveld High School in Upington and moved to Stellenbosch in 2011 to pursue a degree in engineering. He received a Bachelor's of Mechanical Engineering degree from the University of Stellenbosch in 2014. He then received a Master's degree in Engineering Management from the University of Stellenbosch in 2016 where his research focused on decision-making in volatile business environments. From there, he moved to Knoxville, Tennessee, to pursue a PhD in Industrial Engineering at the University of Tennessee. He conducted research in the health care and transportation sectors. His research in health care focused on the development of algorithms to aid the early detection of sepsis, an illness caused by the body's dysregulated response to an infection. His research in transportation focused on improving the safety of connected and automated vehicles under cyber-security and safety uncertainties.